**Title**
Inverse Free Electron Laser Interactions with Sub-Picosecond High Brightness Electron Beams



**Author**
Moody, Joshua Timothy

**Publication Date**
2014

Peer reviewed|Thesis/dissertation

University of California
Los Angeles

# Inverse Free Electron Laser Interactions with Sub-Picosecond High Brightness Electron Beams

A dissertation submitted in partial satisfaction
of the requirements for the degree
Doctor of Philosophy in Physics

by

**Joshua Timothy Moody**

2014

Abstract of the Dissertation

# Inverse Free Electron Laser Interactions with Sub-Picosecond High Brightness Electron Beams

by

**Joshua Timothy Moody**

Doctor of Philosophy in Physics

University of California, Los Angeles, 2014

Professor Pietro Musumeci, Chair

Advanced accelerators have great promise in reducing the size and cost of high energy colliders as well as bringing high brightness x-ray sources to the laboratory tabletop scale. The inverse free electron laser (IFEL) is a high gradient advanced accelerator scheme that is one of the most efficient ways of transferring energy from a laser to an electron beam. By copropagating a laser and a relativistic electron beam through an undulator in vacuum and taking advantage of resonant ponderomotive motion of the electron beam, IFEL avoids the breakdown associated with other schemes that use a material to couple the laser fields to the electron beams.

This dissertation provides an overview of IFEL, the photoinjector electron beams to be used in IFEL interactions, and two IFEL applications: compression and synchronization of a photoinjector electron beam to a laser application using THz driven IFEL and high gradient acceleration using IFEL.

The numerically investigated THz IFEL application shows that with a 10 $\mu$J THz 8 pulse train, an electron beam bunch length of 100 fs RMS can be compressed to 14 fs RMS and have the beam's time of arrival jitter relative to an external laser reduced by an order of magnitude.

High gradient acceleration by IFEL was examined experimentally at Lawrence Livermore National Laboratory (LLNL). This experiment marks the first attempt to use sub-picosecond time pulse, TW peak power scale titanium:sapphire laser pulses to perform IFEL acceleration. The demonstrated energy gain from 77 to 120 MeV combined with particle tracking simulations shows an accelerating gradient of over 200 MeV/m. Because the laser pulse length is the same order as the slippage experienced by the electron beam with respect to the laser and the time of arrival jitter has been measured to be greater than 2 ps, the overlap is investigated through relative single shot time of arrival measurements using electro-optic sampling based spatial encoding techniques. The temporal overlap measurement was found to be consistent with a cross-correlation model taking into account the independently measured laser and electron beam lengths.

The dissertation of Joshua Timothy Moody is approved.

Benjamin Williams

James B Rosenzweig

Pietro Musumeci, Committee Chair

University of California, Los Angeles

2014

*For my family and friends...*

# Table of Contents

# List of Figures

# List of Tables

# Acknowledgments

I would like to thank my parents who supported and believed in me enough to get this far.

Thanks to all of my friends and colleagues at the Particle Beam Physics Lab who made my life fun during graduate school. This includes my office mates: Brendan and Finn O'Shea who would have "Irish Lunch" at 11:00 a.m., Hoson To, Evan Threshkeld, Long Vo, Sean Custodio, Andrey Knyazik, Andy Yakub, Gabe Marcus, and Gerard Andonian who had some epic Starcraft 2 and foos games with me. I would also like to thank David Schiller for the quick IT support at the times it was necessary.

I would like to specially thank Cheyne Scoby who kept my morale up in the time I spent in Pegasus through sailing, flying, and Disneyland trips. Thanks to Joe Duris who tried to keep me active through swing dancing, and to Oliver Williams for the appreciation of death metal, Bad Religion, and Johnnie's Pastrami.

Thanks to Dawnell and Micah, who let me live in Livermore rent free while I struggled to get data, and thanks to Scott and Gerry who got the LLNL experiment going and kept my social life alive in Livermore.

I would like to thank the love of my life, Onnie Luk, who helps me through the rough times and makes me work to be a better person, I hope you will soon join me in Europe.

Finally I would like to thank my advisor, who, although we never really saw eye-to-eye, gave me a lot more patience than I deserve...

# Vita

| | |
|---|---|
| 2006 | B.S. (Physics) University of California at Los Angeles. |
| 2007 | Teaching Assistant, Department of Physics and Astronomy, University of California at Los Angeles. |
| 2007-2014 | Graduate Research Assistant, Department of Physics and Astronomy, University of California at Los Angeles. |

# Publications

P. Musumeci, J. Moody, G. Gatti. 2007. Ultrafast Beam Research at the Pegasus Laboratory. Proceedings of Particle Accelerator Conference 2007.

P. Musumeci, J. Moody, R.J. England, J.B. Rosenzweig, T. Tran.. Dynamically self-optimized beam distributions at the UCLA Pegasus Laboratory: linearity of transverse and longitudinal phase spaces. Nuclear Methods and Instruments. (2007)

P. Musumeci, J.T. Moody, C.M. Scoby. Relativistic Electron Diffraction at the UCLA Pegasus Laboratory. Journal of Ultramicroscopy (2007)

P. Musumeci, J. T. Moody, R. J. England, J. B. Rosenzweig, and T. Tran Experimental Generation and Characterization of Uniformly Filled Ellipsoidal Electron-Beam Distributions. Phys. Rev. Lett. 100, 244801 (2008)

J. T. Moody, P. Musumeci, M. S. Gutierrez, J. B. Rosenzweig, and C. M. Scoby. Longitudinal phase space characterization of the blow-out regime of rf photoinjector operation. Phys. Rev. ST Accel. Beams 12, 070704 (2009)

C. M. Scoby, P. Musumeci, J. T. Moody, and M. S. Gutierrez. Electro-optic sampling at 90 degree interaction geometry for time-of-arrival stamping of ultrafast relativistic electron diffraction. Phys. Rev. ST Accel. Beams 13, 022801 (2010)

P. Musumeci, J. T. Moody, C. M. Scoby, M. S. Gutierrez, H. A. Bender, N. S. Wilcox. High quality single shot diffraction patterns using ultrashort megaelectron volt electron beams from a radio frequency photoinjector. Review of Scientific Instruments 81, 013306 (2010)

J.T. Moody, R.K. Li, P. Musumeci, C.M. Scoby, H.L. To, Compression and Synchronization of an Ultra-short Electron Beam Using a THz Undulator Interaction, Proceedings of 2011 Particle Accelerator Conference.

J.T. Moody, P. Musumeci, G.G. Anderson, S.G.Anderson, M. Betts, DJ. Gibson, A.M. Tremaine, SSQ Wu, The LLNL/UCLA High Gradient Inverse Free Electron Laser Accelerator. Proceedings of IPAC 2012.

J.T. Moody, P. Musumeci, G.G. Anderson, S.G.Anderson, M. Betts, DJ. Gibson, A.M. Tremaine, SSQ Wu, Results of the Short Pulse driven LLNL/UCLA IFEL Experiment. Proceedings of NAPAC 2013.

# CHAPTER 1

# Introduction

There is a large variety of applications for particle accelerators in modern science and technology. High energy, high quality beams are required to push the energy frontier with high luminosity colliders in high energy physics and as drivers for high brightness x-ray sources. Radiofrequency (RF) acceleration methods are the workhorse for producing high energy electron beams both in high energy physics [1–3] and 4th generation light sources [4–7].

In high energy physics, lepton (i.e., positron - electron) colliders are preferred since owing to the fundamental nature of the leptons, the collision is characterized by lower backgrounds when compared with hadron colliders. Nevertheless, several energy frontier collider projects use hadrons due to the limitations on the maximum achievable energy imposed on electron rings by synchrotron radiation losses. The synchrotron radiation power [8] is described by

$$P = \frac{e^2 a^2}{6\pi\epsilon_0 c^3} \tag{1.1}$$

where $e$ is the fundamental unit of charge, $a$ is the acceleration, $\epsilon_0$ is the permittivity of free space, and $c$ is the speed of light. For a relativistic particles traveling on a constant radius trajectory, $a$ scales like $\gamma^2/R$, where $\gamma$ is the energy of the particle divided by its rest mass and $R$ is the radius of the ring. This means that the power scales as $\gamma^4/R^2$, and the energy loss per revolution scales as $\gamma^4/R$ [9], increasing quickly as $\gamma >> 1$. Electrons and positrons have rest energies of .511 MeV/c$^2$, whereas protons have rest energies of 938 MeV/c$^2$, a factor of $10^3$

larger mass. This allows hadron accelerators to reach energies in the tens of TeV with tens of km rings without limiting synchrotron losses.

Lepton accelerators overcome these radiative losses by use of linear acceleration, with the disadvantage of only having a single pass through the accelerating structures and hence they require a long linear footprint.

To reach the ultrahigh energy scale with traditional RF technology, we must construct large facilities, km-scale accelerators which can prove prohibitively expensive in terms of construction and infrastructure costs.

## 1.1 Why Develop Advanced Accelerators?

There is a practical limit to the maximum accelerating gradient that traditional rf accelerators produce due to breakdown at the cavity surface. This limit, which is on the scale of 60 MV/m for traditional rf accelerating structures is what prevents decreasing the footprint of the accelerators. For example, SLAC's 3.2 km linac accelerates electrons to 50 GeV, with an average gradient of 16 MV/m. One solution to further increase these gradients is to decrease the wavelength of the accelerating structures. An attractive option is to take advantage of the large fields associated with modern laser technology.

Although advanced accelerators currently have far less wall-plug efficiency than their rf counter parts, due to reliance on TW power lasers which typically have $< .1\%$ wall-plug efficiency, they have the potential to surpass rf systems as laser technology continues to evolve.

The goal of the development of advanced accelerators is to limit the footprint and therefore cost of energy frontier accelerators for colliders and to bring high brightness short wavelength (x-ray and gamma ray) light sources to the university lab scale where they can be used in a variety of experiments including diffraction, spectroscopy, pump-probe experiments, ultrafast science, etc.

## 1.2 Survey of Advanced Accelerators

Before we go into a detailed description of one particular scheme of laser acceleration, the Inverse Free Electron Laser (IFEL), which is the main subject of this thesis, it is useful to review the types of advanced accelerators in order to understand where IFEL fits in among them. The characteristic common to these accelerators is their goal is to create a high peak accelerating field that is phase matched with the electron beam over a long distance to allow for large energy gain, not just accelerating gradients, and to have focusing control over the electron beam as it accelerates resulting in an high quality output beam.

### 1.2.1 X-band RF Accelerators

We begin with X-band rf accelerators. Although they use radiofrequency wavelengths, these accelerators push the limits of what can be done with current rf technology. They operate in the 10 GHz range. High gradient X-band acceleration has many technical challenges including tight tolerances and fabrication practices. X-band accelerators are being planned in TeV energy positron projects such as CLIC [3], which uses beam driven cavities to power the accelerating structures and in light source development such as MEGaRay [10] [11], which uses X-band klystrons as power sources. X-band accelerators have advantages in gradient over tradition acceleration, achieving gradients of $\sim$ 100MeV/m, but are limited by breakdown at these gradients.

### 1.2.2 Dielectric Wakefield Acceleration

Next we examine the beam driven dielectric wakefield accelerator. In this scheme a high peak current relativistic electron beam passes a bore through a dielectric structured tube. The fields from the electron beam drive wakefields within the dielectric, allowing for modes that can phase match with a witness beam that

typically travels one radiation wavelength behind, extracting energy out of the wakefield. This scheme relies on near-field interaction of the THz ($10^{12}$ Hz) scale wakefields with the dielectric structures. Experiments of this scheme include E-201 at SLAC [12]. These accelerators are capable of achieving gradients on the order of GeV/m.

### 1.2.3 Plasma Accelerators

Plasma wakefield accelerators overcome the obstacle of breakdown in materials by use of a material that is already ionized. These accelerators use either high peak current electron beams or high peak power laser pulses to drive large wakefields in plasmas. In the bubble or blowout regime, the plasma electrons evacuate regions periodically, causing bubbles that of exposed background ions. In these regions there are accelerating and focusing forces that can capture plasma electrons from the back of the plasma bubble and propel (or push) them as the bubble follows the driver through the plasma. This kind of acceleration has produced the highest accelerating gradients to date: 50 GeV/m for electron driven plasma wakes as SLAC [13] and 100 GeV/m gradients for 40 TW peak power laser driven plasmas by LBNL [14]. Ultimately these accelerators will be staged with subsequent stages operating in the quasi-linear regime to preserve beam quality while accelerating to TeV energy scales.

### 1.2.4 Dielectric Laser Accelerators

In dielectric laser accelerators (DLA) complicated dielectric microstructures are fabricated to generate laser modes that can be phased matched with an electron beam. These microstructures have a spatial scale on the order of the laser wavelength, so typically hundreds of nm, but can modulate electrons' energies on the scale of keV, resulting gradients above 250 MeV/m. A proof of principle exper-

iment was performed at SLAC's NLCTA facility [15] which demonstrated these gradients, paving the way for staged DLA structures that can be printed on integrated circuits and extended for gradients over longer distances with a small footprint. The structures serve the purpose of converting the plane wave laser field into a near field which possesses a longitudinal component of the electric field with respect the electron beam that has the right phase velocity to interact with the beam. As these are high intensity near electric fields, the gradients can be limited by dielectric material breakdown.

### 1.2.5 IFEL

The free electron laser (FEL) interaction is one of the most efficient mechanisms to transfer energy from a relativistic electron beam to a radiation pulse. Coupling between transverse electromagnetic waves and relativistic electron motion is made possible in the FEL by the presence of the undulator magnetic field that bends the electron trajectories enabling the energy exchange. Synchronous energy transfer is achieved if electrons oscillations fall behind the laser wavefronts by an integer number of wavelengths for each undulation period (resonant condition). In FELs, the electrons on average lose energy to the electromagnetic wave as they propagate through the undulator field.

The same mechanism can be employed in reverse to enable laser driven acceleration of relativistic electrons. To achieve large energy gains, the IFEL resonant condition must be maintained over a large distance by tapering the magnetic field profile of the undulator in field strength and/or period as the energy of the electron beam increases. With current laser technology, the gradients available in IFEL approach GeV/m.

Ultimately IFEL is not well suited as a multistage accelerator for a collider at TeV energy scales and above as it begins to suffer from synchrotron losses above

the GeV energy scale. IFEL does, however, have a excellent qualities up to 1 GeV, including gradients on the scale of $\sim$ 200MeV/m, decent emittance preservation of the captured beam, and electron bunching that occurs at the wavelength of the laser used.

This bunching can be utilized in light source generation to create mode locked free electron laser [16] to potentially generate pulse trains in the 10 nm(XUV) and 1 Å (X-ray) wavelength regimes with each pulse length on the scale of attoseconds.

## 1.3 A History of IFEL Experiments

IFEL, first proposed by Palmer [17], then investigated by Courant, Pellegrini, and Zakowicz [18], has an experimental history that started in the 1990's after the development of the free electron laser and the realization occurred that ponderomotive resonance could be obtained with a changing energy electron beam by tapering the period and or the magnetic field strength of the undulator to allow for resonant acceleration could continue as the energy of the electron beam changed along the undulator. This section contains a brief history of IFEL experiments, a map of which can be seen in Figure 1.1.

### 1.3.1 IFELA

The history of experimental IFEL begins with the inverse free electron laser accelerator (IFELA) experiment performed at Columbia in 1992 [19]. The experiment took divided their undulator into two parts. The first part of the undulator acted as a light source oscillator due to the resonant wavelength of the undulator being at 1.6 mm and the lack of the available laser sources for 1.6 mm. The second half of the undulator was tapered from 1.8 cm to 2.25 cm. A 750 keV electron beam was injected and 9 % of the electrons were accelerated to 1 MeV resulting in an accelerating gradient of 700 keV/m.

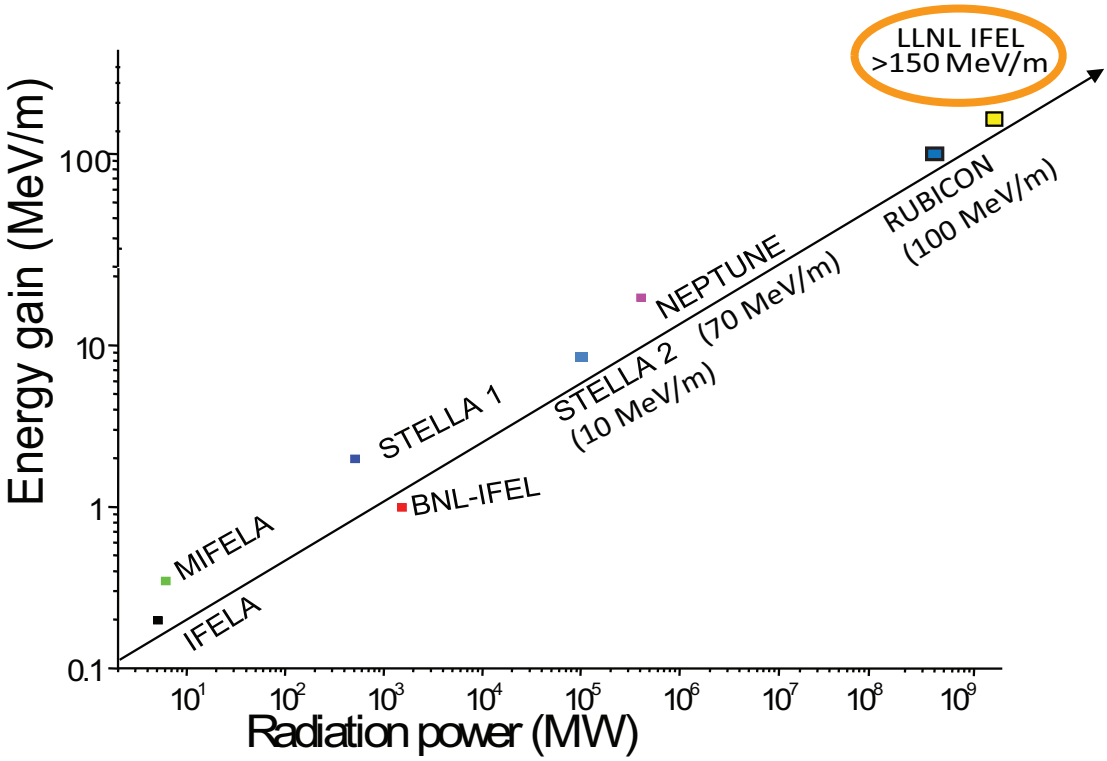


Figure 1.1: History of IFEL Experiments

### 1.3.2 BNL-IFEL

The next significant IFEL experiment was performed in 1996 at Brookhaven National Lab's(BNL) Advanced Test Facility(ATF) [20] [21]. This experiment used a 1-2 GW $CO_2$ laser focused to 1 mm beam waist, a tapered undulator with a period from 2.89 cm to 3.14 cm and magnetic field strength from 1.000 T to 1.024 T. A 40 MeV electron beam was injected into the accelerator and they were able to measure 2.3 MeV of energy gain. Moreover, they were able to study IFEL microbunching by measuring the coherent transition radiation (CTR) from a foil after the undulator then adjusting the $CO_2$ power to adjust the optimal longitudinal bunching position toward and aways from the foil [22]. The resulting accelerating gradient from this experiment was 5 MeV/m.

### 1.3.3 MIFELA

The microwave inverse free electron laser [23] explored large orbit behaviors of a pulsed helical wiggler magnet and S-band microwave in a traveling wave structure to perform detailed benchmarks of three-dimensional numerical calculations of the IFEL interaction. Although the accelerating gradient of 360 keV/m was low compared to the BNL-IFEL experiment, the use of microwave instead of optical wavelengths and the resulting large orbits allowed for accurate benchmarking of fully three dimensional IFEL codes.

### 1.3.4 STELLA

The staged electron laser acceleration experiment, (STELLA) was the first attempt to do staged IFEL. The experiment began by demonstrating multiple stage IFEL at ATF in 2000 [24]. STELLA further demonstrated in 2004 high efficiency trapping using the first staged IFEL to bunch the electron beam and the second to accelerate the beam claiming trapping efficiencies of up to 80 %, [25] and was able to demonstrate acceleration up to 8 MeV with an electron beam injected at 45 MeV and using of a >100 GW $CO_2$ laser focused such that the peak intensity in the second undulator was approximately 2 TW/cm$^2$. The main contribution of this experiment was to demonstrate that reasonably high trapping efficiencies can be achieved through prebunching of the electron beam in addition to achieving an improvement in the IFEL acceleration gradient of above 10 MeV/m.

### 1.3.5 NEPTUNE

The IFEL experiment performed at UCLA's Neptune laboratory in 2004 [26] was able to demonstrate energy gain of trapped electrons in excess of 20 MeV. By use of a 400 GW $CO_2$ laser and the KIAE-2p planar undulator [27] a 14 MeV electron beam was accelerated above 20 MeV. The undulator was designed to correct for

the Gouy phase shift that occurs through the laser's waist to maintain resonant energy exchange between the laser and electron beam throughout. Due to the aggressive undulator tapering the laser intensity at the center of the undulator was insufficient to maintain the electron beams on the resonant acceleration curve, resulting in only significant energy gain in the first half of the undulator as verified with consistent simulations. The acceleration gradient for a record of 70 MeV/m. Although the fundamental IFEL resonance is lost half way through the undulator, higher harmonics of the electron orbits became resonant toward the end of the undulator, allowing for a systematic study of the effects of higher harmonics in IFEL.

### 1.3.6 Rubicon

The Rubicon experiment [28], performed at BNL from 2013-2014, initially demonstrated gradients of $> 100$ MeV/m using a helical undulator constructed at UCLA by J.Duris et al and circularly polarized $CO_2$ laser light with 200 GW peak power. After re-tapering the undulator for a gentler accelerating gradient, large capture was demonstrated from 50 to 90 MeV with energy spread on the scale of 2 %.

### 1.3.7 LLNL IFEL

Lastly we discuss LLNL IFEL [29–31] which explores the effects of short laser pulses using 800 nm Ti:Sapphire technology with pulse lengths of 100 fs rather than the traditionally used 10.6 $\mu$m with pulse lengths of a few ps. A chapter of this dissertation is dedicated to this experiment.

## 1.4 Motivation of Dissertation

This dissertation examines the generation of high brightness electron beams in the photoinjector blowout regime and studies the effects of the IFEL interaction both at THz wavelengths as a method of compression and synchronization and at 800 nm with sub ps laser pulses as a method of high gradient acceleration with applications for gamma ray generation by inverse Compton scattering (ICS).

## 1.5 Organization of the Dissertation

This dissertation is organized as follows: We begin with an examination of the generation of high brightness electron beams in the photoinjector blowout regime. We then look at the theory of the inverse free electron laser interaction, followed by two applications of IFEL. The first application examines the interaction when the electron beam interacts with THz generated by pulse front tilt optical rectification of ultrafast laser pulses, while the second looks at high gradient acceleration by sub picosecond TW scale laser pulses at Lawrence Livermore National Laboratory (LLNL).

# CHAPTER 2

# High Brightness Electron Beams Produced in the Photoinjector Blowout Regime

A key element for a laser accelerator is the high brightness electron beam which is being accelerated. The generation of such high brightness electron beams will be the subject of this chapter.

## 2.1 Beam Development

A beam is a collection of particles with a specific set of approximations and constraints applied. Being a collection of particles it can be described using statistical mechanics. As such, the particle beam can be described by a discrete set having spatial coordinates, $\mathbf{X}_i$ , and corresponding momentum coordinates, $\mathbf{P}_i$, where $i = 1...N$, and $N$ is the number of particles in the set. Each particle in the beam can be seen as a point in a 6D space and each beam can be seen as a single point in a 6-DN space of all possible beam of N particles. We can treat the collection of particles as a density in phase space, $n_{PS}$ composed of Dirac delta functions:

$$n_{PS} = \sum_{i=1}^{N} \delta(\mathbf{x} - \mathbf{X}_i(t))\delta(\mathbf{p} - \mathbf{P}_i(t)) \tag{2.1}$$

We can then use the conservation of phase space volume as prescribed by the Liouville theorem,

$$\frac{D}{Dt}N(\mathbf{x},\mathbf{p},t)=0 \tag{2.2}$$

Where $D/Dt$ is a convective derivative with the form of

$$\frac{D}{Dt}=\frac{\partial}{\partial t}+\dot{\mathbf{x}}\cdot\nabla_x+\dot{\mathbf{p}}\cdot\nabla_{\mathbf{p}} \tag{2.3}$$

From this phase space density conservation we can construct a probability for the distribution being in phase space. The BBKGY hierarchy, which describes the dynamics of a system of a large number of interacting particles [32] can be applied to construct a recursion relation between the probability of $N$ particle interactions, $f_N$, and $N-1$ particle interactions, $f_{N-1}$. Justified by the unlikelihood of three particle interactions and higher, one can truncate the series and reduce the system down to an averaged probability distribution, $f_1$ and the effects of binary interactions, which can be reduced to a correlation function, $g(12)$. Lastly, ignoring binary interactions such as collisions, as can be done with photoinjector electron beams, one arrives at the Vlasov equation:

$$\frac{\partial f}{\partial t}+\dot{\mathbf{x}}\cdot\nabla_x f+\dot{\mathbf{p}}\cdot\nabla_{\mathbf{p}} f=0 \tag{2.4}$$

This equation seems markedly similar to that described by the Liouville theorem but there is an important subtlety, however, as $f$, previously indicated by $f_1$, is the smooth averaged distribution function, neglecting the binary and higher order interactions. Thus this equation describes the evolution of a smooth distribution in 6 dimensional space, instead of a spiky distribution of systems in 6N dimensional space. Whereas the Liouville equation described the complete forces, the $\dot{\mathbf{p}}$ term in the Vlasov equation is the average force over all of the particles (neglecting the particle in question). The Vlasov equation combined with the fields described by Maxwell's equations characterize the time evolution of the electron beam.

The distribution function can be characterized by looking at its moments. Integrating over the distribution function gives you the number of particles, $N$, while integrating over the first moment gives the centroid:

$$< \mathbf{x} >= \int_{-\infty}^{\infty} \mathbf{x} f(\mathbf{x}, \mathbf{p}, t)\, \mathrm{d}\mathbf{p}\, \mathrm{d}\mathbf{x} \tag{2.5}$$

Integration over the second moment while subtracting the average gives the variance :

$$\sigma_x^2 = \int_{-\infty}^{\infty} \mathbf{x^2} f(\mathbf{x}, \mathbf{p}, t) - < \mathbf{x} >\, \mathrm{d}\mathbf{p}\, \mathrm{d}\mathbf{x} \tag{2.6}$$

Because the beam has a relatively low energy spread and divergence, the paraxial approximation can be applied which is valid when $p_x, p_y << p_z \sim \mid \mathbf{p} \mid$, allows for the restatement of $p_x$, $p_y$, and $p_z$ into $x'$, $y'$, and $\delta p / < p_0 >$ respectively. The phase planes then are commonly known as the three trace planes. We can represent these coordinates as a six dimensional paraxial column vector for easy beam tracking calculations:

$$\mathbf{X} = \begin{pmatrix} x \\ x' \\ y \\ y' \\ z \\ \frac{\delta p}{p_0} \end{pmatrix} \tag{2.7}$$

If the force acting on the beam is linear with respect to the offset of the coordinates then the dynamics resembles that of a simple harmonic oscillator with the particles following elliptical trajectories in the trace planes, moving together and preserving the area of the distribution. These oscillations are called betatron or synchrotron motion depending if they happen to in the transverse or longitudinal

plane. Any linear force, drift or combination thereof can be represented by the following linear transfer matrix:

$$\mathbf{R} = \begin{pmatrix} R_{11} & R_{12} & R_{13} & R_{14} & R_{15} & R_{16} \\ R_{21} & R_{22} & R_{23} & R_{24} & R_{25} & R_{26} \\ R_{31} & R_{32} & R_{33} & R_{34} & R_{35} & R_{36} \\ R_{41} & R_{42} & R_{43} & R_{44} & R_{45} & R_{46} \\ R_{51} & R_{52} & R_{53} & R_{54} & R_{55} & R_{56} \\ R_{61} & R_{62} & R_{63} & R_{64} & R_{65} & R_{66} \end{pmatrix} \tag{2.8}$$

For most cases the phase planes are decoupled, meaning that the off-diagonal elements (other than between $x_i$ and $x_i'$) are zeros. Notable exceptions to this are dispersive and angular-dispersive elements which have non-zero $R_{16}$ and $R_{26}$ elements, assuming that the dispersion is in the horizontal plane. Other examples are longitudinally dispersive elements that have nonzero $R_{56}$ such as doglegs and chicanes. These elements are necessary for compression of chirped high energy beams because this element of the transfer matrix for a drift goes like $1/\gamma^2$, so it has a small value at higher energies.

In this notation, the transfer matrix can be constructed for individual elements and a single transport matrix can be constructed from the elements through matrix multiplication, following the rule, like any operator, that the earlier element that the beam encounters is on the right of the matrix chain.

For a particle with initial 6-D trace space coordinates, $\mathbf{X}_i$, we can then use the total $R$-matrix to determine its final propagated coordinates:

$$\mathbf{X}_f = \mathbf{R} \cdot \mathbf{X}_i \tag{2.9}$$

The size of the area occupied by the beam in trace space is known as the emittance. The transverse RMS emittance are defined in the paraxial coordinates

as:

$$\epsilon_{x_i} = \sqrt{< x_i^2 >< x_i'^2 > - < x_i x_i' >^2} \tag{2.10}$$

If the beam experiences acceleration, the RMS emittance will decrease due to the longitudinal momentum increasing, which has the effect of scaling down the beam angles, $x'$ and $y'$, proportional to $\gamma\beta$. As we are interested in a constant of the motion for the propagation, we can introduce the normalized emittance,

$$\epsilon_{n,x_i} = \gamma\beta\sqrt{< x_i^2 >< x_i'^2 > - < x_i x_i' >^2} \tag{2.11}$$

The normalized emittance appears as a nonlinear term in the beam envelope equation which describes how the second moment described by Equation 2.6 evolves along z:

$$\frac{\mathrm{d}^2\sigma_x}{\mathrm{d}z^2} + \frac{(\beta_0\gamma_0)'}{\beta_0\gamma_0}\frac{\mathrm{d}\sigma_x}{\mathrm{d}z} + \kappa_x^2\sigma_x = \frac{\epsilon_{n,x}^2}{(\beta_0\gamma_0)^2\sigma_x^3} + \frac{2I}{I_0\beta_0^3\gamma_0^3\sigma} \tag{2.12}$$

where $\kappa$ is the focusing forces due to external fields in the lattice, $(\beta_0\gamma_0)'/(\beta_0\gamma_0)$ is the acceleration, $I$ is the peak beam current and $I_0$ is the characteristic or Alfven current, which is 17 kA for electrons. This equation resembles that of a damped driven harmonic oscillator with two nonlinear terms, one that is proportional to the square of the normalized emittance and the other one (representing space charge forces) that is proportional to the peak current. As the beam becomes increasingly relativistic we can see that the space charge term will decrease faster than the emittance term so that at high energy the evolution of the beam size is dominated by the emittance and one can neglect effects due to space charge forces.

The normalized longitudinal emittance can be defined as,

$$\epsilon_z = \frac{\sqrt{< \delta z^2 >< \delta p^2 > - < \delta z \delta p >}}{m_0 c} \tag{2.13}$$

The RMS emittances represents the area of ellipses in trace space enclosing the particle distribution. These ellipses change orientation and perform rotations under linear transformations but never change in area, reflecting the fact that the emittance is preserved under linear transformations.

A good figure of merit for beam quality is the six-dimensional beam brightness, which can be seen as an RMS 6D trace space density. As opposed to the commonly used four-dimensional brightness, the six-dimensional brightness includes the longitudinal emittance, a figure that describes the compressibility of the beam as it relates to energy spread. The 6-D brightness is given as:

$$B = \frac{N}{\epsilon_x \epsilon_y \epsilon_z} \tag{2.14}$$

The 6-D brightness is also useful as there are several emittance exchange schemes, where longitudinal and transverse emittances can be swapped, resulting in smaller transverse emittance and therefore a potentially tighter focus at the exchange of compressibility or energy spread.

If the explicit time derivative of the Vlasov is zero, the solutions to the modified equation will describe equilibrium states. Assuming separability of the distribution function into three phase plane functions, as well as that each of those functions are separable in coordinates and momenta, we can solve the equilibrium Vlasov equation and arrive at the bi-Gaussian distribution for each phase plane:

$$f_{biGaussian}(x_i, x_i') = \frac{1}{2\pi\sigma_x\sigma_{x'}} \mathrm{Exp}\left[ -\frac{x^2}{2\sigma_x^2} \right] \mathrm{Exp}\left[ -\frac{x'^2}{2\sigma_{x'}^2} \right] \tag{2.15}$$

The bi-Gaussian distribution in each trace plane gives a noninteracting equilibrium solution to the Vlasov equation and is self similar through linear transformations, and a great deal of research goes into the design of both magnets and

RF accelerating sections to make the forces experienced by the beam as linear as possible. The self-forces due to space charge from a beam with the bi-Gaussian distribution are, however, very non-linear resulting in phase space area (and thus emittance) growth. Consequences of these nonlinearities include beam halo and general phase space dilution of charged particle beams as they propagate through and accelerating beamline.

The bi-Gaussian distribution is not the only solution to the Vlasov equation. One of particular interest to the beam community is the Kapinchski-Vladimirski(KV) distribution [33], which is that of a uniformly filled ellipsoidal beam. The density within the ellipsoid is constant, i.e. $\rho_0 = 3Ne/4\pi ABC$ for an ellipsoid with a constraining boundary of

$$(\frac{x}{A})^2 + (\frac{y}{B})^2 + (\frac{z}{C})^2 = 1 \tag{2.16}$$

Solving the electrostatic problem for a uniformly filled ellipsoidal distribution, the electric field seen by the beam in the rest frame is linear. Consequently the there is no emittance growth due to the nonlinearities of the space charge field while the beam propagates, making this distribution ideal for preserving beam quality throughout propagation through a linear lattice.

This has motivated the beam community to experimentally create such a distribution right from the start, that is, in the photoinjector.

One technique for producing this distribution is to shape the laser profile that is applied to the photocathode to have an intensity profile such that the electron beam distribution at the cathode will become an ellipsoidal beam. This method is complicated and expensive, reflecting the qualities of laser pulse shapers.

In the rest of this chapter we will discuss a different method based on illuminating the cathode with an ultrashort laser pulse and relying on the space charge forces to obtain a nearly ideal uniformly filled ellipsoidal distribution.

## 2.2 Photoinjector Blowout Regime

A more attractive option to produce the distribution takes advantage of the ultrafast rearrangement of the beam as it expands longitudinally under the influence of strong space-charge forces. Luiten et al. [34], reconsidering an idea proposed by Serafini [35], have shown that to obtain a final ellipsoidal distribution there is essentially no requirement on the initial laser pulse shape other than it be much shorter than the final bunch length after expansion. This has motivated the use of a "pancake regime" where the only requirement of the laser profile on the cathode is that the transverse to longitudinal aspect ratio is large, $\sigma_r >> \sigma_z$

With the advent of chirped pulse laser amplification (CPA) [36] production of sub-picosecond laser pulses has become routine making possible to realize the large aspect ratio of the laser required for the photoinjector blowout regime.

### 2.2.1 Experimental Generation, Observation, and characterization of Uniformly Filled Ellipsoidal Electron Beam: Methodology

The generation and characterization of a near uniformly filled ellipsoidal electron beam was performed at UCLA's Pegasus [37]. Other than the photoinjector blowout beam studies, this lab has focused on advanced accelerator diagnostics such as electro-optic sampling [38] with applications in ultrafast electron diffraction [39]. A diagram of the setup experimental beamline can be seen in Figure 2.1.

The experiments were performed using a Coherent Inc. Titanium:Sapphire Laser system capable of generating pulses with a central wavelength of 800 nm that have a 40 fs FWHM as measured by a single shot autocorrelator . This laser is frequency tripled using nonlinear optical elements to pulses with a central wavelength of $\sim$200 nm and temporal RMS of 35 fs. An ultraviolet laser pulse is used to overcome the work function of the copper cathode of a 1.6 cell SLAC/BNL/UCLA photoinjector gun driven at 2.856 GHz. The transverse laser

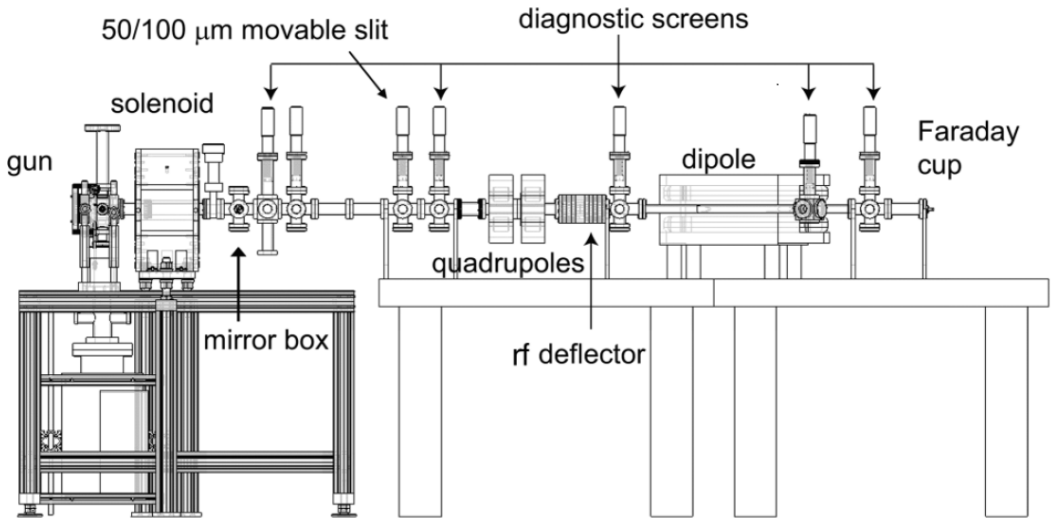


Figure 2.1: Layout for Photoinjector Blowout Regime Beam Measurements. An X-band deflecting cavity and a dispersive spectrometer allows the longitudinal spatial profile and phase space to be measured.

profile is shaped by overfilling a Gaussian mode imaged 1 mm pinhole aperture onto the cathode. This cut Gaussian distribution results in an good approximation of $\sqrt{1-(r/a)^2}$ for r $\leq$ a, where r is the radial cylindrical coordinate and a is the fixed constant radius. This is the ideal radial profile prescribed by Luiten, as it represents radial density of the thin disk resulting from the collapse of an astronomical uniformly filled ellipsoidal object. As the gravitational and electrical forces only differ by sign, (i.e. repulsive vs. attractive), this distribution is the best place to start to obtain a uniformly filled ellipsoidal distribution upon expansion. The expansion occurs as the electron beam is accelerated by the gun to a final energy of 3.75 MeV. As the electron beam accelerates the space charge force is reduced by a factor of $1/\gamma^2$ or $\sim$50, effectively freezing the dynamics (and the evolution of the distribution) at the gun exit. A solenoid, typically used for emittance compensation techniques [40] is used as a lens to collimate the electron beam as it travels to the deflecting cavity. A 50 or 100 $\mu$m slit serves to cut the electron beam in the deflecting cavity plane, thereby increasing the resolution of

the temporal measurement.

The deflector is a 9 cell standing wave cavity driven at 9.599 GHz with a maximum deflecting voltage, $V_0$ of 500 kV. The deflector, designed by R.J. England [41],operates in a $TM_{101}$ mode. The effects of the deflector can be modeled as a linear transformation on the beam distribution using a thin kick model for the deflecting cavity. This linear transformation has a representation of a 6x6 $\mathbf{I}$ matrix with the exception of the $R_{45}$ and $R_{63}$ elements are $\frac{eV_0}{m_0 c\gamma} \times \frac{2\pi\nu}{c}$, where $c$ is the speed of light, $e$ and $m_0$ are the electron charge and mass and $\gamma$ is the Lorentz factor. As such, it imparts a linear correlation between the longitudinal position in the beam, $z$, and the vertical position detected on the downstream fluorescent screen, $y$. After a drift of 17 cm between the center of the deflector and the imaging screen,a proportionality factor of $K \simeq$ 1.1 fs/$\mu$m is determined between the transverse position at the screen and the longitudinal position in the deflector.

To obtain synchronization between the electron beam and the deflecting voltage, the low level reference signal for the deflector at 9.599 GHz is obtained multiplying the 79.333 MHz laser oscillator master clock by 121, i.e. phase locking the laser pulses with the RF cavity. The RMS temporal jitter of the X-band signal with respect to the laser pulse's time of arrival introduced by this multiplication is $\sim$ 1 ps. This results in a significant ($\sim$ 1 mm) vertical jitter of the beam position on the screen thus preventing collection of data by simple integration over multiple shots. For the measurements presented here a post-processing routine selected data only from images for which the beam centroid was $< 100$ $\mu$m from the beam line axis.

The vertical RMS beam size observed on the downstream screen can be approximately written as the quadrature sum of the contribution due to the deflection and the minimum RMS spot size achieved when the cavity voltage is off, that is $\sigma_y = \sqrt{\sigma_0^2 + (K\sigma_z/c)^2}$ where $\sigma_z$ is the RMS bunch length. In order to resolve the

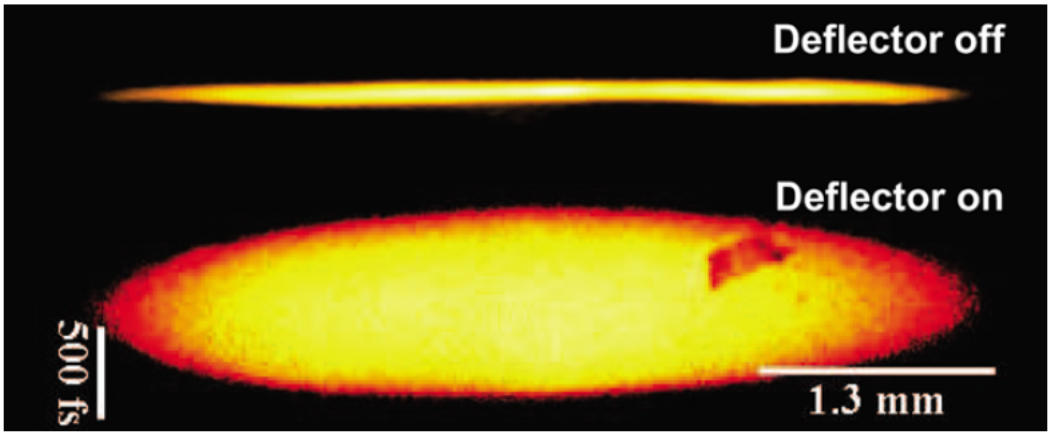


Figure 2.2: Image of deflected electron beam at diagnostic screen immediately after deflecting cavity. (Top) Image with deflector set to zero voltage. (Bottom) Image with cavity set to maximum voltage, resulting in a streak with 50 fs resolution.

time structure of the bunch, we require that the contribution to the vertical spot size due to the t-correlated deflection be much greater than $\sigma_0$. The minimum measurable bunch length (which sets the temporal resolution) is given by $\sigma_0/\mathrm{K}$.

There are two methods employed for the minimization of $\sigma_0$ prior to turning on the deflecting voltage: One relies on focusing with a quadrupole lens and the second is obtained by selecting only the central beam slice by collimation using a horizontal slit. The information extracted from these different configurations is complementary, as in the former method we measure the full beam distribution projected into 2D, while using the latter method we measure only a nearly 2D slice extracted from it.

By employing the vertically focusing quadrupole just upstream of the rf cavity we focused the beam down to a thin ($\sigma_0 < 40$ $\mu$m thick) horizontal line on the measurement screen, yielding a temporal resolution better than 50 fs. The streak images obtained both before and after the 500 kV deflecting voltage is turned on, for the beam parameters given in Table 2.1, are shown in Figure 2.2. Since the

| Blowout Experimental Parameters | |
|---|---|
| Beam energy | 3.75 MeV |
| Peak field at the cathode | 80 MV/m |
| Photoinjector injection phase | 25 deg |
| Laser spot size (RMS) | 400 $\mu$m |
| Laser pulse length (RMS) | 35 fs |

Table 2.1: Pegasus photoinjector parameters

initial y-betatron size is negligible, there is an almost perfect correlation between the y axis and time. Thus one of the most striking features is the sharp ellipsoidal beam boundary which encloses the particle distribution function projected onto the x-t plane. This direct verification of the ellipsoidal boundary provides a strong validation of the theoretical prediction of dynamical formation of ellipsoidal beams through ultrashort laser pulse cathode illumination.

#### 2.2.1.1 Discussion of Blowout Measurement Results

The sharpness of the distribution boundary in t is predicted to be limited by the initial spread in emission times. The measured bunch length is 300 fs RMS in good agreement with particle tracking simulations performed using the ASTRA beam dynamics code [42]. Even including the possible delay time associated with photoemission, the beam distribution has stretched by almost an order of magnitude. We then expect that it would show little memory of its initial size; the sharp density transition at the boundary verifies this expectation.

The intensity distribution inside the ellipse of Figure 2.2 merits further consideration. Since the quadrupole lens focuses the beam in the vertical direction (y), effectively projecting the beam distribution along this axis, we expect an intensity distribution resembling the projection of a uniformly filled ellipsoid onto the x-z plane. In other words if the beam distribution, $\rho(x, y, z)$ is constant and differs

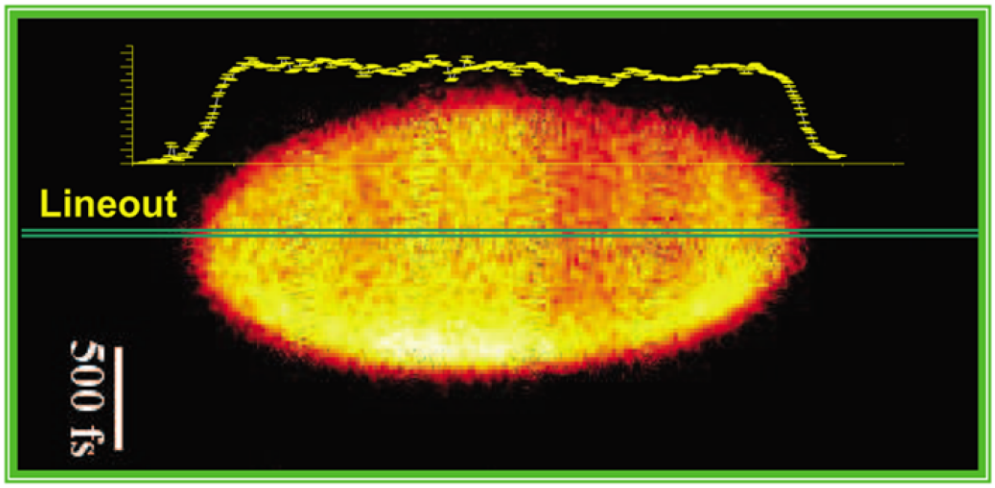


Figure 2.3: Blowout beam X-Z spatial distribution measurement with a lineout demonstrating the expected behavior of a near-uniformly filled ellipsoid: Flat top with fast falling edges.

from zero only for $\frac{x^2}{a^2}+\frac{y^2}{b^2}+\frac{z^2}{c^2}<1$ where a, b, c are the three semiaxes of the ellipsoidal, on the screen one should observe an intensity distribution proportional to the projection of $\rho$ onto the $(x,z)$ plane, $f(x,z)=\int \rho(x,y,z)\,\mathrm{d}y \propto \sqrt{1-\frac{x^2}{a^2}-\frac{z^2}{c^2}}$. This prediction is verified in Figure 2.4, where a surface plot of the pixel intensities from Figure 2.2 is compared to the ideal distribution $f(x,z)$.

In the original proposal of the radial shape of the initial transverse laser profile is deemed critical for creating the ellipsoidal beam. However, in our measurements the initial laser transverse profile has been shaped by simply imaging onto the cathode an iris of aperture $r_a$ illuminated with a larger Gaussian laser spot of measure. We observe in t-dependent beam images that the shape of the final beam distribution is not particularly sensitive to the initial transverse profile, as long as this one has sharp edges. Only when the laser transverse profile presents long tails, i.e., when the laser is apertured at a radius $r_a > 1.5\ \sigma_g$, does the beam lose its characteristic sharp ellipsoidal boundary.

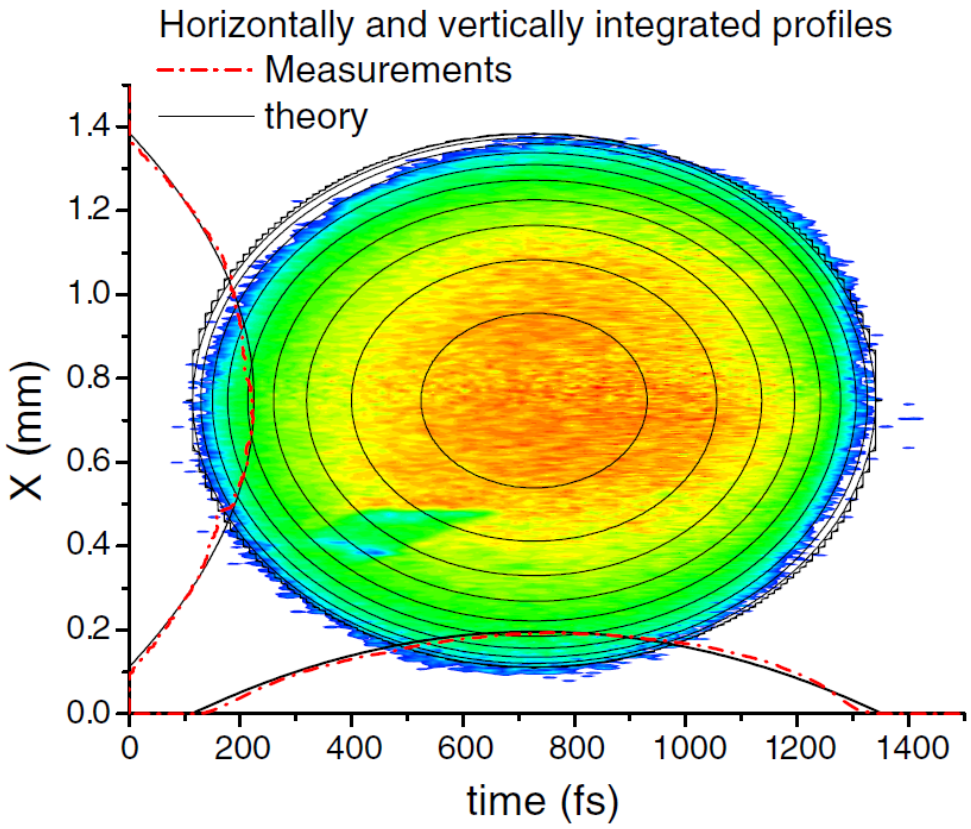


Figure 2.4: X-Z distribution integrated with model superimposed.

This mild dependence on the initial laser transverse shape is in good agreement with particle tracking simulations. It originates in the details of the dynamics of the beam rearrangement. A half-circle initial distribution would be required if the beam expansion were entirely longitudinal. However, because of relativistic dilation the beam rest-frame aspect ratio (i.e. the ratio between the transverse and longitudinal beam sizes) grows very quickly to be of order unity. Hence the space-charge driven expansion and distribution rearrangement take place both radially and longitudinally, leading to an ellipsoidal boundary that is not critically dependent on the details of the initial conditions.

### 2.2.2 Longitudinal Phase Space Measurement

The measurement of the longitudinal phase space (LPS) of the blowout beam exploits the two dimensional nature of the images obtained with the rf deflector, where the horizontal coordinate can be used to encode any information whose variation along the bunch temporal coordinate is under study. Examples include the position and amplitude of a Bragg diffraction peak for ultrafast electron diffraction studies, or the beam size after a horizontally focusing quadrupole for slice emittance measurements [43]. In this section we discuss the measurement of the longitudinal phase space of the blow-out beam where we utilize the unstreaked dimension to display the momentum spectrum of the beam after it is dispersed by a magnetic dipole.

The dipole magnet employed has a design bend of 45 degrees and a radius of curvature of 0.67 m. After a longitudinal distance of 29 cm from the exit of the dipole, chosen in order to maximize the energy resolution and acceptance, the transverse x-y profile of the beam containing the mapped longitudinal phase space is imaged onto a 1 inch diameter yttrium aluminum garnet (YAG) fluorescent screen from Radiabeam Technologies IBIS profile monitor. The emittance compensation solenoid is employed to guide the beam to a very gentle focus a few meters downstream of the cathode. A 100 $\mu$m wide horizontal aperture at a distance 1 m downstream from the cathode is used to select a central slice of the beam to perform the measurement. The need for this experimental procedure arises from consideration of the effects of the deflecting electromagnetic field on the beam energy distribution and it is discussed in detail in the next section. The small aperture reduces the charge to $< 5$ % of its initial value, thus effectively stopping any further space charge driven dynamical evolution, as confirmed by GPT simulations. For photoinjector parameters typical of the measurements described here, in the region after beyond 1 m downstream of the cathode the energy spread would slightly (10 %) increase. When the collimating slit aperture is in-

serted in the beam path,however, the simulated energy spread remains constant. This can be explained noting that even though the local charge density remains unmodified by the aperture, the beam aspect ratio and hence the magnitudes of the space charge forces in the transverse and longitudinal direction are strongly affected.

The only longitudinal phase space transformation that takes place after the slit is a drift propagation up to the deflecting cavity plane where the beam longitudinal profile gets imprinted by the transverse deflecting kick into the vertical plane.

Two quadrupole magnets of effective length $L_q$ of 10.4 cm located, at respective longitudinal positions of 1.54 m and 1.66 m from the cathode are used to minimize the betatron beam sizes both in x and y at the measurement screen. The measured y-spot size on the YAG screen is $< 100$ $\mu$m Obtaining a well resolved LPS measurement requires that these beam sizes be small compared to the streaked and dispersed spot dimensions.

For the LPS measurement there is a drift of L = 110 cm from the center of the deflecting cavity to the imaging screen. The voltage applied to the deflector was $V_0 = 100$ kV, resulting in a proportionality factor was $K = 6.3$ fs/$\mu$m. Taking into account a camera calibration of 31 $\mu$m/pixel, the calibration value is 16 fs/pixel. This value is cross-checked with a direct measurement of the calibration factor obtained by lowering the deflecting voltage to a level in which a full phase sweep of the rf field can be observed on the measurement screen. The vertical centroid of the beam is then measured as a function of the phase of the deflecting cavity. The slope of the resulting sinusoidal variation at the zero crossing yields the pixel to phase calibration. The slope is then scaled by the ratio of the operating voltage and the phase sweep voltage as measured with an independent power meter and finally divided by kc to obtain the time calibration for a single pixel on the CCD. For the LPS vs charge measurement case, this method yielded a $(15 \pm 1)$ fs/pixel calibration in close agreement with the predicted value.

The screen momentum calibration can be estimated using linear matrix transport analysis. The horizontal deviation from the design trajectory due to dispersive terms is

$$x = [\rho(1 - \cos\theta_b) + L_d \sin\theta_b]\frac{\delta\gamma}{\gamma} \tag{2.17}$$

where $\rho$ is the bending radius, $\theta_b$ the bending angle, and $L_d = 29$ cm is the drift distance from the exit of the dipole to the imaging screen. Again, taking into account the camera magnification, this gives a 270 eV/pixel calibration. In order to verify this experimentally we measured the shift in the horizontal centroid of the beam when varying the magnetic field in the dipole magnet by a small amount, noting that a small variation $\delta B/B$ is equivalent to $-\delta p/p$. A linear fit gives $(0.0073 \pm 0.0003)\%$ pixel calibration factor. For a central beam energy of $(3.55 \pm 0.05$ MeV this corresponds to $(260 \pm 10)$ eV/pixel in close agreement with our estimate.

Applying the calibrations discussed above to the raw image data from the digital camera, a direct measurement of the longitudinal phase space beam distribution is obtained. In order to simplify the description of the physics of the blow-out regime, we break down the characterization of the LPS to a few essential physically relevant parameters. These are the energy chirp that describes the correlated energy spread of the beam denoted by C, the RMS energy spread ($\sigma_{\mathrm{dE}}$), the RMS bunch length ($\sigma_{\mathrm{t}}$), the slice or uncorrelated or slice energy spread ($\sigma_{\mathrm{dE_s}}$), and lastly the longitudinal phase space area or longitudinal emittance ($\epsilon_{\mathrm{z,n}}$). Depending on the application each one of these parameters may be more important than the others. Ultimately, only the complete phase space distribution fully describes the beam, but these parameters can give insight into important physical processes inherent to the photoinjector blow-out regime.

The image analysis is performed by a routine that starts by filtering the raw

image data. As in transverse phase space reconstruction measurements, filtering the noise is a critical issue in determining the phase space area. The only difference in this case is that the raw image (with proper calibration applied) directly carries the longitudinal beam distribution information. As this method involves no numerical reconstruction in the data except rescaling the axes from x-y to p-z, the filtering problem is simplified. The filtering method proceeds as follows. An upper limit threshold is first applied to eliminate any saturated pixels that have resulted from x rays hitting the imaging camera CCD. After selecting a region of interest, an iterative RMS cut is applied line by line until the computed beam RMS values converge within a threshold of 0.1%. Finally, the filtered image is integrated in the two transverse dimensions over the region of interest. A lower bound threshold is applied until the total integrated intensity is decreased to 90% of its initial value to eliminate the noise contribution at the tails of the beam profile.

The beam chirp (C) is determined by slicing the beam in 50 fs slices for one RMS bunch length around the beam centroid. The centroid of each slice is then computed and slope is determined by a linear least squares regression. The thickness of the distribution in each slice gives a local measure of the uncorrelated energy spread. The RMS bunch length and energy spread are calculated by projecting the full image intensity distribution on the two correspondent axes.

#### 2.2.2.1 Complication to LPS measurement: Panofsky-Wenzel Theorem

The most substantial source of systematic error in our measurement setup is the deflecting cavity. Use of a deflecting cavity to measure the longitudinal profile of an electron beam imposes an additional energy spread for off-axis particles. This additional energy spread is well described by the Panofsky-Wenzel theorem which in its differential form can be written as

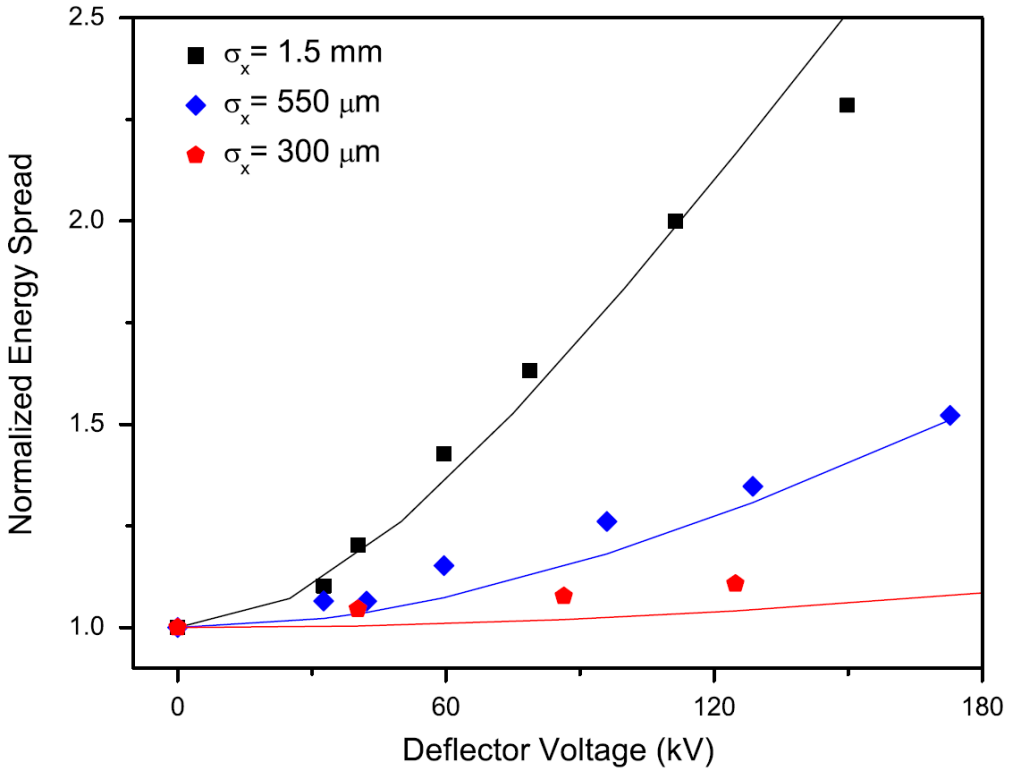


Figure 2.5: Plot of energy spread induced by the deflecting cavity as a function of transverse spot size through the deflector.

$$\nabla_{\perp}(\Delta p_z) = \frac{\partial(\Delta \mathbf{p}_{\perp})}{\partial z} \tag{2.18}$$

Equation 2.18 indicates a relationship between the transverse momentum imparted to particles that are longitudinally off the center of phase of the beam, and the longitudinal momentum imparted to particles that are transversely off center of the axis of symmetry. When applied to a deflecting cavity the Panofsky-Wenzel theorem implies that the same factor that causes the deflection of the beam induces an increase in energy spread which depends on the transverse beam width inside the deflecting cavity. By using a thin kick approximation, the energy change of an off-axis particle due to the rf fields of the deflector can be written, following Equation 2.18, as

$$\frac{\mathrm{d}\gamma}{\gamma} = \frac{keV_0}{\gamma m_0 c^2 \beta} y \tag{2.19}$$

where y is the vertical particle position. The rest of the parameters are the same as those of Equation 2.18. When applied to the second moment of the beam distribution, Equation 2.19 describes the expected increase in energy spread in terms of the RMS vertical beam size at the deflecting cavity. An experimental study of the effect of energy spread imposed upon the electron beam by the deflecting cavity is shown in Figure 2.5. A measurement of the increase in energy spread as a function of vertical spot size was performed by using the solenoid as a lens to change the transverse profile of the electron beam as it traveled through the deflecting cavity. The energy spreads for each spot size in Figure 2.5 were normalized by the energy spread measured without any deflecting voltage, as changing the beam focusing has also an effect on the beam energy spread. The data is compared with the normalized quadrature sum of the measure initial energy spread and the induced contribution calculated using Equation 2.19. The data is in good agreement with the kick model for the deflecting cavity, demonstrating the effect predicted by the Panofsky-Wenzel theorem on the beam energy spread. This study motivated the use of an aperture in order to minimize the beam transverse dimensions in the deflecting cavity. Because of the deflecting mode field profile, the field gradient is maximum in the vertical axis and minimal along the horizontal axis. Hence, a horizontal aperture is used to minimize the induced additional energy spread. When the 100 $\mu$m wide slit is inserted, the energy spread of the beam on the spectrometer screen increases by approximately 600 eV with the deflector turned on at 100 kV with respect to the unstreaked beam. Although this value may be negligible when considering the total energy spread of the beam, the contribution from the deflecting cavity constitutes an additional uncorrelated energy spread, which limits the resolution of the measurement of this parameter at about 1 keV. Given the low charge, the beam distortions that could arise

from wakefields produced by the interaction between the beam and the slit are negligible.

### 2.2.3 Longitudinal Phase Space Measurement Results

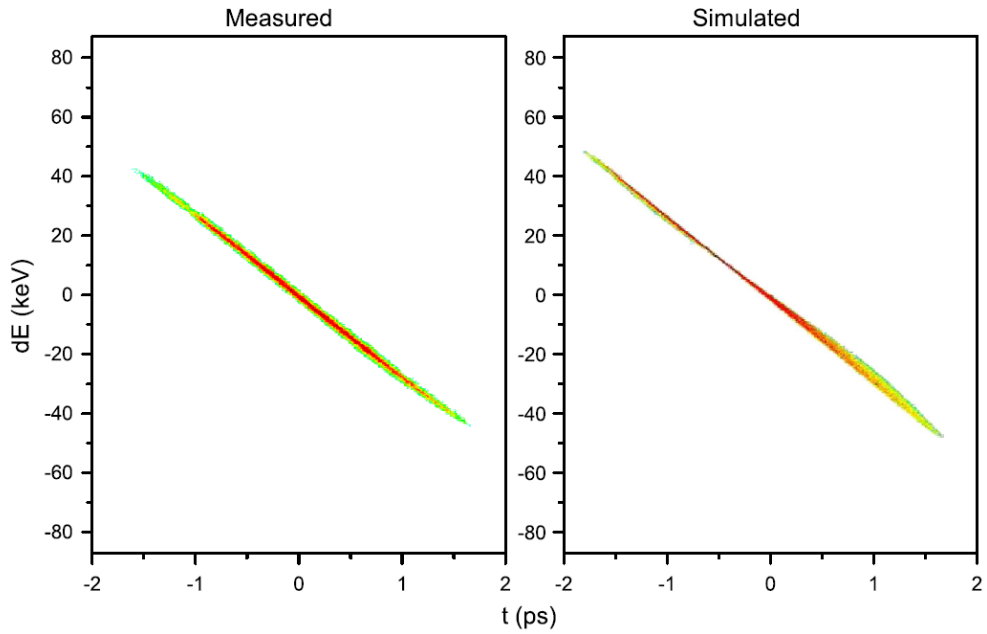


Figure 2.6: Linear Longitudinal Phase Space (LPS) Measurement. (Left) Measured LPS distribution. (Right) Simulated LPS distribution.

A direct measurement of the LPS of a typical beam generated by the Pegasus photoinjector operated in the blow-out mode mode of operation is shown in Figure 2.6. For this measurement the laser spot on the cathode was 500 $\mu$m RMS, RF gun launch phase 22 degrees, and a charge of 20 pC. The measured LPS is quite linear and has a very low longitudinal emittance. These results are expected for the uniformly filled ellipsoidal beam distribution, which is characterized by space charge forces being linear as a function of all three coordinates measured from the bunch center. For photoinjector operating modes which involve the use of longer laser pulses on the cathode ($>$ 3 ps), the LPS beam distribution would be

characterized by a significant second order component due to the RF curvature. In the blow-out case, due to the linearity of the dynamics, it is the thickness of the energy distribution at a constant time relative from the bunch center, or uncorrelated energy spread, which determines the final longitudinal emittance. For this reason, the resolution of the LPS, which sets a limit on the minimum recordable linewidth is crucial in this measurement. The measured longitudinal emittance for the case shown in Figure 2.6 is $(0.5 \pm 0.1)$ mm-mrad. We observe that the high beam quality of the phase space implies the feasibility of very large compression ratios.

In order to benchmark our understanding of the beam evolution, we compared the measurement with particle tracking simulations from GPT. The simulations start from the cathode and use a 2.5D field map for the rf gun and the on-axis magnetic measurement map for the emittance compensation solenoid. The beam dynamics is followed by GPT up to the slit plane. At this point a linear drift propagation matrix transformation up to the rf deflector plane is applied to the particle coordinates. Spacecharge forces are not taken into account for this region of propagation as the slit has removed most of the beam charge.

We compare the resulting particle coordinates in the time-energy plane with the data. The simulation results obtained with GPT are also shown in Figure 2.6 and are in remarkably good agreement with the data. There are essentially no free parameters in the simulation as the initial transverse and longitudinal spot size are taken from the laser measurements. A small degree of uncertainty is given by the nonuniform emission at the cathode which alters the beam spatial distribution and can thus affect the creation of the final state, causing some deviation from a uniformly filled ellipsoidal beam.

In Table 2.2 we summarize the longitudinal phase space parameters measured and compared with the simulation. A significant characteristic of the measured longitudinal phase space is the strong correlation between energy and position

| Parameter | Simulated | Measured | Unit |
|---|---|---|---|
| Chirp (C) | 91 | 90 ± 1 | keV/c mm |
| $\epsilon_{z,n}$ | 0.3 | 0.5 ± 0.1 | mm-mrad |
| $\sigma_{dE}$ | 22 | 21 ± 2 | keV |
| $\sigma_t$ | 797 | 788 ± 8 | fs |

Table 2.2: LPS Parameter Comparison

along the bunch, i.e., energy chirp which is quantified with the chirp parameter C = 90 keV/(c mm) . This large correlation is due the final beam state being the result of a strong space charge driven expansion so that particles at the head of the beam have been pushed further and hence have higher energy. In order to obtain an analytical estimate, we observe that in the pancake approximation limit, the bunch length is given by $\tau = m_0 c\sigma/e\epsilon E_0^2$, where $\sigma = Q/(2\pi\sigma_l^2)$ is the surface charge density at emission and $E_0$ the accelerating gradient. The beam energy spread in the same approximation is given by $m_0c^2\Delta\gamma = e\sigma L_s/\epsilon_0$ , where $L_s = 5$ cm is the length over which the space charge forces act. $L_s$ gives a good estimate for the propagation region where the expansion takes place has been taken from the simulations as the point where the aspect ratio in the beam rest frame changes from an oblate to a prolate ellipsoid. In the drift region following the gun, the energy spread stops increasing since the beam has become long in its rest frame and the residual elongation comes from the previously imprinted difference in beam velocities. The final bunch length is $\tau_f = \tau + \Delta\gamma L_d/\gamma^3 c$, where $L_d$ is the drift length to the deflecting cavity plane.

The resulting final chirp is

$$C \simeq m_0c^2\frac{\Delta\gamma}{c\tau_f} \sim 85\ \frac{keV}{mm} \tag{2.20}$$

This value is in close agreement with that which was found experimentally.

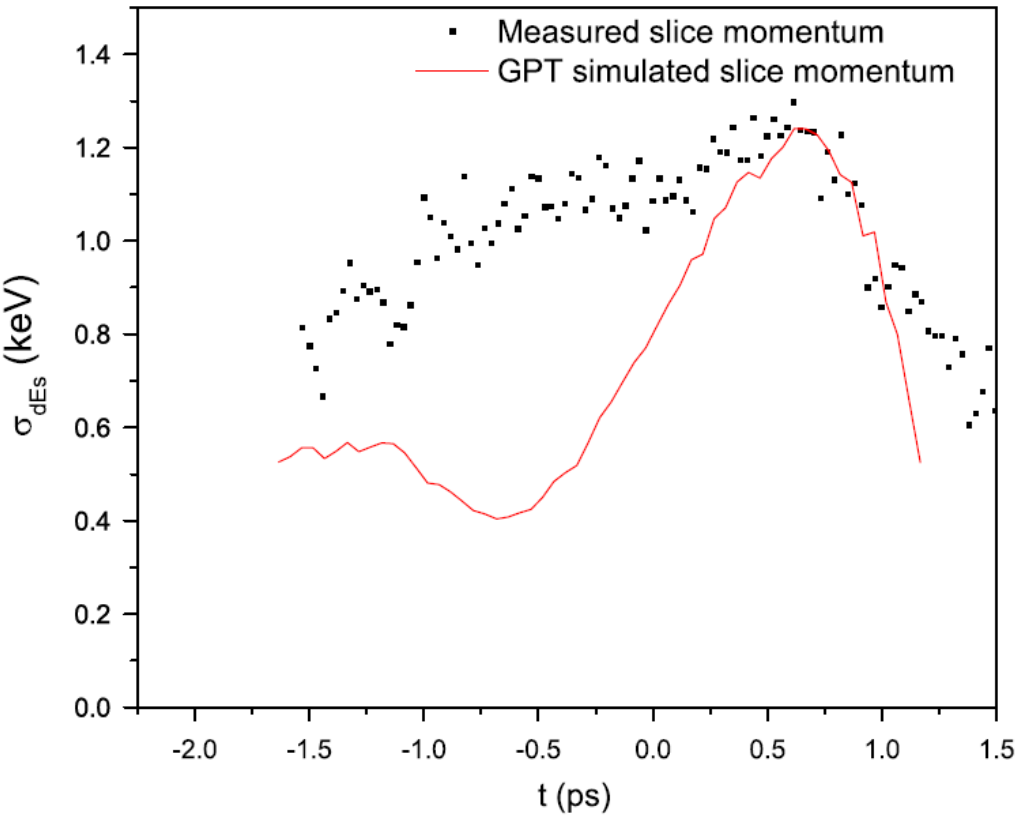


Figure 2.7: Determination of longitudinal slice energy spread. The resolution is determined to be 1 keV.

#### 2.2.3.1 Longitudinal Slice Emittance Measurement

By calculating the RMS energy spread on 50 fs temporal slices we obtain the result shown in Figure 2.7 which displays the local slice or uncorrelated energy spread along the bunch. This quantity determines how cold the beam distribution is locally and is a critical beam parameter for many applications since it determines the growth rate of any beam instability, both desired like FEL amplification and harmful to the beam quality such as, for example, coherent synchrotron radiation instability. In current short wavelength FEL injector designs, a laser heater is usually introduced in the beam line to be able to externally control the uncorrelated energy spread and damp the undesired instabilities.

Examining Figure 2.7 we note that, although we cannot resolve the small local slice energy spread of the central region of the beam, the measured slice energy spread follows the simulation for values larger than 1.0 keV. This is an indication of the resolution of the measurement. The 1.0 keV measured slice energy spread corresponds to a 0.027 % relative energy spread and is, in absolute value, the lowest uncorrelated energy spread measured to date from an rf photoinjector beam.

We note that this is still much larger than the thermal spread of the particles coming out of the cathode. Consequently, the measured longitudinal emittance is at least 2 orders of magnitude larger than the thermal limit (in striking contrast with transverse emittances obtained from rf photoinjectors that are within a factor of 2 from the corresponding thermal limit).

The source of the uncorrelated or slice energy spread is primarily due to radial-energy correlations in the beam dynamics. The space charge field of a uniformly filled ellipsoidal charge distribution has ellipsoidal equipotential surfaces and hence a slice (a plane at constant z) contains particles at different energies. This accounts for most of the keV-level slice energy spread seen in the measurements and simulations.

Another effect which has to be taken into account is the radial dependence of the rf accelerating field. The energy spread calculated from GPT simulations for the photoinjector gun operating at a 100 MV/m gradient was found to be 1 keV RMS energy spread per 1 mm RMS laser spot size on the cathode. This quantity is proportional to the square of the RMS laser spot size, so for a 400$\mu$m RMS spot size at the cathode (Pegasus nominal parameter value) this contribution is $< 0.2$ keV.

An estimate for the resolution can be obtained by measuring the vertical spot size before turning the rf deflector on for streaking. With the proper quadrupole settings, the spot size is found to be 87 $\mu$m RMS or 2.8 pixel RMS. Taking into account the large beam chirp of 90 keV/c mm or 30 keV/ps, this accounts for

1.1 keV energy uncertainty in agreement with the limit set by Figure 2.7.

#### 2.2.3.2 Electron Beam Chirp Studies

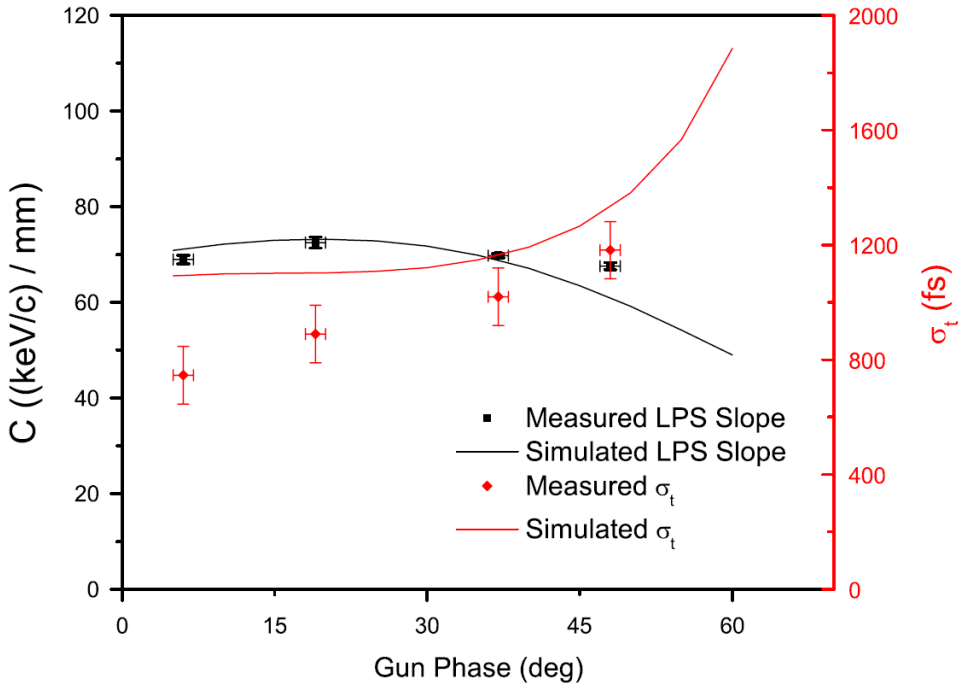


Figure 2.8: LPS Chirp as a function of rf gun phase.

We have further characterized the behavior of the longitudinal phase space as a function of various photoinjector parameters. In Figure 2.8 the variation of the main LPS parameters obtained by changing the injection phase is shown. Both the RMS bunch length and the energy chirp show a very weak dependence on the rf phase. By lowering the laser launch phase the gun acts as an RF compressor. This behavior is not clearly observed in the case of a very short laser pulse illuminating the cathode due to the RF focusing effect being small for a very short beam in addition to the large amplitude longitudinal space charge field associated with the pancake shaped beam. In order to take advantage of RF velocity bunching in the gun, the laser pulse should be stretched to a few ps to sample a few degrees of

the RF wave. In the case studied here, the self-fields of the bunch dominate the longitudinal expansion and the RF wave only makes a small contribution to the final beam phase space distribution. The energy distribution chirp does not vary significantly in the relatively large interval of phases under study.

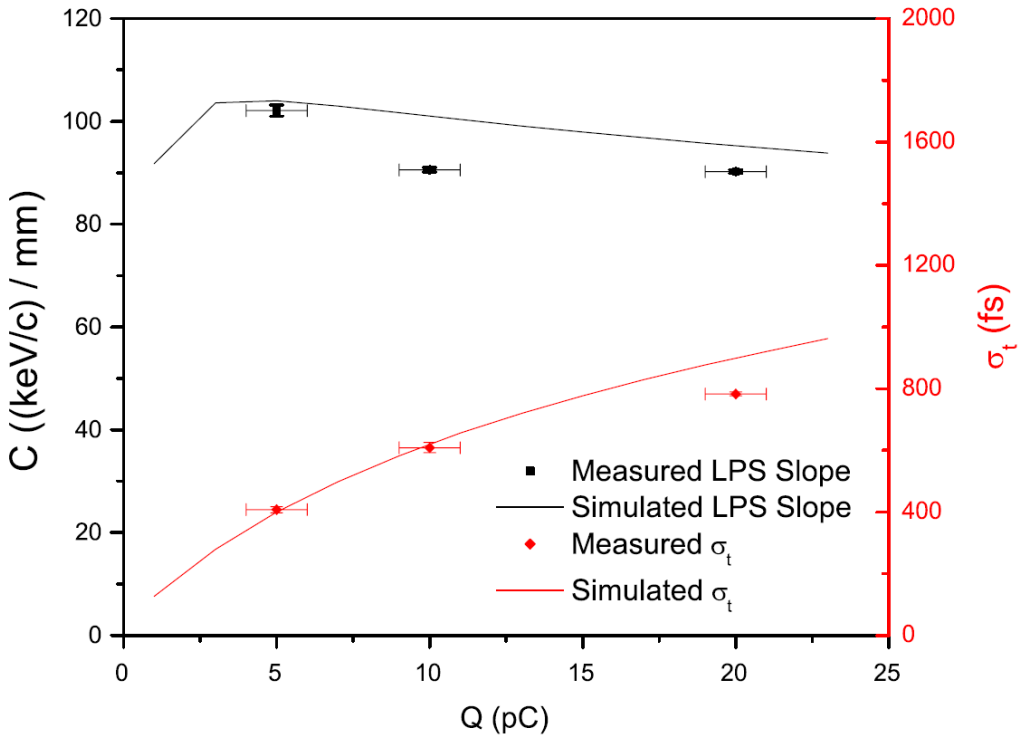


Figure 2.9: LPS Chirp as a function of charge.

More interesting behavior is seen when we vary the input charge as seen in Figure 2.9. We observe, as expected, a significant variation in the RMS bunch length and energy spread. For these measurements the initial laser spot size at the cathode was 500 $\mu$m which explains the slightly shorter bunch lengths.

What may be less expected is the weak dependence of the chirp slope (C) on the beam charge. As the RMS beam parameters increase by a factor of two, the time-energy correlation remains quasi-constant. For a typical beam in the blow-out regime of photoinjector operation, we observe that in the one-dimensional

approximation of the longitudinal expansion, the resulting analytical estimate for C (Equation 2.20) does not depend on the surface charge density at the cathode.

This ceases to be true when the approximation of space charge driven expansion of an initial pancake beam is violated. For example, at the lowest charge point, the bunch lengthening due to the space charge is minimal and other dynamical factors, for example the RF field curvature and transverse dependence, influence the beam evolution.

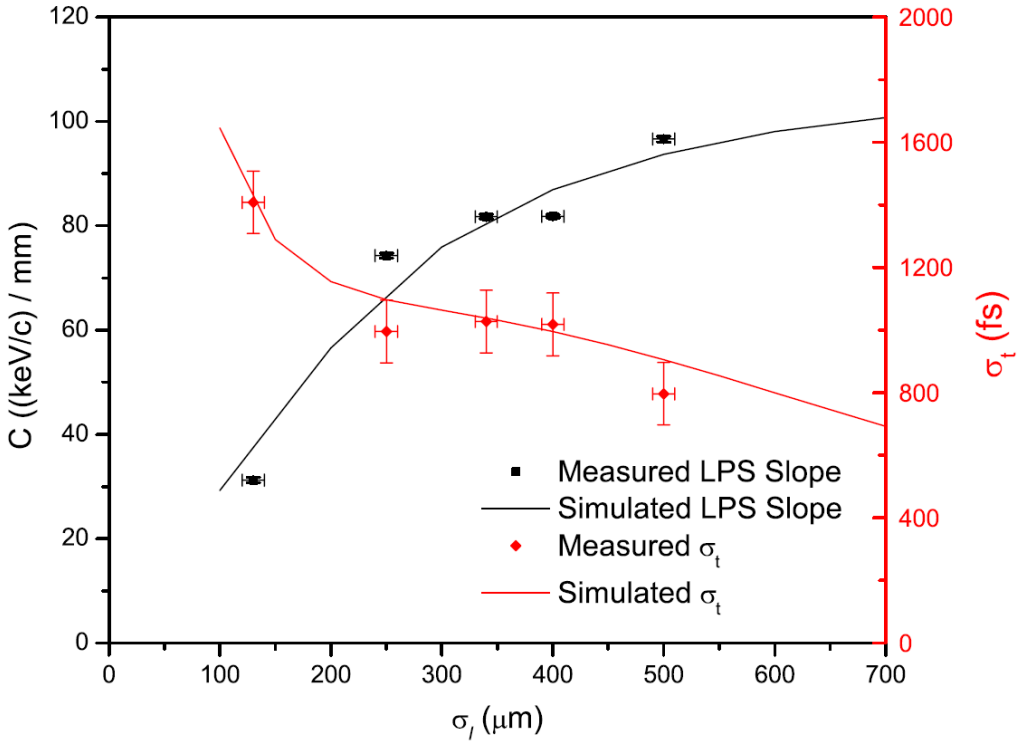


Figure 2.10: LPS Chirp as a function of laser spot on the cathode.

Lastly, we studied the LPS as a function of the laser spot size at the cathode while keeping the charge constant as can be seen in Figure 2.10. Since surface charge density determines the longitudinal expansion, reducing the beam dimensions on the cathode will have a large effect on the expansion dynamics. As the initial spot size on the cathode is decreased, the bunch length increases quickly,

while the slope of the chirp decreases at first weakly then more noticeably for the smaller spot sizes. This can be explained by observing that a smaller chirp is due to a relatively longer beam and smaller energy spread. The longitudinal space charge force decreases more rapidly for smaller laser spot at the cathode due to the fact that the beam (longer and transversely smaller) exits the pancake regime after a shorter propagation distance. In this situation, which by definition is not accounted for in the approximation leading to Equation 2.20), the energy spread growth rate diminishes quickly, leading to a final state with a lower energy chirp.

### 2.2.4 Limits of Photoinjector Blowout Regime Measurement: Phase Space Distortions Due to Asymmetry

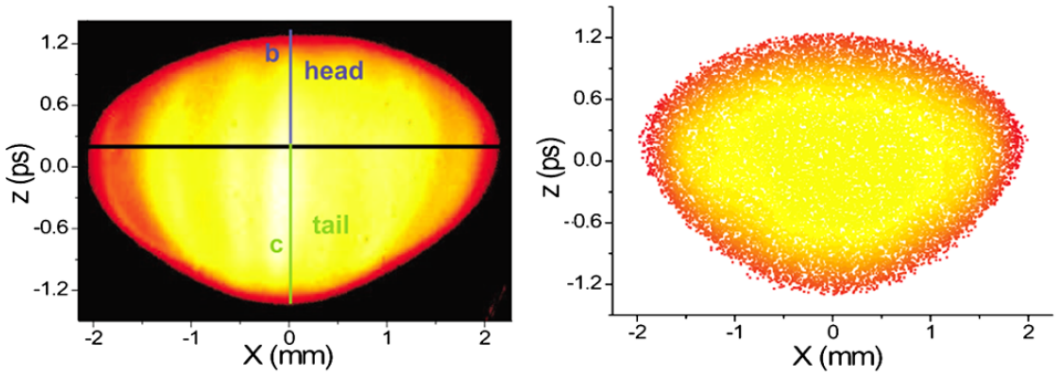


Figure 2.11: X-Z distribution with nonlinear behavior due to image charges at the cathode.(Left) Measured X-Z distribution, semi-axes are labeled b and c. (Right) Simulated X-Z distribution.

The streak image seen left in Figure 2.11 corresponds to a beam of charge of 50 pC, and is taken in the projection (quadrupole-focused) mode. For this measurement, the phase of the deflecting field is such that an upward kick is imparted on the leading edge of the beam, which is thus found at the top of the image. For these charge levels, the beam after expansion is quite a bit longer ($> 600$ fs RMS) and develops an asymmetry in the ellipsoidal boundary showing an elongated tail.

This effect is well predicted by simulations, as seen in the ASTRA phase space displayed on the right side of Figure 2.11. It is due to the deceleration exerted on the beam in the near-cathode region by the beam image charge. This symmetry breaking in the longitudinal space-charge forces is always present, but becomes noticeable only when the magnitude of the image-induced electric field becomes a significant fraction of the RF accelerating field. In the case shown in Figure 2.11, the surface charge is 50 pC for a laser RMS spot size at the cathode, $\sigma_l$, of 400 $\mu$m. Including the image charge contribution, the peak decelerating field at the beams trailing edge is $E_{SC,max} = Q/(2\pi\sigma^2_{L,RMS}) = 5.6$ MV/m which is $> 16$ % of the RF accelerating field at injection phase, $E_0 \sin\phi_0 \sim 34$ MV/m.

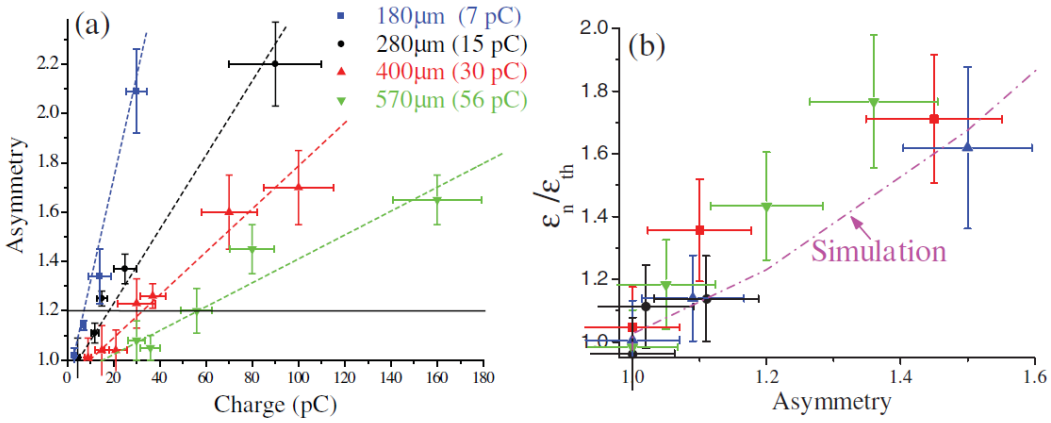


Figure 2.12: Transverse Emittance as a function of x-z asymmetry.

To quantify this effect, we first introduce an asymmetry parameter A defined as the ratio of the semi-axes shown in Figure 2.11 (i.e., $A = b/c$). In Figure 2.12 we show the dependence of A on the charge and laser spot size on the cathode. A linear dependence on charge is found, with a slope increasing as $\sigma^{-2}_{L,RMS}$. The errors mostly come from fluctuations in the beam charge which was up to $\pm$ 12% shot to shot due to both pulse-to-pulse laser energy jitter and pointing jitter on the laser iris aperture. In Figure 2.12(b) the effect of beam asymmetry on the normalized transverse emittance $\epsilon_n$, as measured with a multishot pepper pot

technique, is illustrated. Since the beam emittance has a thermal component th directly proportional to $\sigma_{L,RMS}$, we normalized the measurements to the emittance values th obtained for negligible ($< 1\ pC$) beam charge. There is a strong correlation between A and the amount of emittance growth. When the beam loses its uniformly filled ellipsoid shape, nonlinearities associated with the spacecharge fields quickly degrade the transverse quality of the beam. Values of A $> 1.2$ are to be avoided, which from the data indicate that $E_{SC,max}$ should be limited to less than 10% of the applied field $E_0 \sin \phi_0$.

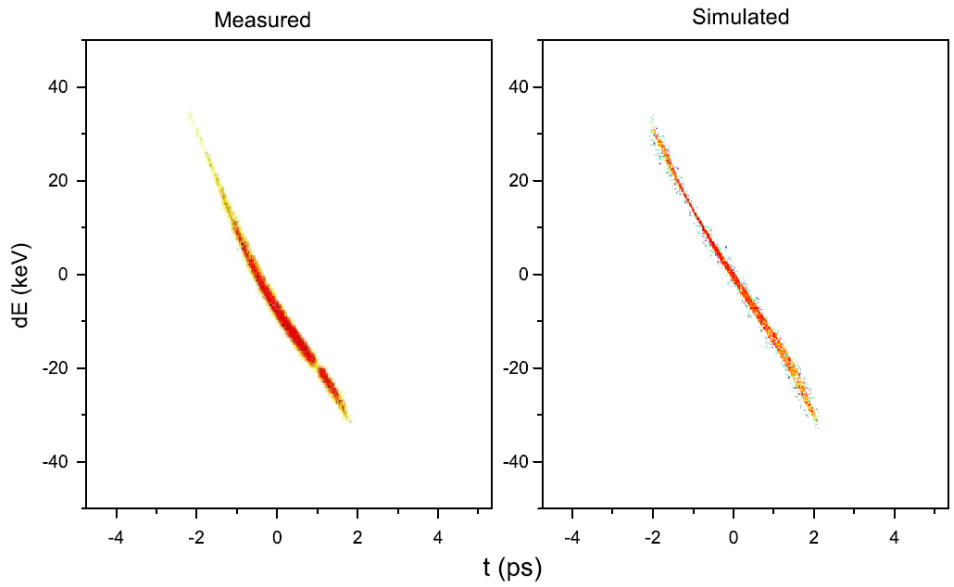


Figure 2.13: Nonlinear LPS due to beam asymmetry.

The effects of this asymmetry on the longitudinal phase space are apparent in the case of a 20 pC beam with an initial RMS laser spot of 100 $\mu$ at the cathode. Figure 2.13 demonstrates the beam quality degradation due to the asymmetry in both the measured and simulated LPS beam distributions. The effect is quite dramatic with the beam distribution losing its nearly ideal linear correlation. Projecting the beam distribution onto the time axis, one finds an asymmetric shape. Such a density profile is the self-consistent cause for the curvature in the self-field dominating the phase space distribution in Figure 2.13. The distortion at

the tail of the beam can be attributed to the retarding effect of the image charge that lowers the energy of the beam tail.

## 2.3 Conclusion

Now that we have examined the current state of high brightness beams to be injected into an advanced accelerators, we move onto the theoretical background of the inverse free electron laser interaction.

# CHAPTER 3

# The Inverse Free Electron Laser Interaction

After the description of the generation of high brightness beams in Chapter 2 we now examine theoretical background of the IFEL interaction. We will start by describing the IFEL fundamental principles, focusing on the concept of a period average resonant interaction. We'll derive and explore the one dimensional equations motion for an electron moving in a planar undulator with the approximation that the laser is a simple plane wave. Then, moving away from the plane wave approximation and toward more realistic models for the laser propagating through the undulator, we'll look at the case where the interaction occurs with a diffraction limited Gaussian laser beam, then at the flattened Gaussian modes which best represent the transverse profile from laser amplifiers operating near saturation. The effects of short pulses are then examined, and found to be important in particular when the laser pulse length is on the order of the amount of slippage that occurs as the electron beam falls behind the laser in the undulator. We then discuss the simulations modes of the interaction in three dimensions and how they apply to the physical experiments under study.

## 3.1 Concept of IFEL Interaction

As discussed in the Introduction, IFEL is an interaction that occurs when a relativistic electron beam co-propagates with a high power laser in vacuum with its trajectory set by a periodic magnetic structure called an undulator. There is a theorem that states to first order there can be no average energy gain induced by a

laser pulse on a relativistic electron beam. It is useful to examine the assumptions of this theorem and how IFEL overcomes them.

The Lawson-Woodward theorem (LWT) [44, 45] states that the energy gain (or loss) of an electron beam from an unbounded interaction with a laser for an infinite extent is zero if there are no static electric or magnetic fields present. The theorem can be better understood by looking at short proof by Esarey et al [46].

A highly relativistic electron with $\beta \to 1$ is propagating along the z direction with the plane wave laser wave vector, $\mathbf{k}$ in an arbitrary direction. For simplicity we will have the laser field be linear polarized in the x-z plane. The change in electron energy over the entire interaction is $\Delta U = \int E_z z \mathrm{d}z$, where the integral is taken from $-\infty$ to $+\infty$. The component of the electric field that is responsible for the acceleration is

$$E_z = \frac{1}{2\pi} \int dk_x dk_z dk_y \hat{E}_z(x,y) e^{i(k_z z - \omega t)} \tag{3.1}$$

and $k_x$ and $k_z$ are the wavenumbers in x and z, and $\hat{E}_z$ is the Fourier transformed electric field. We can plug for vacuum dispersion $\omega = kc$ then apply Gauss's law $\nabla \cdot \mathbf{E} = 0$ using the fields in Fourier transform space we get $\hat{E}_z = -\frac{1}{k_z} k_x \hat{E}_x$ where $\hat{E}_x$ is the transformed transverse electric field. Plugging our results into Equation 3.1 we get,

$$\Delta U = \frac{e}{2\pi} \int \frac{k_x}{k_z} \hat{E}_x(x,y) \mathrm{d}k_x \mathrm{d}k_y \int_{-\infty}^{\infty} \mathrm{d}z e^{i(k_z - k)z} \tag{3.2}$$

Looking at the last integral in Equation 3.2 we see that this is a Dirac delta function, $\delta(k_z - k)$. This means that the integral vanishes unless $k = k_z$ which implies that $k_x$ must be zero and therefore the entire integral vanishes.

In effect LWT shows that you cannot achieve a force that is along the motion of the electron beam and maintain phase matching with it. As a result, the electron

beam slips through all of the phases of the laser field, canceling out whatever forces would have accelerated the beam if the extent is infinite.

There are several schemes which break one of the assumption of the theorem to achieve electron acceleration using laser fields. One possibility is to use nearby structures to obtain phase matching, or limit the interaction region (dielectric or half-plane). Another possibility is to use non linear interactions like beatwave or ponderomotive scattering. IFEL achieves acceleration while still considering the laser as a plane wave in vacuum and the interaction infinite in extent.

The idea behind IFEL is to add a periodic magnetic field to induce transverse motion of the relativistic electron beam. This will enable coupling of the electrons to the transverse electric field of the plane wave, while also controlling the phase seen by the electron beam as it slips with respect to the laser.

The IFEL interaction allows for maximal energy exchange when the period and magnetic field strength of the undulator are chosen to satisfy the resonance condition. This condition occurs when the electron beam slips exactly one laser wavelength per undulator period. Particles away from resonance sample all phases of the laser, resulting in no average energy change.

## 3.2 One Dimensional Case in Planewave Laser Field

The 1-D IFEL equations are covered by Courant et al [18]. We begin with the case of a relativistic electron beam moving in planar undulator and a plane wave laser with its wave number vector parallel to the undulator axis. The equation of motion governing the evolution of an electron in electric and magnetic fields are given by the Lorentz force equation:

$$m\frac{d(\gamma\mathbf{v})}{dt} = e(\mathbf{E}_L + \mathbf{v} \times (\mathbf{B}_u + \mathbf{B}_L)) \tag{3.3}$$

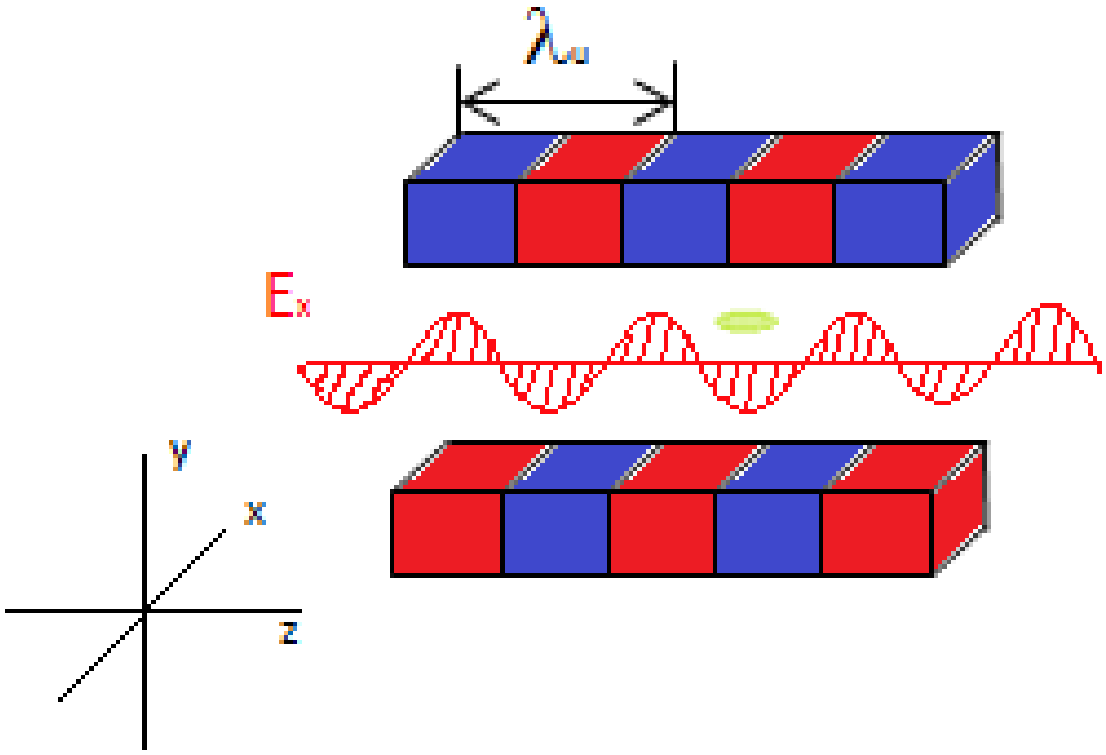


Figure 3.1: Cartoon of concept of IFEL interaction. The relativistic electron beam's slippage with respect to the laser is controlled by the undulator. When the electron beam slips by one radiation wavelength per undulator cycle, resonant energy exchange is obtained.

where $\mathbf{E}_L$ and $\mathbf{B}_L$ are the electric and magnetic fields of the laser and $B_u$ is the magnetic field of the undulator, $\gamma = (1-\beta^2)^{-1}$ is the relativistic Lorentz factor, $\beta = v/c$ is the magnitude of the electron velocity normalized by the speed of light, and e is the electron charge.

If we set up a Cartesian coordinate system such that the direction of the beam propagation is along $z$. We can choose linear polarized plane wave to have the field in $x$, the direction of propagation along $z$ and the magnetic field from undulator in the y direction. A setup of the coordinate system can be seen in Figure 3.1.

The magnetic field of a planar undulator with no transverse dependence can

be described by:

$$\mathbf{B}_u = (0, B_0 \sin(k_u z), 0) \tag{3.4}$$

Where $k_u$ is the undulator wave number or $2\pi/\lambda_u$ and $\lambda_u$ the undulator period. The plane wave laser can be described as:

$$\mathbf{E}_L = (E_0 \sin(kz - \omega t), 0, 0) \tag{3.5}$$

The corresponding magnetic field due to the laser, $\mathbf{B}_L = \mathbf{E}_L/c$. To provide us insight about the symmetries of this system we can write down the Lagrangian [8]:

$$\mathscr{L} = \frac{-mc^2}{\gamma} + e\mathbf{v} \cdot (\mathbf{A}_L + \mathbf{A}_u) \tag{3.6}$$

Where $\mathbf{A}_L = -E_0/(kc)cos(kz - \omega t)\hat{\mathbf{x}}$ and $\mathbf{A}_u = -B_0/k_u cos(k_u z)\hat{\mathbf{x}}$ are the vector potentials for the laser and undulator, respectively. As there is no transverse dependence to any of the forces involved, the Lagrangian is invariant under translations of the transverse coordinates and therefore their conjugate momenta is a conserved quantity [47]. The transverse canonical momentum by taking the derivative of the Lagrangian with respect to the transverse coordinates, i.e. $\mathbf{p}_T = \partial\mathscr{L}/\partial\dot{\mathbf{x}}_T$. This yields

$$\mathbf{p}_T = \gamma m \mathbf{v}_T + e(\mathbf{A}_L + \mathbf{A}_u) = C \tag{3.7}$$

The constant, $C$ is the initial transverse momentum of the beam outside of the undulator. For an electron entering the undulator on axis with zero angle, this constant is zero. If we assume a small angle between the two (paraxial approximation) and a relativistic beam, then $p_{T0} = \gamma\beta\theta$, where $\theta$ is the angle. We can write the longitudinal component of the electron velocity in the undulator as

$$\beta_z = \sqrt{1 - \frac{1}{\gamma^2} - \beta_T^2} \tag{3.8}$$

Now we solve for $\beta_T$ in terms of the explicit forms vector potentials from Equation 3.7. Assuming co-propagation of the laser and electron beams,

$$\beta_T = \frac{eB_0}{\gamma mck_u} cos(k_u z) + \frac{eE_0}{\gamma mc^2 k} cos(kz - \omega t) \tag{3.9}$$

We can solve for $\beta_z$ using our result for $\beta_T$ by plugging into Equation 3.8. We can simplify the result with the following scale (unit-less) parameters, $K = eB_0/mck_u$ and $K_L = eE_0/mc^2k$ resulting in

$$\beta_z = \sqrt{1 - \frac{1 + K^2 cos^2(k_u z) + K_L^2 cos^2(kz - \omega t) + 2K_L K cos(k_u) cos(kz - \omega t)}{\gamma^2})} \tag{3.10}$$

We can now make use of the half angle trigonometric identities: $cos^2(\alpha) = 1/2 + 1/2cos(2\alpha)$ and $cos(\alpha)cos(\beta) = 1/2cos(\alpha + \beta) + 1/2cos(\alpha - \beta)$ and assume that the beam is relativistic ($\gamma >> 1$), therefore we can expand $\beta_z$ to first order safely, giving us

$$\beta_z \simeq 1 - \frac{2 + K^2 + K_L^2 + 2K_L K(cos(\psi_+) + cos(\psi_-)) + K^2 cos(2k_u z) + K_L^2 cos(2(kz - \omega t))}{4\gamma^2} \tag{3.11}$$

Here we define $\psi_+ = (k + k_u)z - \omega t$ and $\psi_- = (k - k_u)z - \omega t$ for the combined cross terms seen in Equation 3.10. Since the laser wavelength is typically several orders of magnitude below that of the undulator, $K_L << K$ and we can neglect most of the terms involving $K_L$.

The work-energy theorem for a charged particle in an electric fields tells us:

$$\frac{dU}{dt} = e\mathbf{E} \cdot \mathbf{v} \tag{3.12}$$

Since **E** only has an x component from 3.9 for $\beta_x$, the explicit form of the electric field, the relativistic energy we get

$$\frac{d\gamma}{dz} = \frac{kK_L}{\gamma}\sin(kz - \omega t)(Kcos(k_u z) + K_L cos(kz - \omega t)) \tag{3.13}$$

Here we change the independent variable $d/dt \sim cd/dz$ instead of $c\beta_z d/dz$ as we are interested in the slow behavior (on the order of $\Delta z \sim \lambda_u$) of the energy evolution along the undulator. Again we can use trigonometric identities to write,

$$\frac{d\gamma}{dz} = \frac{kK_L K}{2\gamma}(\sin(\psi_+) + \sin(\psi_-)) \tag{3.14}$$

The energy evolution is proportional to $\sin(\psi_+)$ and $\sin(\psi_-)$. We can write these functions explicitly by examining the time evolution,

$$ct = ct_0 + z + \int_0^z dz \frac{2 + K^2 + 2K_L K(\cos(\psi_+) + \cos(\psi_-))}{4\gamma^2} + \frac{K^2}{8\gamma^2 k_u}\sin(2k_u z) - \phi_0 \tag{3.15}$$

Here the final term can be integrated so long as the $K$ and $k_u$ do not vary too violently over an undulator period.

Plugging into the phase we can now write the phases

$$\psi_\pm = \pm k_u z - k\int_0^z dz \frac{2 + K^2 + 2K_L K(cos(\psi_+) + cos(\psi_-))}{4\gamma^2} - \frac{kK^2}{8\gamma^2 k_u}\sin(2k_u z) - \phi_0 \tag{3.16}$$

There is a way to elegantly combine these terms using the following expansion of Bessel's functions:

$$\sin(a + b\sin\phi) = \sum_{n=-\infty}^{\infty} J_n(b)\sin(a + n\phi) \tag{3.17}$$

We can use this to write each term:

$$\sin(\psi_{\pm}) = \sum_{n=-\infty}^{\infty} (-1)^n J_n(G) \sin[(2n \pm 1)k_u z - \int_0^z dz \frac{2 + K^2 + 2K_L K(cos(\psi_+) + cos(\psi_-))}{4\gamma^2} - \phi_0] \tag{3.18}$$

Here $G = kK^2/8\gamma^2 k_u$. When we sum the two together we can use the dummy indices, $n$ for $\sin(\psi_+)$and $m$ for $\sin(\psi_-)$. If we can collect terms with equal phase, we can collect terms with equal phase when $m = n+1$. The result after collecting terms and exploiting the parity of the Bessel functions,

$$\sin(\psi_+) + \sin(\psi_-) = \sum_{n=-\infty}^{\infty} \Big(J_n(G) - J_{n+1}(G)\Big) \sin\Big[(2n+1)k_u z - k\int_0^z dz \frac{2 + K^2 + 2K_L K(cos(\psi_+) + cos(\psi_-))}{4\gamma^2} - \phi_0\Big] \tag{3.19}$$

If we look at the terms in which $n \neq 0$, we see the harmonic interactions. The strongest interaction is the one in which we select the $n = 0$ term. In this case we define $JJ = J_0(G) - J_1(G)$ and the energy evolution is

$$\frac{d\gamma}{dz} = \frac{kKK_L}{2\gamma} JJ \sin(\psi) \tag{3.20}$$

The ponderomotive phase term $\psi$ in this equation is the coordinate of interest in our one dimensional equations of motion. Taking a spatial derivative on this phase gives us

$$\frac{d\psi}{dz} = k + k_u - \frac{k}{\beta_z} \tag{3.21}$$

By continuing to use the relativistic approximation for $\beta_z$ we can then write the phase evolution as

$$\frac{d\psi}{dz} = k_u - k\frac{2 + K^2 + 2K_L K(cos(\psi_+) + cos(\psi_-))}{4\gamma^2} \tag{3.22}$$

The second harmonic undulator term goes to zero when averaged over a period. With the phase evolution determined in terms of laser and undulator parameters we turn our attention to the energy evolution along the undulator.

This equation, along with the phase evolution shown in Equation 3.22 form the two 1-D equations of motion. Most of the physics of the system are apparent if we neglect terms with $K_L$ in the phase evolution giving us,

$$\frac{d\psi}{dz} = k_u - k\frac{1 + \frac{K}{2}^2}{2\gamma^2} \tag{3.23}$$

Upon examination of equation 3.23 we can set the left hand side to zero, meaning that the ponderomotive phase is now a constant of the motion. For a given set of undulator and radiation parameters, there exists an electron beam energy, $\gamma$, that satisfies this condition. We name this the resonant energy, designated as $\gamma_r$. The resonant condition can be written as

$$\gamma_r^2 = \frac{k(1 + \frac{K^2}{2})}{2k_u} \tag{3.24}$$

which can physically be interpreted as the relationship between the undulator period and strength, and the laser wavelength that result in an electron beam slipping one radiation wavelength per undulator period. With the approximations we have applied, no $K_L$ terms appear in this equation, meaning that the resonance does **not** depend on the laser intensity.

If we choose to inject our electron beam far away from this resonant energy, we will get very little energy transfer from the laser to the electrons as the beam will sample all phases quickly over a period and have little energy modulation. Most cases of interest will involve injection at or near the resonant energy. In light of

this we can expand our energy variable about the resonant energy: $\gamma = \gamma_r + \delta\gamma$ where $\delta\gamma/\gamma_r \ll 1$. Our dynamical equations then become

$$\frac{d(\delta\gamma)}{dz} \simeq \frac{kK_LKJJ}{2\gamma_r}\big(\sin(\psi) - \sin(\psi_r)\big) \tag{3.25}$$

$$\frac{d\psi}{dz} \simeq 2k_u\frac{\delta\gamma}{\gamma_r} \tag{3.26}$$

Here $\psi_r$ is the resonant phase, whose explicit value is related to the energy change of the resonant particle. These equations resemble those of a physical pendulum.

Equations 3.25 and 3.26 are Hamilton's equations of motion for this Hamiltonian:

$$H = \frac{k_u\delta\gamma^2}{\gamma_r} - \frac{kK_LKJJ}{2\gamma_r}\big(cos(\psi) + \psi\sin(\psi_r)\big) \tag{3.27}$$

Using this Hamiltonian we can investigate our first case of interest, in which we allow the resonant phase to be zero and the potential involved then is proportional to $cos(\psi)$. We can then map out the interactions by looking at the curves of constant Hamiltonian as seen in Figure 3.2. We can see ellipses that represent closed orbits of particles that are injected close to the stationary phase space point at $(0, 0)$. The cusp-like boundary is known as the separatrix and separates trapped particles from passing particles. All of the particles within the separatrix remain local to the stationary design point, while anything outside of the bucket passes through phase space.

The region inside the separatrix is commonly known as a "bucket". Its height from the stationary point can be derived using the Hamiltonian and is equal to

$$\frac{\delta\gamma_{bucket}}{\gamma_r} = \frac{1}{\sqrt{1 + \frac{K^2}{2}}}\sqrt{2KK_LJJ} \tag{3.28}$$

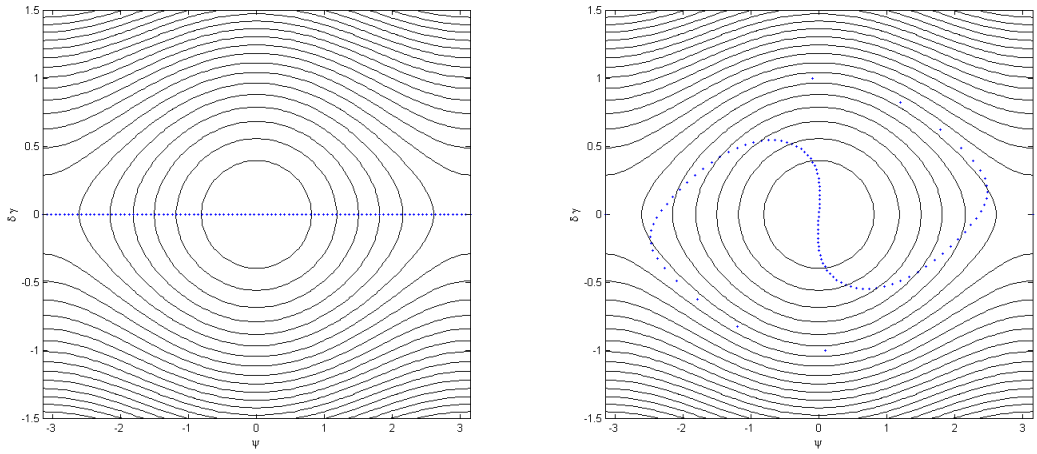


Figure 3.2: Phase Space Plot with trajectories and particles. (Left) Phase space at injection. (Right) Phase space at injection for a buncher.

All of the particles that are trapped within the bucket will undergo synchrotron oscillations. If the particle is injected near the stationary point at the center of the bucket the oscillation period will be well defined as

$$Z = \frac{\lambda_u \sqrt{1 + \frac{K^2}{2}}}{\sqrt{2K_L K J J}} \tag{3.29}$$

For cases of interest the electron beam will be much longer than the wavelength of the laser radiation, and thus we will fill all phases within some energy spread of the resonant energy. The particles orbits will evolve along the phase space trajectories shown as the lines in Figure 3.2.

We can stop the interaction after that the electrons undergo a quarter period synchrotron oscillation if we choose an appropriate length for the undulator. The electrons will then be clustered around the stationary point in phase space with an increased energy spread. This results in an electron beam density modulated at the radiation wavelength in a process called bunching.

## 3.3 Tapering and Acceleration

For a fixed set of undulator parameters $(K, k_u)$ and radiation wavenumber $k$ any electron beam injected into this interaction will simply rotate in phase space around the stationary point. In order to achieve energy gain we must allow the parameters to evolve over the length of the undulator in a way that maintains the resonant condition for the accelerating particles. Taking the derivative with respect to z on Equation 3.24 we get

$$\frac{\mathrm{d}}{\mathrm{d}z}(\gamma_r^2)_{Taper} = \frac{k(1+\frac{K^2}{2})}{2k_u}\Big[2K\frac{\mathrm{d}K}{\mathrm{d}z} - \frac{1}{k_u}\frac{\mathrm{d}k_u}{\mathrm{d}z}\Big] \tag{3.30}$$

This equation describes the tapering required for a chosen energy gain along the undulator. Note that this does not depend on $K_L$, and therefore the laser field intensity. Plugging the resonant energy and phase into Equation 3.20, multiplying through with $\gamma_r$ and pulling the derivative to the outside, we get

$$\frac{\mathrm{d}}{\mathrm{d}z}(\gamma_r^2)_{Ponderomotive} = kKK_LJJ\sin(\psi_r) \tag{3.31}$$

Here we have something that explicitly depends on the laser field intensity as it contains $K_L$. If we match the tapering and ponderomotive gradients we can achieve an optimal accelerating gradient.

When designing the undulator tapering profile we must still choose a resonant phase, $\psi_r$. This parameter sets the ponderomotive gradient for the localized stationary point in phase space. If it is set to be $\pi/2$ then there will be a maximum energy gain but the bucket's extent in phase space will be limited to a single point and therefore there will be no acceleration of a realistic beam. If we choose the resonant phase to be zero then we return once more to the case of the buncher. For most cases this parameter is chosen as a compromise of $\pi/4$.

## 3.4 Gaussian laser propagation

Thus far we have treated the ideal case for the interaction when the laser propagation or $K_L$ is a constant over the length of the undulator. In an effort to accurately model the interaction we allow the laser field to become a function of z and have a finite transverse extent. A simple model including these effects is to assume a Gaussian mode for laser pulse,

$$\mathbf{E_L} = E_0 e^{-\left(\frac{x^2+y^2}{w_0^2}\right)} \frac{w_0}{w(z)} \sin\left(kz - \omega t - \phi_G - k\frac{r^2}{2R(z)}\right)\hat{\mathbf{x}} \tag{3.32}$$

This mode, the $\mathrm{TEM}_{00}$, is characterized by $w$ the waist parameter, $R(z)$ the radius of curvature of the phase fronts, and $\phi_G$ is the Guoy phase shift that results from going through a waist.

The waist parameter w is equal to $\sqrt{2}\sigma_r$, where $\sigma_r$ is the second moment of the time-averaged Gaussian intensity distribution. The waist parameter will vary along the laser propagation according to $w(z) = w_0\sqrt{1 + (z/z_r)^2}$ where $z_r = \pi w_0^2/\lambda$ is the Rayleigh length. The radius of curvature of the phase fronts are $R(z) = z\big[1 + (z_r/z)^2\big]$ The radius of curvature is infinity when the Gaussian laser beam is at the waist. The Guoy phase shift is a result of transverse spatial confinement of the wave and is specified by $\phi_G = \arctan(z/z_r)]$. These three effects modify the radiation field from a simple harmonic plane wave function by lowering its value away from the waist, shifting the phase off axis away from the waist, and finally changing the phase due to crossing the waist.

Once the effects of diffraction are included the ponderomotive gradient can be computed, set equal to the tapering gradient and the accelerator designed. The tapering will be weaker in at the ends of the undulator as the ponderomotive gradient will have decreased due to the spot size increasing. Because IFEL has phase dependence on the laser, it is important to rephase the electron beam as it passes through the waist.

Ideally the ponderomotive gradient and tapering gradients will be equal to each other but in the context of an experiment in which laser intensity, transverse mode and pointing substantially fluctuates the ponderomotive gradient can fall below or above a given undulator tapering design along the undulator.

For the case of the ponderomotive gradient becomes less than the tapering gradient during propagation, there is a lack of available field intensity to accelerate the electrons and their energy gain on the curve set by the tapering gradient. This causes the electrons to fall out of ponderomotive bucket, away from resonance, and their average energy gain by the fundamental IFEL interaction will go to zero.

### 3.4.1 Flattened Gaussian

An more accurate model for a laser from a modern amplifier are Flattened Gaussian (FB) modes. They result from gain saturation in the transverse profile of the beam as it propagates through the amplifier. These modes are comprised of higher order Laguerre-Gaussian (LG) modes [48]. These modes are

$$E = E_0 \sum_{n=0}^{N} c_n^{(N)} L_n\Big(\frac{(2N+1)r^2}{w_0^2}\Big) \exp\Big[-\frac{(N+1)r^2}{w_0^2}\Big] \tag{3.33}$$

where $L_n$ is the $n$th Laguerre polynomial and the $c_n^{(N)}$ are coefficients defined by:

$$c_n^{(N)} = (-1)^n \sum_{m=n}^{N} \frac{1}{2^m} \begin{pmatrix} m \\ n \end{pmatrix} \tag{3.34}$$

The higher order modes have a faster Guoy phase shift through the waist and even lower on axis field near the waist as can be seen in Figure 3.3. This figure compares the radial profiles of zero-order Gaussian and second and fourth order FB modes at three points they propagate from a 6.5 m focal length lens to a waist.

The on axis fluence for the higher order modes show nearly a factor of 2

decrease while propagating near the waist compared to that of a $TEM_{00}$ Gaussian mode. This decrease in field intensity can cause an IFEL accelerator's that was optimally designed for Gaussian laser profiles to have the ponderomotive gradient to drop below the tapering gradient throughout the undulator resulting in either fail to capture at the beginning of the undulator or the captured electron beam to fall out of the ponderomotive bucket prematurely.

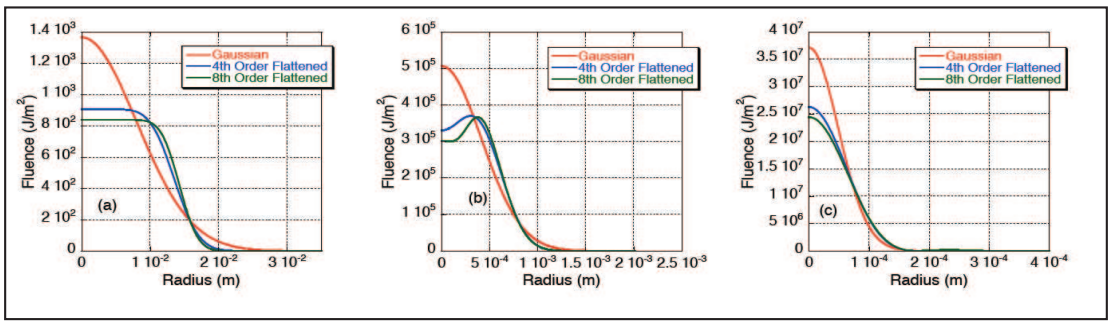


Figure 3.3: Radial Profiles of Flattened Gaussian Modes. a) far from waist b) .5 m from waist c) at waist.

## 3.5 IFEL Interaction in the Limit of Short Laser Pulse

A concern of use of short pulse lasers for this interaction is when the pulse length of the laser is on the same scale as the slippage of electron beam with respect to the laser. Under these conditions, $K_L(z)$ becomes further reduced at the ends of the undulator in addition to the reduction due to the Gaussian mode propagation. The laser pulse length gives limited duration to the interaction, as the electron beam will slip completely outside of the laser envelope, cutting off the interaction completely. To avoid this in longer undulator designs, the laser pulse length should be greater than the slippage in the undulator, or $c\Delta t > \lambda N_u$ where $L_u$ is the length of the undulator.

When it is on the same scale we can modify our existing equations and examine the effect of the slippage. The electric field from Equation 3.32, which we will call

$\mathbf{E_1}$ now becomes:

$$\mathbf{E_L} = \mathbf{E_1} \exp\Big[ - \frac{(kz - \omega t)^2}{(\omega\tau)^2} \Big] \tag{3.35}$$

This electric field form is a solution to the slowly varying envelope approximation (SVEA) to Maxwell's equations where there is a Gaussian profile with second moment $\tau$ with the fast phase term contained in Equation 3.32.

As the IFEL acceleration process occurs, the electron beam slips a wavelength per period in the undulator

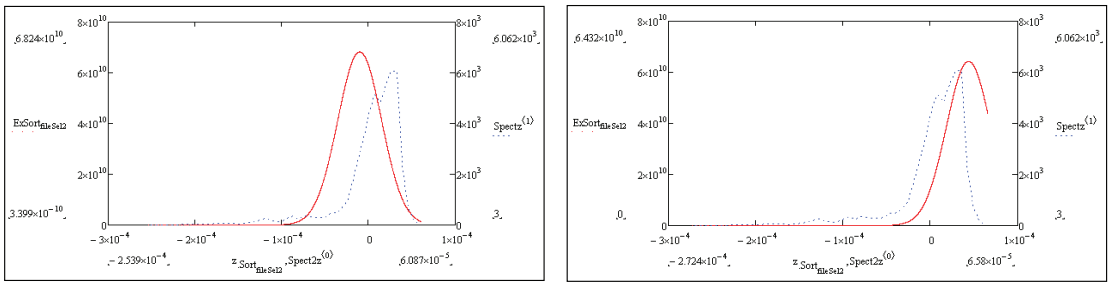

Figure 3.4: Demonstration of slippage of the electron beam at beginning and end of undulator. Electron beam (blue) and laser (red) longitudinal profiles at the beginning (left) and end (right) of the undulator

## 3.6 Three dimensional simulations of IFEL interaction

To make the most realistic possible model of the interaction we must look at the full three dimensional evolution of the electron beam in a laser field.

To simulate the interaction using particle tracker simulations, a magnetostatic field map was used to represent the field of the undulator. The laser is represented by the time dependent field in Equation 3.35.

The particles' trajectories are then integrated the fields then pushing the particles at each timestep. The first 3D beam studies were performed by cbeam,

a particle tracing code developed at LLNL, then compared and verified by the commercial code, general particle tracer.

Now that we have established the theoretical groundwork for the IFEL interactions we can look at specific experimental cases that use this interaction to manipulate ultrashort electron beams. Particularly using the a laser in the THz regime to do synchronization and compression and high gradient acceleration using TW power laser pulses.

# CHAPTER 4

# Synchronization and Compression using THz IFEL Interaction

With an understanding of the IFEL interaction we are now in position to examine the application of ultrashort electron beam compression and synchronization using the IFEL interaction with a THz laser field.

Although high power sources of optical scale radiation are readily available, the wavelength and thus the length scale of the modulation of the electron beam density is typically several orders of magnitude smaller than the bunch length of high brightness beams created by photoinjectors. If we wish to compress a single bunch of electrons using an IFEL interaction, we should choose a wavelength that is initially on the same scale as the beam to manipulate the beam. This could be used for electron diffraction or to control injection (maximize capture and minimize energy spread) into a high gradient short wavelength accelerator.

A THz driven IFEL has the advantage of a high gradient interaction over a short length that can be used to compress and synchronize an electron beam produced by a photoinjector to a laser if the THz is produced by that laser.

The THz regime is the region of the electromagnetic spectrum extending from 0.1 to 10 THz in frequency with a corresponding wavelength band of 3 mm to 30 $\mu$m. This band falls between the optical infrared and microwave regions of the electromagnetic spectrum as can be seen in Figure 4.1

This band is colloquially known as the THz gap because of technological gap

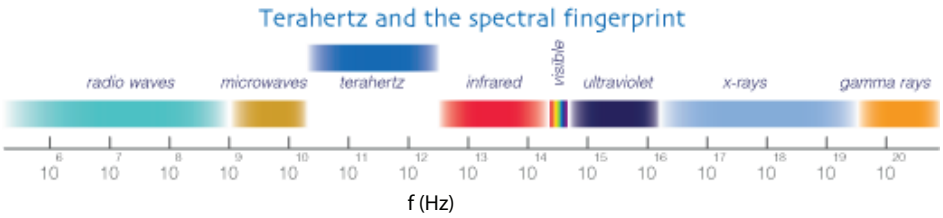


Figure 4.1: Electromagnetic Spectrum showing the THz Gap.

left by the lack of efficient high power THz sources, in spite of there being a high demand for such sources. Due to many molecular transitions in this regime there are a large range of applications for THz radiation from medical imaging, to security to cultural heritage verifications [49–51].

With so much demand for THz sources, their development of THz remains an ongoing area of active research. There are several avenues the development of THz sources. They include quantum cascade lasers [52] radiation from relativistic electron beam sources such as CTR, CSR and THz FELs, and optical conversion processes such as rectification of ultrashort laser pulses.

Our application demands a relatively high peak power of THz radiation that is synchronized to the laser. As we plan on interacting the electron beam with THz radiation and the currently available resources are limited to a single beamline we chose to generate the THz through optical rectification of an ultrashort laser pulse.

## 4.1 Optical Rectification Model

### 4.1.1 Nonlinear three wave mixing

Optical rectification can be seen a three wave difference mixing process where two of the waves to be mixed are subcomponents of a wide bandwidth continuous spectrum. We can begin our examination by following the example in Yariv [53]

by looking at the three wave mixing process for two waves that are closely spaced in frequency space. We begin with Maxwell's equations in a non-magnetic medium with polarization, $\mathbf{P}$ stated explicitly:

$$\begin{aligned} \nabla\times\mathbf{H} &= \mathbf{J} + \frac{\partial}{\partial t}(\epsilon_0\mathbf{E}+\mathbf{P}) \\ \nabla\times\mathbf{E} &= -\frac{\partial}{\partial t}(\mu_0\mathbf{H}) \end{aligned} \tag{4.1}$$

Here we can break the polarization into the linear and nonlinear parts, $\mathbf{P} = \epsilon_0\chi_L\mathbf{E} + \mathbf{P}_{NL}$. Here $\chi_L$ is the linear susceptibility and $\mathbf{P}_{NL}$ is the nonlinear polarization. The nonlinear polarization to second order is defined by $(P_{NL})_i = 2d_{ijk}E_jE_k$ where $d_{ijk}$ is the effective second order susceptibility. We can simplify the curl of $\mathbf{h}$ in Equation 4.1 by introducing the conductivity through Ohm's law, $\mathbf{J} = \sigma\mathbf{E}$, also we can substitute $\epsilon = \epsilon_0(1+\chi_L)$ .

Taking the curl on the curl of $\mathbf{E}$ and recognize that $\nabla\cdot\mathbf{E} = 0$ by Gauss's law with no free charges. We get a wave equation for $\mathbf{E}$,

$$\nabla^2\mathbf{E} = \mu_0\sigma\frac{\partial\mathbf{E}}{\partial t} + \mu_0\epsilon\frac{\partial^2\mathbf{E}}{\partial t^2} + \mu_0\frac{\partial^2}{\partial t^2}\mathbf{P}_{NL} \tag{4.2}$$

Since we are examining three wave mixing, we can assume three Fourier modes and simplify the problem by assuming plane waves with complex notation,

$$\begin{aligned} \mathbf{E}^{(\omega_1)}(z,t) &= \mathbf{E}_1 e^{\mathrm{i}(\omega_1 t - k_1 z)} \\ \mathbf{E}^{(\omega_2)}(z,t) &= \mathbf{E}_2 e^{\mathrm{i}(\omega_2 t - k_2 z)} \\ \mathbf{E}^{(\omega_3)}(z,t) &= \mathbf{E}_3 e^{\mathrm{i}(\omega_3 t - k_3 z)} \end{aligned} \tag{4.3}$$

Here we are explicitly stating the real part using complex notation for the three plane waves. $E_{m,n}(z)$ are indexed such that $m$ is the selected mode corresponding to $\omega_m$ and $n$ is the vector component.

We can now write the solution to Equation 4.2 in terms of our first mode. For the spatial part we can employ the slowly varying wave approximation, $(d\mathbf{E}_1/dz)k_1 \gg d^2\mathbf{E}_1/dz^2$ which allows us to state

$$\nabla^2(\mathbf{E}_1) = -\frac{1}{2}\big[k_1^2\mathbf{E}_1 + 2\mathrm{i}k_1\frac{\mathrm{d}\mathbf{E}_1}{\mathrm{d}z}\big]e^{\mathrm{i}(\omega_1 t - k_1 z)} \tag{4.4}$$

For the right hand side of the wave equation we get,

$$\text{rhs} = (-\mathrm{i}\omega_1\mu_0\sigma + \omega_1^2\mu_0\epsilon)\frac{\mathbf{E}_1}{2}e^{\mathrm{i}(\omega_1 t - k_1 z)} - \mu_0\omega_1^2\big[\mathbf{P}_{NL}^{(\omega_1)}(z,t)\big] \tag{4.5}$$

Recognizing that $\omega_1^2\mu_0\epsilon = k_1^2$, we cancel these terms on both sides of the wave equation. We then can cancel the time dependent phase terms because we choose the difference frequency, $\omega_1 = \omega_2 - \omega_3$. Finally, we divide by $\mathrm{i}k\exp(-ikz)$ on both sides and we get

$$\frac{\mathrm{d}\mathbf{E}_1}{\mathrm{d}z} = -\frac{c\sigma\mu_0}{2n(\omega_1)}\mathbf{E}_1 - \frac{\mathrm{i}\mu_0 c\omega_1}{2n(\omega_1)}e^{\mathrm{i}\Delta kz}\mathbf{P}_{NL} \tag{4.6}$$

This equation describes the amplitude evolution of the THz as it passes through a nonlinear material with an index of refraction that has frequency dependence, $n(\omega)$. We can further simply the expression by recognizing that the first term acts as a damping term. We introduce $\alpha$, a damping parameter. Moreover, $\Delta k = k_1 - k_2 - k_3$ which we can apply material dispersion to make $\Delta k = 1/c\big[n(\omega_1)\omega_1 - n(\omega 2)\omega_2 - n(\omega_3)\omega_3\big]$.

### 4.1.2 Bandwidth continuum mixing and THz generation

So far we have been looking at discrete 3 waves, but optical rectification is difference frequency mixing across a continuous bandwidth. As such, we will change notation and introduce the continuous frequency variable $\omega$ within the bandwidth

of laser and the THz frequency variable $\Omega$ The nonlinear polarization then becomes

$$P_{NL}(\Omega)_i = d_{ijk} \int_0^\infty E_j(\omega + \Omega) E_k(\omega)^* \mathrm{d}\omega \tag{4.7}$$

With our simplifications and change of notation the THz amplitude field evolution equation becomes

$$\frac{\mathrm{d}\mathbf{E}_1(\Omega, z)}{\mathrm{d}z} = -\frac{\alpha(\Omega)}{2}\mathbf{E}_1(\Omega, z) - \frac{\mathrm{i}\mu_0 c\Omega}{2n(\Omega)} e^{\mathrm{i}\Delta kz}[\mathbf{P}_{NL}] \tag{4.8}$$

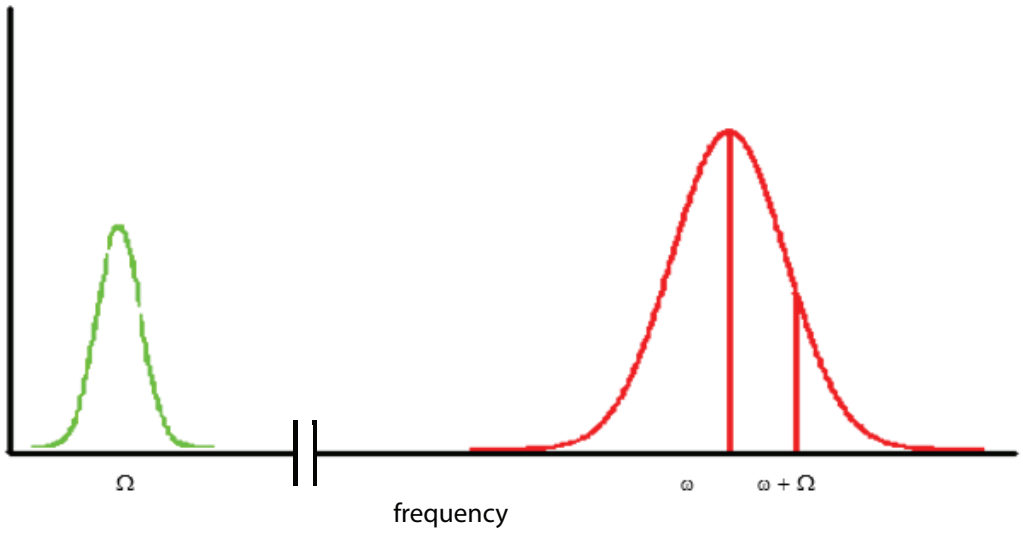


Figure 4.2: Cartoon of difference mixing within bandwidth of the spectrum of the laser.

With the continuum bandwidth our $\Delta k$ term also changes. We can expand the function $\Delta k(\Omega) = k(\Omega) - k(\omega) - k(\omega + \Omega) \sim k(\Omega) + \partial k/\partial\omega\, \Omega \sim \Omega/c\big(n(\Omega) - n_g(\omega_0)\big)$

Looking at Equation 4.8, we see that there are three terms of interest that we can control in the generation of THz radiation by optical rectification. First is

the strength of $P_{NL}$, which is controlled by the second order coefficient, $d_{ijk}$. The second term of interest is the absorption term containing $\alpha(\Omega)$ and the third is a multiplicative phase matching factor, $\exp[i\Delta kz]$. These three factors, and thus the efficiency of the optical rectification process, are dependent upon the choice of nonlinear material. A chart of nonlinear materials, compiled by Hebling [54] can be seen in Table 4.1. The effective nonlinear coefficient can be seen in the second column of this chart.

| Nonlinear Materials | | | | | |
|---|---|---|---|---|---|
| Material | $d_{eff}$ (pm/V) | $n^{gr}_{800nm}$ | $n_{THz}$ | $\alpha(cm^{-1})$ | FOM ($pm^2cm^2/V^2$) |
| CdTe | 81.8 | – | 3.24 | 4.8 | 11.0 |
| GaAs | 65.6 | 4.18 | 3.59 | 0.5 | 4.21 |
| GaP | 24.8 | 3.67 | 3.34 | 0.2 | 0.72 |
| ZnTe | 68.5 | 3.13 | 3.17 | 1.3 | 7.27 |
| GaSe | 28.0 | 3.13 | 3.27 | 0.5 | 1.18 |
| $sLiNbO_3$ | 168 | 2.25 | 4.96 | 17 | 18.2 |
| sLN 100K | ” | ” | ” | 4.8 | 48.6 |
| DAST | 615 | 3.39 | 2.58 | 50 | 41.5 |

Table 4.1: Chart of Nonlinear Materials from

We selected stoichiometric magnesium oxide doped lithium niobate ($MgO : LiNbO_3$). The 0.67 % MgO doping allows for a reduction of photorefractive damage as the high intensity short laser pulse travels through the crystal. Although DAST, an organic molecule has the highest nonlinear coefficient, it also has a very large absorption coefficient. Stochiometric lithium niobate (sLN) was chosen because when it is cooled to 100 K, has the highest figure of merit (FOM), a measure defined by

$$\mathrm{FOM} = \frac{4\mathrm{d}_{\mathrm{eff}}^2}{\alpha^2 \mathrm{n}_{800\mathrm{nm}}^2 \mathrm{n}_{\mathrm{THz}}^2} \tag{4.9}$$

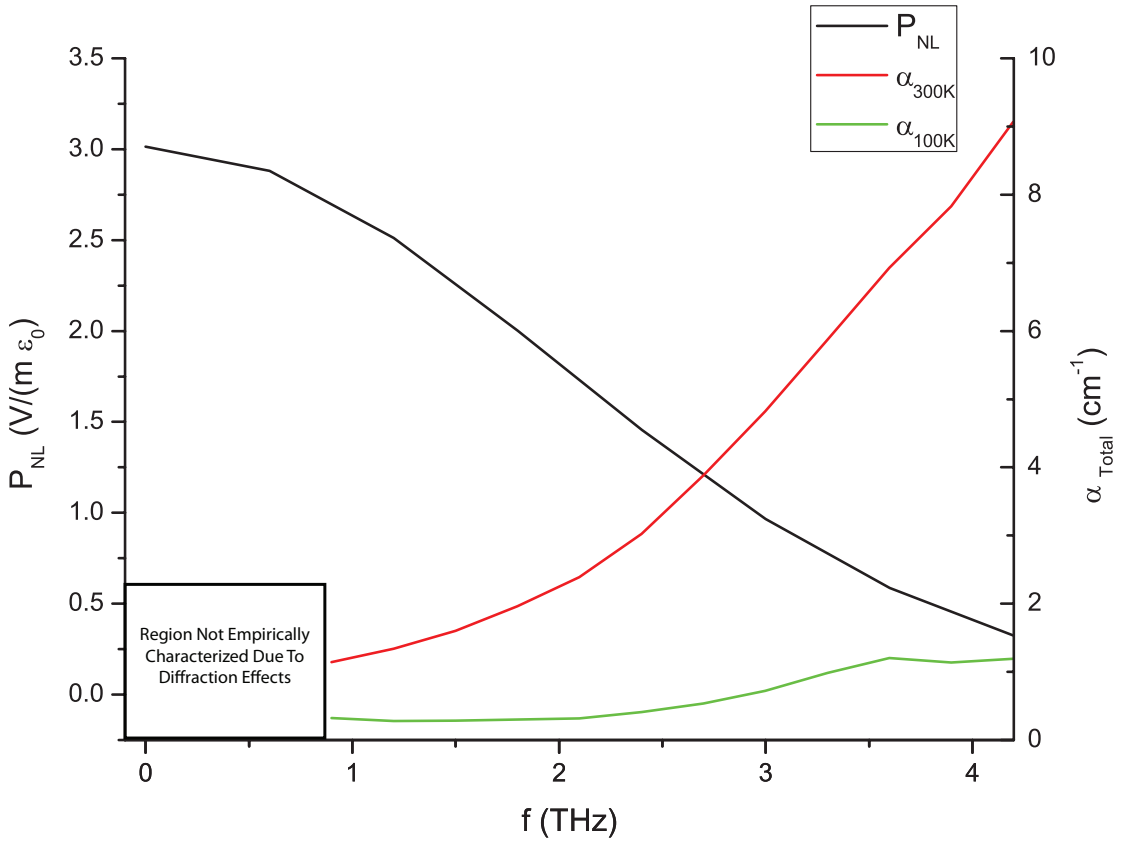


Figure 4.3: Nonlinear Polarization resulting from optical rectification of a Gaussian pulse in sLN with a temporal full width at half max of 40 fs, as well as empirically found absorption spectra for the room temperature and 100 K.

The spectral characteristics of the produced THz in the generating term will be dependent on the bandwidth of the laser pulse. The resulting nonlinear polarization from a 40 fs transform limited Gaussian laser pulse is shown in Figure 4.3. This plot shows the potential bandwidth generated by the autocorrelation of the laser pulse. The tail extends past the 4.5 THz value but virtually no power is generated in this spectral range due to the absorption peak at 4.5 THz.

#### 4.1.2.1 Absorption

The second term of interest is the absorption term. $\alpha(\omega)$ can be split into two parts, one related to the imaginary part of complex dielectric function that is temperature dependent, $\alpha_\epsilon$ and one part that is related to free carrier absorption, $\alpha_{fc}$, that has dependence on the intensity of the pump laser.

We will first examine the temperature dependent complex dielectric absorption. The absorption due to this can be viewed as arising from phonon-polariton resonances. The width of these resonances are strongly temperature dependent and their effects over the generating spectrum can be significantly reduced by decreasing the temperature.

The complex dielectric function from phonon-polariton modes is well described by a Lorentz oscillator model as explained by Yeh [55]. It can be used to find both the index of refraction, $n(\Omega)$, and the material dependent absorption, $\alpha_\epsilon$ found in Equation 4.8. To determine the dielectric function we look back at the explicit form of the polarization as a function of frequency in terms of lattice vibrations and the electric field:

$$P(\Omega) = b_{21}Q(\Omega) + b_{22}E(\omega) \tag{4.10}$$

The dielectric function can be extracted from the polarization,

$$P(\Omega) = \epsilon_0[\epsilon(\Omega) - 1]E(\Omega) \tag{4.11}$$

The lattice displacements are described by independent oscillators:

$$Q(\Omega) = \frac{b_{12}}{\Omega_i^2 - \mathrm{i}\Omega\gamma - \Omega^2} \tag{4.12}$$

Where $b_{21}$ and $b_{22}$ are material dependent oscillator strength coefficients. $\Omega_i$ is the resonant frequency of each mode and $\gamma$ is related to the width of the resonance spike, which has a strong dependence on temperature.

When we combine these equations we find the frequency dependent explicit form of the dielectric function:

$$\epsilon(\Omega) = 1 + \frac{b_{22}}{\epsilon_0} + \frac{b_{12}^2}{\epsilon_0(\Omega_i^2 - \mathrm{i}\Omega\gamma - \Omega^2)} \tag{4.13}$$

The dielectric function specifies both the absorption and the index of refraction by taking its real and imaginary parts,

$$\begin{aligned} n(\Omega) &= Re(\sqrt{\epsilon}) \\ \alpha_\epsilon(\Omega) &= -2\pi\Omega \ \mathrm{Im}(\sqrt{\epsilon}) \end{aligned} \tag{4.14}$$

The absorption spectral dependence for MgO doped stochiometric $LiNbO_3$ was experimentally characterized by Palfalvi [56]. Applying the results of these measurements we have curves for the material dependence of the absorption that we can apply to the measurement. These curves are shown in Figure 4.3.

The intensity dependent absorption is due to the creation of free carriers within the crystal that then absorb the THz as it propagates. This form of absorption is well described by Fulop [57] using the Drude model [58]. The free carrier absorption has a form similar to that of metallic or plasma absorption.

The density of the free carriers resulting from the laser pulse propagating through the crystal is determined by and expansion of the intensity of the pump

$$N_{fc} = \frac{\alpha_0 \tau I \lambda_0}{hc}(\alpha_0 + \frac{1}{2}\beta_2 I + \frac{1}{3}\beta_3 I^2) \tag{4.15}$$

where $\alpha_0 = \alpha_\epsilon(\omega_0)$ is the material response at the central frequency of the laser, $\tau$ is the pump pulse length, and $\beta_2$ and $\beta_3$ are the two and three photon absorption coefficients.

With this density we can specify a plasma frequency for the free carriers, $\omega_{pfc} = e\sqrt{N_{fc}/(\epsilon_0\epsilon_\infty m_{eff})}$, where $e$ is the electron charge, $m_{eff}$ is the effective

mass of the free carrier, and $\epsilon_\infty$ is the high frequency response of the dielectric function.

These free carriers couple to the electromagnetic field of the THz radiation as it propagates through the crystal, then scatter, resulting in loss of energy for the wave. This absorption process can be expressed by,

$$\alpha_{fc} = 2\frac{\Omega}{c}\ \mathrm{Im}\left[\sqrt{\epsilon_\infty\Big(1 - \frac{\omega_{pfc}^2}{\Omega^2 + \mathrm{i}\Omega/\tau_{sc}}\Big)}\right] \tag{4.16}$$

Here $\tau_{sc}$ is the scattering time of the free carriers, estimated to be 200 fs.

We can now combine these two forms of the absorption of lithium niobate into single spectral terms that corresponds to each temperature. These curves can be seen if Figure 4.8.

#### 4.1.2.2 Phase Matching

We lastly examine the phase matching factor in Equation 4.8. If we ignore all absorption terms and integrate to find the THz field generated, it will have a dependency that is proportional to $\mathrm{sinc}(\Delta k/2)$. While $LiNiO_3$ has a high effective nonlinear coefficient, the difference in the index of refraction between the THz ($n = 4.96$) and the group velocity of the pump (2.25) results in a of dephasing of $\pi/4$ in only 100 $\mu$m. This severely limits the amount of THz that can be generated.

To achieve phase matching in these nonlinear materials, one can select a material the has collinear phase matching, but this condition is only nearly matched in materials such as ZnTe or GaP which have an order of magnitude lower effective second order coefficients, as can be seen in Table 4.1.

Other phase matching methods include periodic poling of the material which allows the waves to catch up with each other as they undergo collinear propaga-

tion [59], or using pulse front tilting of the pump pulse.

Because of the results by Hebling et al. [60], we selected the pulse front tilt method of phase matching. The generation of the THz can be described by Huygen's principle, in which the point response of the material acts as a spherical wave. For an extended pump distribution the direction is parallel to the gradient of the envelope of the pump pulse and there can be controlled by tilting the pulse front. By tilting the pump pulse front along the phase matching angle in the material, the propagating THz will sample the same phase of the response of the material as it propagates through the crystal. This phase matching angle is determined by $\theta_{PM} = \cos^{-1}\left(v^{ph}_{THz}/v^{gr}_{800nm}\right)$ where $v^{ph}_{THz}$ is the phase velocity of the produced THz and $v^{gr}_{800nm}$ is the group velocity of the pump.

To pulse front tilt at this angle we need to develop an x-z linear correlation in the laser pulse using an angular dispersive optical element. We can describe the pulse front tilt, $\gamma_{tilt}$ from one of these elements by

$$\tan\gamma_{\text{tilt}} = \frac{n_{800nm}}{n^{gr}_{800nm}}\omega\frac{\mathrm{d}\Theta}{\mathrm{d}\omega} \tag{4.17}$$

Where $\mathrm{d}\Theta/\mathrm{d}\omega$ is the angular dispersion. Because we are using an ultrashort pulse, we prefer to not have material longitudinal dispersive effects such as pulse group dispersion found in prisms, therefore we choose to use a grating. Martinez [61] begins with the grating equation for an diffraction order m, central wavelength $\lambda$ and line spacing $d' = 1/N_{lines/length}$

$$\sin\theta_{in} + \sin\theta_{out} = \frac{m\lambda}{d'} \tag{4.18}$$

and finds the change from the central output angle in a small angle approximation

$$\Delta\theta_{out} = \alpha\Delta\theta_{in} + \beta\omega \tag{4.19}$$

Where $\alpha = -\cos(\theta_{in0})/\cos(\theta_{out0})$ is the mixing term between input and output angles and $\beta = m/(2\pi cd' \cos\theta_{out0})$ is the angular dispersion term we are looking for in Equation 4.17.

We can now choose a set of parameters for the grating in terms of the incident angle and the grating line spacing to choose a pulse front tilt angle to match the phase matching angle. We then use an achromatic lens to image the laser pulse into the crystal and we can achieve phase matching as the laser pulse propagates through the crystal.

There are two limitations to single lens imaging the pulse in this fashion. The first is any aberrations that may occur, such as astigmatism from lens tilt misalignment or spherical aberrations that may happen from the lens or curvature interface boundary at the crystal entrance.

With all of the terms modeled Equation 4.8 is then numerically integrated using a Runge-Kutta algorithm with zeros for the magnitude of the field's initial conditions. The results of these models are then compared to the measured THz spectra and are seen as the curves in Figure 4.8.

## 4.2 Experimental THz Generation

The THz generation and characterization experiments were performed using the Ti:Sapphire laser at the UCLA Pegasus lab. The relevant parameters are listed in Table 4.2

### 4.2.1 Experimental Setup of THz Generation

A diagram of the THz generation setup is shown in Figure 4.4. The laser pulse is sent to a diffraction grating of 900 lines per mm. The blazed grating is in an Littrow configuration to optimize efficiency scattering into the first order. An

| Pegasus Laboratory Laser Parameters | |
|---|---|
| Parameter | Value |
| Pulse Energy | 2 mJ |
| $\sigma_t$ | 35 fs |
| $\lambda_0$ | 800 nm |
| $\Delta\lambda$ | 30 nm |

Table 4.2: Pegasus laser parameters

achromatic lens with a focal length of 5 cm images the laser pulse from the grating to within the crystal with a magnification factor such that the pulse front is tilted at the phase matching angle.

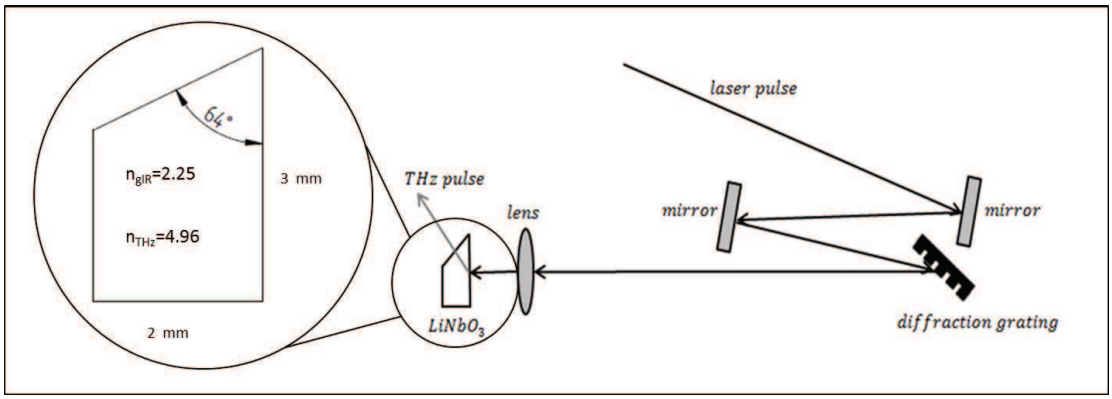


Figure 4.4: Experimental Setup of Single Cycle THz Generation via Optical Rectification

Using a golay cell that was cross-calibrated with pyro-electric detectors and a low pass filter with a cutoff at we were able to measure an optimal room temperature value for the single cycle pulse to be on the order of 1 $\mu$J. With the input pulse energy at 2 mJ, the conversion efficiency is about $10^{-3}$, a two order of magnitude increase over the conversion efficiencies of similar length materials such as GaP or ZnTe that have near collinear phase matching condition but lower second order dielectric coefficients.

#### 4.2.1.1 Cooling

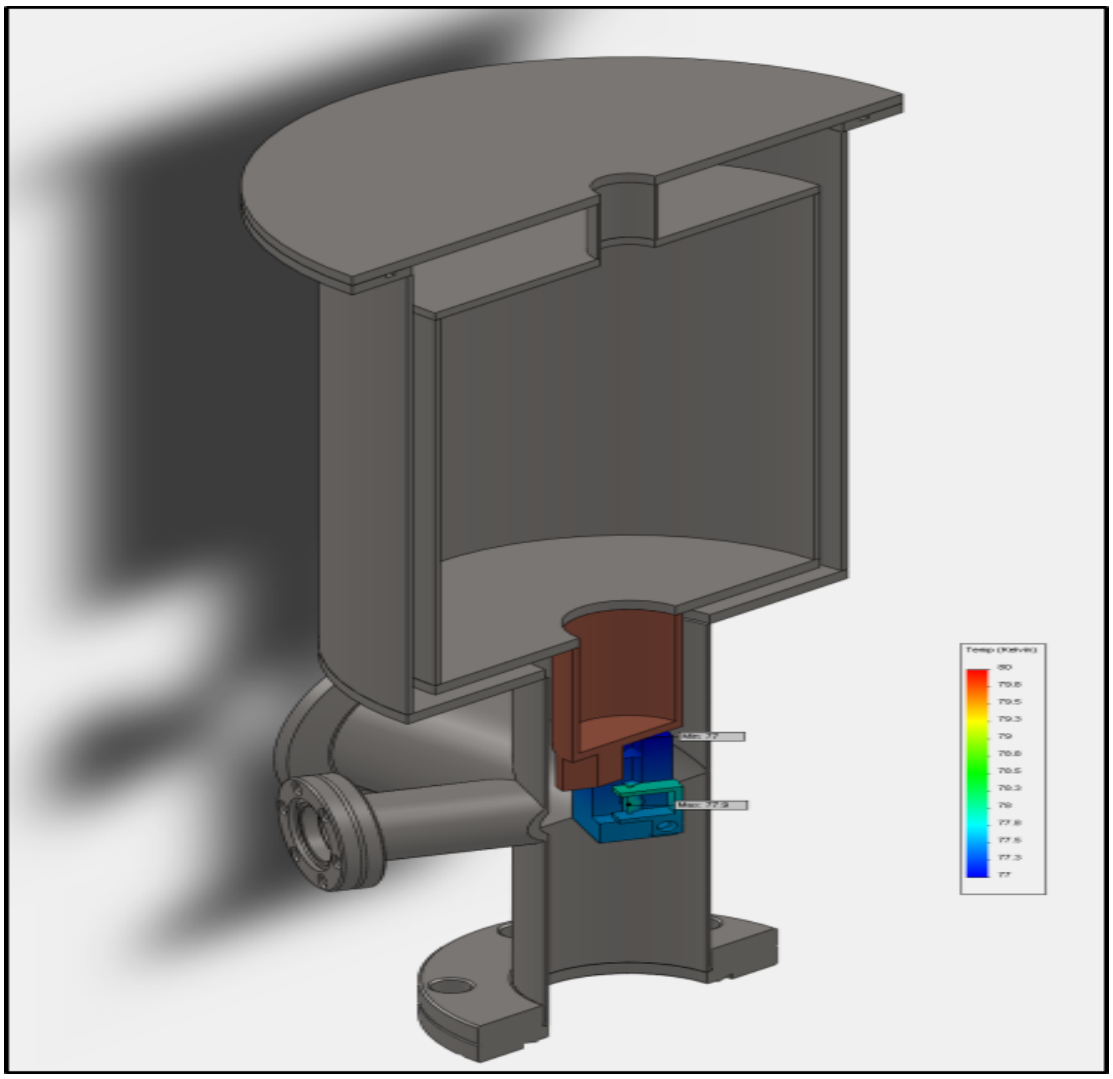

Figure 4.5: Cooling Chamber with Thermal Simulation

To further increase the efficiency by reducing the absorption due to the phonon-polariton resonance during THz generation a thermal device was designed to cool the crystal to 77 K by contact with liquid nitrogen.

The chamber was made of a vacuum with a laser quality window for the input laser as well as a THz transparent window to couple the THz out of the chamber. The crystal holder is made of copper for high thermal conductivity and has uses

vacuum safe thermal gel to ensure that crystal is thermally coupled to the copper. A stainless steel reservoir is filled with the liquid nitrogen. A thermal simulation is showed inf Figure 4.5, describing the equilibrated temperature profile of the crystal assuming that the copper surface is held at 77 K. Due to the decrease in the material absorption, an increase in the conversion efficiency can be nearly an order of magnitude as measured by calibrated Golay cell.

#### 4.2.1.2 Pulse Train Generation

In Chapter 3 we saw that the IFEL interaction's relies on slippage but will cease to interact if the envelope of the laser is on the same scale as the slippage. The THz pulses that are generated by our method are only a single cycle. This limits the electrons' interaction with the THz to only a few undulator periods. For significant modulation to take place this interaction length must be extended by effectively stretching the pulse. One option is to create a pulse train, by making several single cycle pulses that are spaced near the radiation wavelength.

A method of creating a pulse train is by using $\alpha$ Barium Borate crystals. These crystals have a well determined birefringence and the laser can be split rotating these crystals such that the electric field of the linearly polarized laser is at 45 degrees between the fast and slow axes. The delay between the two pulses are specified by $\Delta t = L/c(n_o - n_e)$, where $L$ is the length of the crystal, $n_o$ is the ordinary index of refraction and $n_e$ is the extraordinary index of refraction. The crystals can be stacked to make a pulse train where the number of pulses are $2^N$ where $N$ is the number of crystals. This has the advantage of being able to tune the spacing of the THz pulses by adjusting the length of each crystal but also results in dividing the pump energy and therefore the intensity by up to a factor of $2^N$.

Another option is to place the single cycle pulse into a waveguide, which will

increase the phase velocity of the THz wave but decrease its group velocity. A waveguide mode could be chosen such that the electron beam can propagate at near the group velocity of the THz pulse while the undulator parameters can be chosen to match the resonant condition and have optimal electron beam modulation.

### 4.2.2 Measurements

To successfully characterize the THz source, the methodology to measure it should be understood. The autocorrelation function of the THz pulse can be measured using interferometry, then through the Wiener-Khinchin autocorrelation theorem [62], we can determine the power spectrum of the THz pulse.

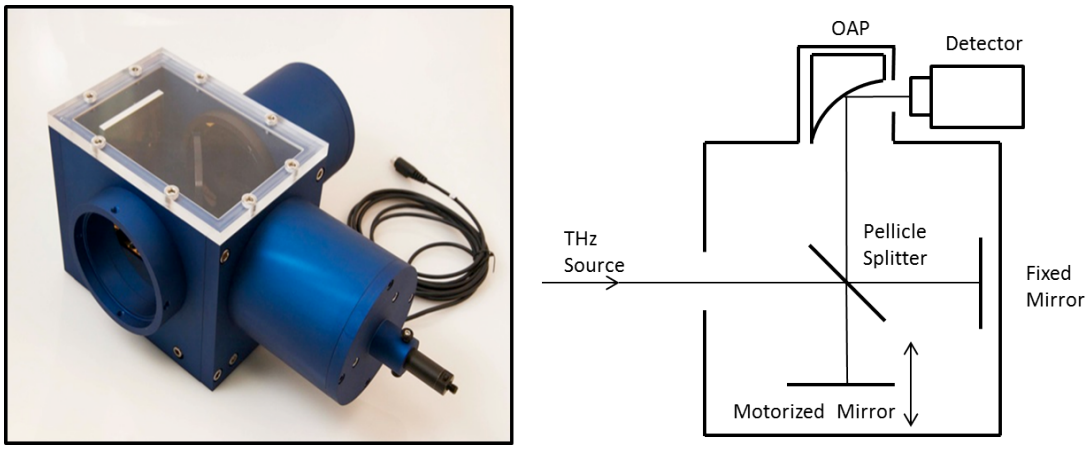


Figure 4.6: BLIS Interferometer

Figure 4.6 shows the device that was used to measure the autocorrelation of the THz signals. The Bunch Length Interferometer System (BLIS) is a Michelson type interferometer that was developed by Radiabeam Technologies. The incoming THz pulse is split by a Pellicle beam splitter that sends 50 % of the pulse energy to a fixed arm, while the other half of the energy goes to a mirror on a translation stage that can be controlled to the precision of tens of nanometers. The relative path length then can be adjusted and half of the original pulse energy is focused

into a Golay Cell detector after being recombined at the beamsplitter. The other half of the pulse energy leaves in the direction of the THz source.

If we have a complex electric field from the THz signal called $E0(t)$ impinging on the interferometer, then, is split, has one quarter of the pulse delayed the moving arm by a time $\tau$, then the field at the detector by superposition will be

$$E_{det}(t,\tau) = \frac{1}{2}\Big[E_0(t) + E_0(t-\tau)\Big] \tag{4.20}$$

The signal measured by the detector, however will be an integrated intensity, or

$$S(\tau) \propto \int E_{det}(t,\tau)E^*_{det}(t,\tau)\mathrm{d}t \tag{4.21}$$

Expanding out the terms we end up with a Signal that looks like

$$S(\tau) \propto \int \mathrm{d}t \, \Big(|E_0(t)|^2 + |E_0(t-\tau| + 2\big(E_0(t)E^*_0(t-\tau)\big)\Big) \tag{4.22}$$

The first two terms of the signal are equal and constant with respect to the delay. The third term is the autocorrelation function of the pulse, that which we desire to measure. To extract it from the signal the constant background must be subtracted. We can now take the Fourier Transform of the autocorrelation function and by the Wiener-Khinchin Theorem we now have the Power spectrum for the pulse.

A sample raw measurement is taken from and power spectrum from the interferometer is shown in Figure 4.7. Because a second detector is not used to normalize the input energy of the THz pulse, each delay position is sampled for a population of 5 measurements, then averaged. The subtraction of the average of the entire signal is usually enough to eliminate the DC components and extract the autocorrelation. On occasion a small misalignment can result in a small linear

increase in the autocorrelation signal. As the signal should be symmetric around the main peak where there are equal path lengths, this is a misalignment artifact and can be removed through low pass filtering, linear fitting, and subtraction of the linear behavior to obtain the autocorrelation function.

The power spectrum is then determined by taking using the fast Fourier transform algorithm. This spectrum peaks around 1 THz but has very little power in lower frequencies due to the fast diffraction of these spectral components, resulting in their absence at the detector. The spectral modulation is a result of the strong absorption of THz by water.

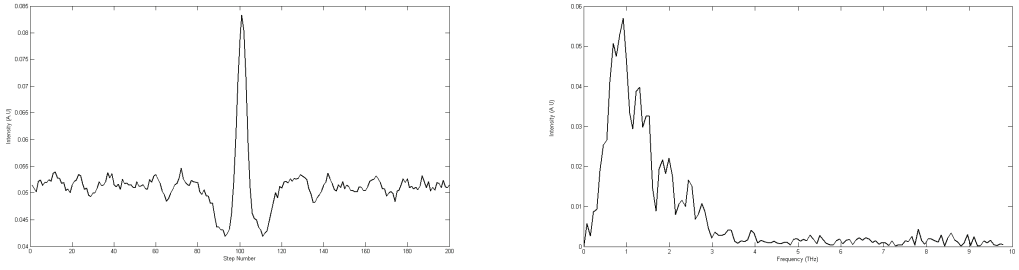

Figure 4.7: Sample signal (left) and resulting power spectrum (right) for a single THz measurement.

### 4.2.3 Results of THz Source Characterization

The results of the characterization of the optical rectification THz source can be seen in Figure 4.8. The integration model discussed earlier was compared with the average of ∼30 power spectra taken both at room temperature of 300 K and at liquid nitrogen temperatures of 77 K. The left scale for the power spectral density was normalized by the pulse energy as measured by the Golay cell.

A significant increase in the power spectral density can be seen both in its amplitude and the extension into higher frequencies as a result of cooling to liquid nitrogen temperatures. The models tend to overestimate the damping at lower

frequencies due to the free carrier model, however this may be a result of some of the less precisely determined parameters in the model such as the effective mass of the free carriers. The water spectra are shown at the top to give insight into the spectral modulation seen, particularly in the 77 K case.

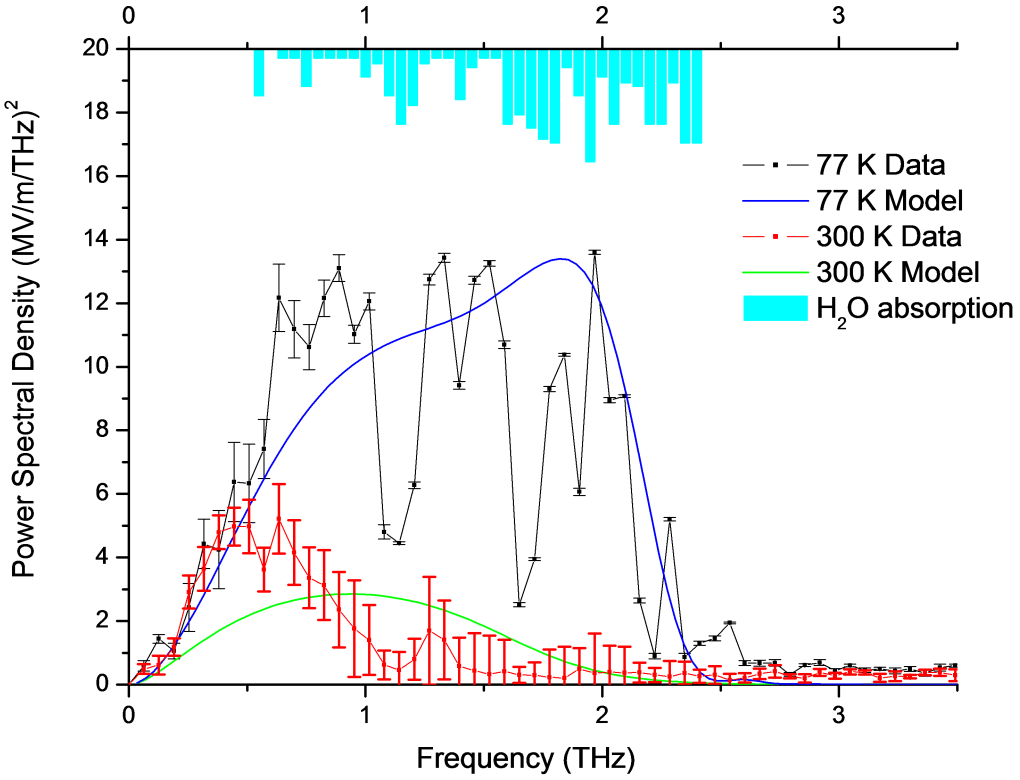


Figure 4.8: Results of THz Characterization

This experiment demonstrated that significant power can be generated in the spectral region up to 2 THz using this laser locked radiation source. With the source characterized we can now discuss interacting this source's radiation with a relativistic electron beam in an undulator for the purposes of compressing and synchronizing a high brightness electron beam for injection into a laser driven application.

## 4.3 Description and Simulation of Proposed THz experiment

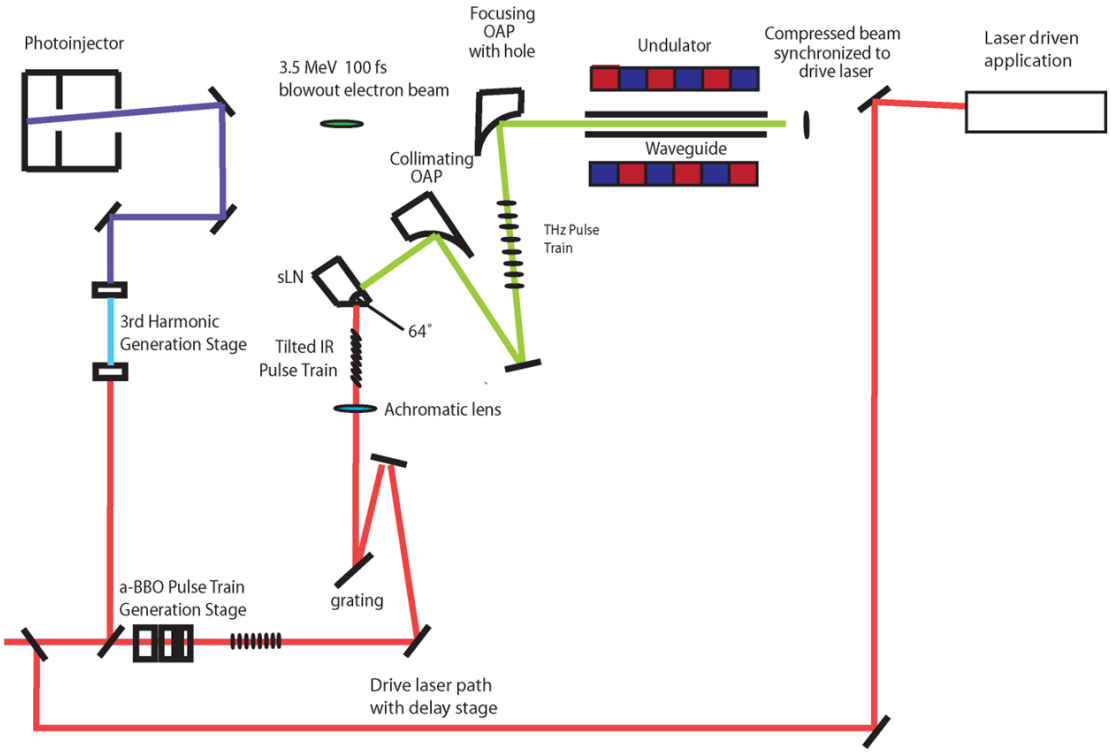


Figure 4.9: Experimental Setup of OR

The interaction of laser locked THz radiation with a photoinjector driven has been proposed at the UCLA Pegasus lab. In this scheme, a high intensity laser pulse used to drive an application such as a laser wakefield accelerator, is split into two additional arms: One to drive a photocathode and the second to generate a THz pulse train to interact with the electron beam to compress it and compensate for the loss of synchronization with the driver laser that occurs from RF phase jitter in the photoinjector gun. A conceptual diagram of this experiment can be seen in Figure 4.9.

Table 4.3 shows the parameters selected for the IFEL compression and synchronization experiment. The laser strength parameter, $K_l$ is the value set by an

| THz IFEL Parameters | |
|---|---|
| Parameter | Value |
| $K_l$ | $4.2 \cdot 10^{-3}$ |
| $K$ | 1.6 |
| $JJ$ | 0.84 |
| $\gamma_r$ | 7.0 |
| $\lambda_u$ | 1.7 cm |

Table 4.3: Compression and Synchronization Experimental Parameters.

8 pulse THz train with each single cycle pulse's central frequency at 1 THz, and longitudinal separation of a wavelength. The total energy of this train should be 10 $\mu$J to achieve this laser strength parameter. The injection energy from the electron beam 3.5 MeV, as is achievable from the Pegasus photoinjector.

### 4.3.1 Modeling of IFEL Interaction in Proposed Experiment

The preliminary investigation of this interaction was performed by integrating the 1-D equations of motion seen in Chapter 3. These equations were numerically integrated using a Runge-Kutta algorithm with initial conditions set by the particle set expected by the chirp of 1 pC ultrashort beam with a temporal RMS value of 100 fs.

#### 4.3.1.1 Results of 1-D Integration model

The results of the 1-D integration can be seen in Figure 4.10 and Figure 4.11. The left side of Figure 4.10 shows the particle beam injected into the IFEL interaction. The horizontal axis if displayed in time, meaning that the right side of the distribution arrives at a longitudinal position later than the left side, representing a positive chirp. At the exit of the undulator we see full compression down to an

RMS value of 14 fs, resulting in nearly an order of magnitude compression of an ultrashort electron beam.

The synchronization was studied by varying the central average time of arrival (TOA) that the electron beam is injected into the IFEL, thus with respect to the laser phase. Examining the final average TOA of the electron beam at the exit of the undulator, we see that there is an order of magnitude reduction in the variation. For the selected parameters, this effect will begin to break down for cases in which the time of arrival jitter is much bigger than 200 fs.

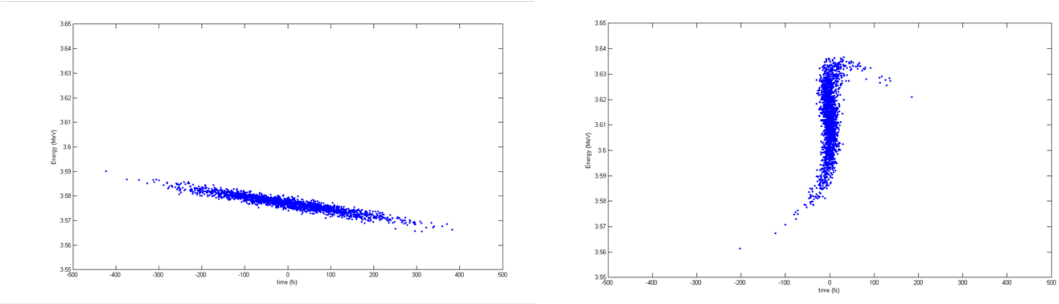

Figure 4.10: Compression of ultrashort beam. A 100 fs RMS beam is injected into the IFEL. The results

This study was performed with no question to the effects of the energy jitter. There is an effect of energy jitter simply due to the $R_{56}$ of the undulator which can be describe by [63]:

$$R_{56Und} = \frac{N\lambda_u}{\gamma_0^2} + \left(\frac{3NK^2\lambda_u}{2\gamma_0^2}\right) \tag{4.23}$$

For the parameters selected in this experiment, the $R_{56}$ for the undulator is 1.3 cm. This sets a limit on the amount of energy jitter than the electron beam can acquire from the RF photogun. For a jitter of 50 fs resulting from this effect, the electron beam must have an energy jitter of less than 0.1 %. This figure is achievable by modern RF systems.

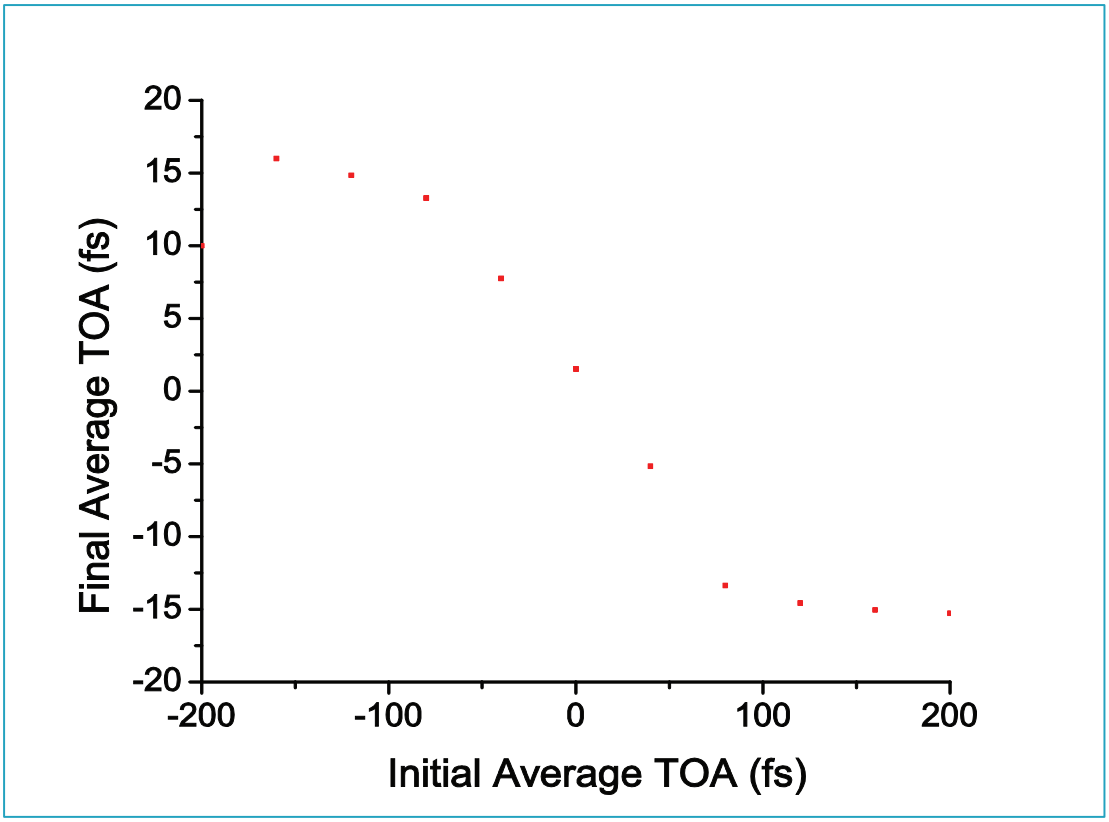


Figure 4.11: Synchronization of ultrashort beam by THz IFEL interaction. The final average time of arrival (TOA) is reduced by roughly an order of magnitude compared to the inital average TOA.

#### 4.3.1.2 3-D Simulation

To include three dimensional effects, the interaction was then modeled with a start-to-end simulation. A 1 pC electron beam is created at the photoinjector and propagated using the commercial particle tracing code, GPT. The beam is then imported into the FEL code, Genesis 1.3 [64], at a location one meter downstream from the cathode.

The Genesis 1.3 model uses a 2 mm x 2mm rectangular boundary. The modified parameters to meet the resonance condition with the waveguide mode are an undulator strength parameter of $K = 0.829$ with a resulting coupling factor of

$JJ = 0.93$. The initial THz transverse profile is modeled as a Gaussian pulse with a RMS spot size of 500 $\mu$m. The electron beam is focused by quadrupole magnets so that it is matched to the focusing channel established by the undulator with an entrance spot size of 150 $\mu$m. All other parameters from the 1-D case remain the same.

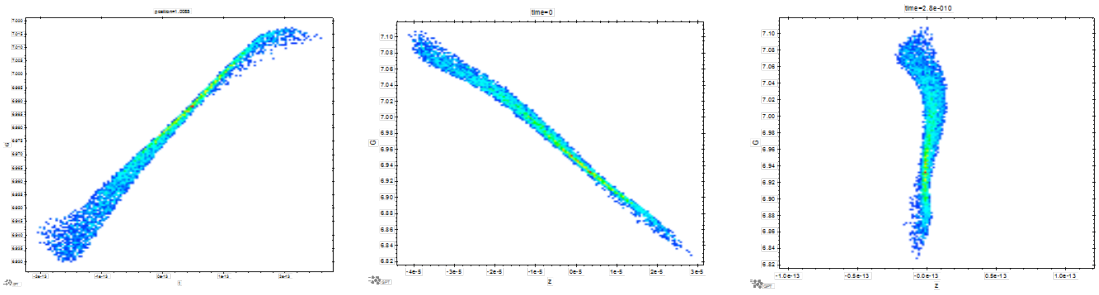

Figure 4.12: Results of 3-D simulation using GPT and Genesis 1.3

The results of the 3-D study is shown in Figure 4.12. With this parameter set the coupling is a weaker, resulting in a beam at the output of the undulator that is not fully compressed, but has a strong negative chirp. After a drift of 9 cm from the exit of the undulator, the electron beam reaches a fully compressed state of 6 fs RMS.

# CHAPTER 5

# High Gradient IFEL Acceleration at LLNL

In this chapter we discuss discuss an experiment where the IFEL interaction was used for high gradient acceleration. This experiment represents the first time an IFEL accelerator was driven by a high intensity short pulse (sub-ps) laser system. The experiment was performed at Lawrence Livermore National Laboratory (LLNL) in Building 194. This facility houses a 100 MeV electron linac that was used to measure many fundamental nuclear cross-sections [65]. In the last decade, the accelerator complex has been used for X-ray and gamma-ray production. X-rays have been obtained colliding the high brightness electron beam from an RF photoinjector with a high energy laser pulse in the PLEIADES and TREX [66] experiments. The IFEL experiment was funded as a potential injector for a future compact gamma-ray production facility for nuclear material detection based on photofission or nuclear resonance fluorescence.

## 5.1 Experimental Description

The experimental setup can be divided into three components: the electron beam source, the laser system and the interaction region. The modeling of each of the components is explained as each component is discussed. First we look at the electron beam generation and acceleration and chirping. The interaction laser and the photocathode drive laser will then be explained, and lastly, the interaction area and diagnostics.

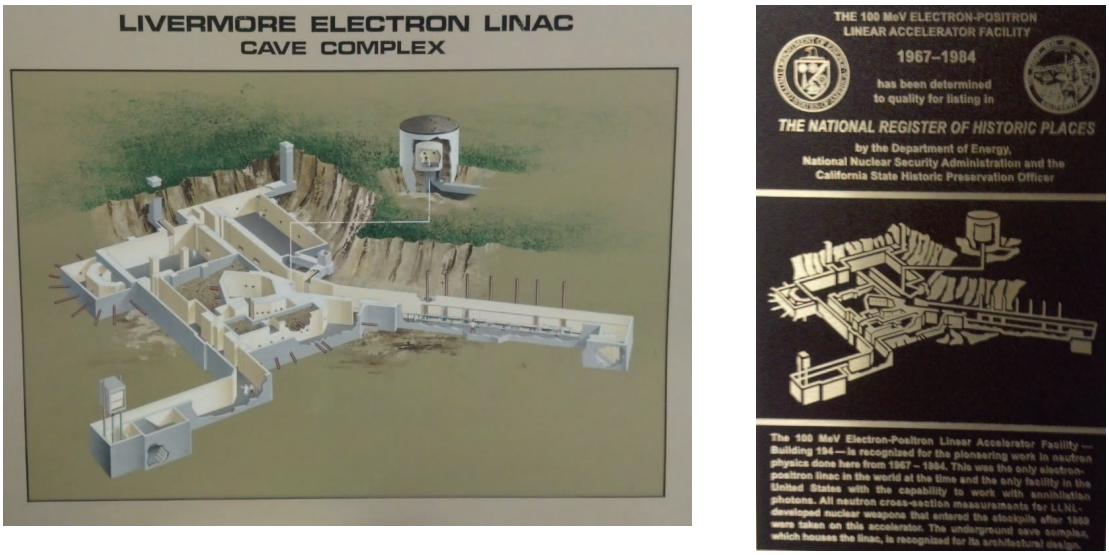


Figure 5.1: Building 194 Artist rendering and Historical Plaque

### 5.1.1 Electron Linac Beamline

The electron beam is generated by a SLAC/UCLA/BNL 1.6 Cell photoinjector gun of the same design as that in the Pegasus Laboratory in the blowout experiments seen in Chapter 2. A short ultraviolet (UV) laser pulse (260 nm) that is discussed illuminates the copper cathode to produce the electron beam. For these experiments we operate at a charge of 100-500 pC per pulse as a compromise to provide a strong signal on the various beam and timing diagnostics and to limit the beam quality degradation which occurs at very high ($\sim$ nC) beam charges. The UV laser applied to the cathode is 120 fs full width at half maximum (FWHM)and its transverse mode was a Gaussian distribution with cut tails obtained by relay imaging of an overfilled 1 mm pinhole onto the cathode. Considering these initial electron beam parameters, we can calculate the figure of merit for determining the effects of the nonlinearity in the photoinjector blowout regime. This is given by the ratio of the electric field due to the surface charge density of the initial beam distribution, $E_{sc} = \sigma_{surface}/\epsilon_0$ to the RF accelerating field at the cathode, $E_{rf} = (120\ \mathrm{MV/m}) \sin\phi$, where $\phi$ is the injection phase. The figure of merit values

ranged from 3-14 % for the operational range of charges. From the investigation of the photoinjector blowout regime in Chapter 2 we know that when this ratio exceeds 10 %, space-charge driven nonlinearities degrade the quality longitudinal phase space, preventing optimal compression.

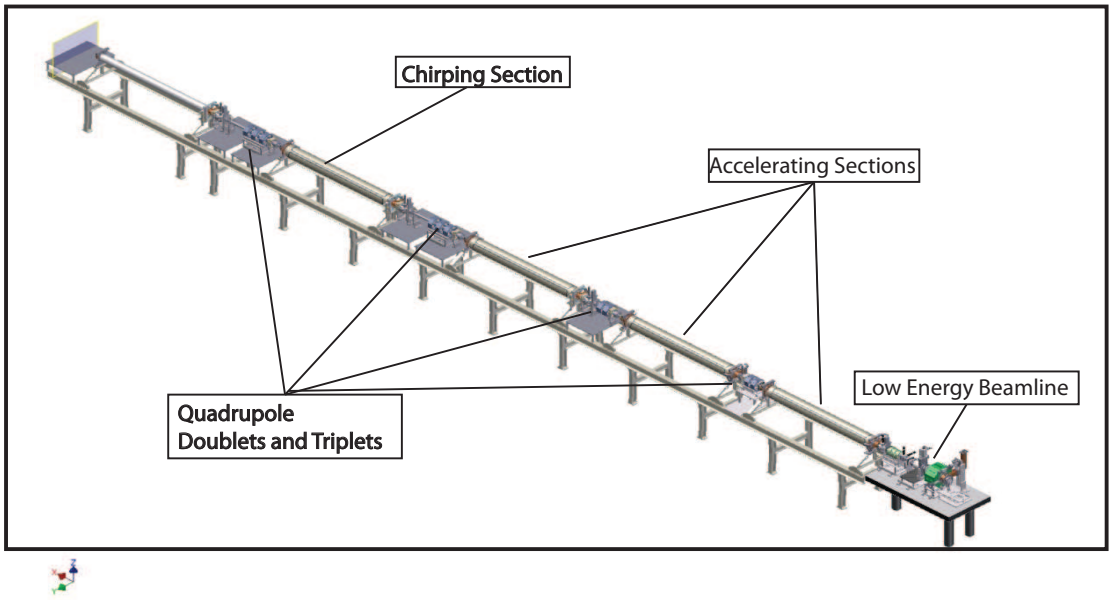


Figure 5.2: Building 194 Linac Beamline. The low energy section is visible after the RF photoinjector at models right side. The beam can them be accelerated by 5 3 m long RF linacs with inter-spaced matching quadrupole sections.

The RF gun and solenoid were modeled using the Superfish and Parmela codes by Los Alamos National Laboratory (LANL) [67] [68]. Superfish solves Maxwell's equations on a mesh using boundary conditions to obtain the RF fields in the gun and Parmela is a particle tracing code that solves the equations of motion of the particles in any external fields and tracks the evolution of the 6D phase space including the effects of space charge. In addition, the Parmela code was compared to a model of the beam was developed using an independent commercial particle tracing computer code, General Particle Tracer (GPT) [69] and their results were found to be consistent.

Before the first accelerating section the low energy beamline is formed by three skew quads to compensate for any transverse mixing that occurs in the gun and solenoid, an integrated current transformer (ICT) to measure the charge of the electron beam, and a set of slits to perform an emittance measurement on the beam. The normalized emittance was measured for 100 pC case to be 2 mm·mrad.

As the beam is accelerated in the gun, the solenoid controls its spot size and minimizes the emittance using the emittance compensation scheme and by matching the beam to the invariant envelope solution [70] at the entrance to the first RF accelerating section.

The 3 m SLAC style accelerating sections [71] are designed to get a constant gradient acceleration (by tapering the shunt impedance) of 25 MeV per section. LLNL Bldg. 194 has 5 sections available to accelerate the electron beam. The IFEL requires an injection energy of 50 MeV so that three sections are minimally needed. However, in order to have more flexibility, four RF linac sections are used to inject the into the IFEL at a higher energy and to allow running off crest for compression. This also has the advantage of running the linacs at a lower average accelerating gradient, easing the power requirements on the relatively aged RF kystron systems. A model of the section is shown in Figure 5.2. The first three sections are run with an on crest phase to use the maximum gradient and are used to accelerate the electron beam up to the chosen injection energy. The last section is run at a compressing phase to imbue a negative energy chirp on the electron beam so that a magnetic chicane can compress it.

Quadrupole doublets and triplets are used to collimate and control the beam as it propagates through the accelerating sections, particularly to compensate for the defocusing kicks that the electrons receive as they exit the sections.

A Parmela simulation of the beam evolution through the linac is shown in Figure 5.3. Plot a) of this figure shows the normalized transverse emittances and the average energy, $E$ of the beam. Looking at the energy evolution of the beam,

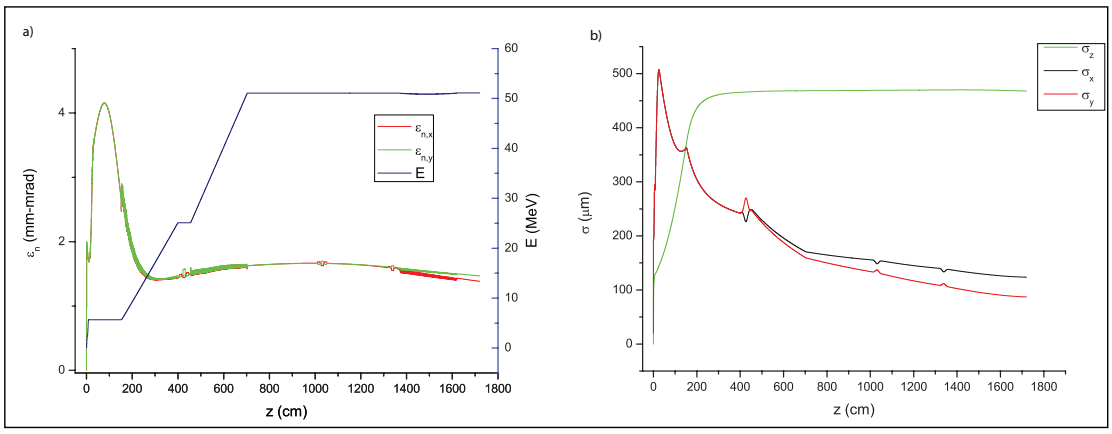


Figure 5.3: Results of beam acceleration using the Parmela tracing code. a) Normalized emittance in x,y as and energy. b) Longitudinal and transverse RMS spot sizes.

one can see the increase resulting from each of the RF sections, with the third section being close to zero and the small dip in the average energy as the beam is chirped at the last section.

Plot b) of Figure 5.3 shows the transverse and longitudinal RMS spot sizes during the linac section. After matching the transverse spot size of the beam to the invariant envelope at the first accelerating section, the spot size is controlled with quadrupole magnets, compensating for the defocussing kicks that occur at the exits of the accelerating sections. The longitudinal RMS pulse length expands during the blowout process then stops evolving as the space charge forces and velocity differences between the particles become negligible for $\gamma >> 1$.

### 5.1.2 Laser

The laser system has the double function of driving the IFEL acceleration process and of generating the electron beam at the photocathode. The amplification system is a chirped pulse amplifier (CPA) design, which is the standard for current ultrafast lasers. In CPA, high bandwidth laser pulses are produced in an ultrafast

oscillator. These pulses are then stretched by imposing a linear chirp using an aberration free Offner stretcher, amplified by 6 orders of magnitude in a regenerative amplifier, and a multi-pass amplifier provides the remaining amplification to the required pulse energy. Finally the laser is compressed back to the original pulse length using a grating based compressor. CPA allows for the generation of very high intensity compressed laser pulses as the intensity during the amplification process can be held below the damage threshold of the lasing media using high stretching ratios. The Centarus X laser system, purchased from Amplitude Technologies, is a 10 Hz Titanium-Sapphire based system. In the following sections we will describe the system from oscillator to the preamplifier then describe the two paths that lead to the photocathode and the interaction point at the undulator. The laser parameters are summarized in Table 5.1 .

#### 5.1.2.1 Oscillator and Stretcher

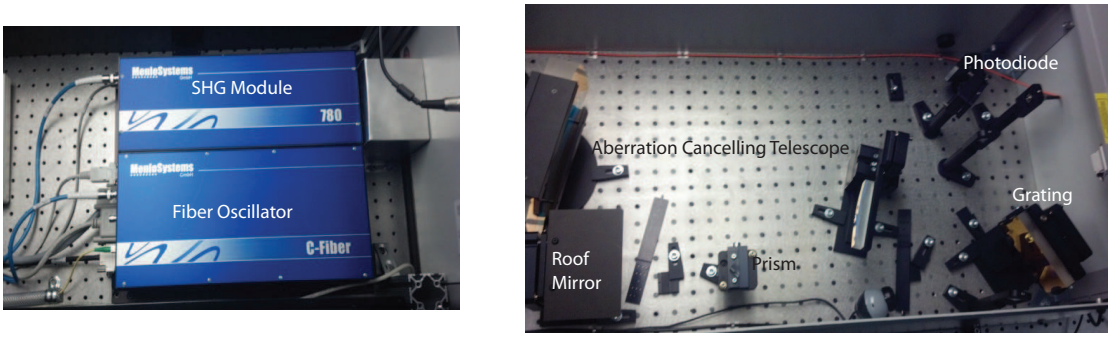


Figure 5.4: Oscillator and Stretcher for Front End Laser System.

The laser's oscillator is a C-fiber 780 erbium doped fiber oscillator developed by MenloSystems. It produces a pulse train with a repetition rate of 100 MHz with a minimum pulse length of 120 fs FWHM and an energy of 1 nJ per pulse of 10 nm bandwidth laser light centered on 780 nm. The erbium doped fiber generates IR light at 1560 nm which is then cover 780 nm using second harmonic generation crystals. Although the bandwidth is limited compared to titanium-sapphire oscil-

lators that can have bandwidths of 40 nm and produce pulse widths of only 35 fs, the fiber oscillator is far more stable, requiring no alignment adjustments over the duration of the experiment.

The pulse train of the oscillator is then stretched to 300 ps in an Offner stretcher [72]. This design of uses a single grating, prism, a reflective telescope, and a roof mirror to provide compact, aberration free stretching of the laser pulses. The prism and grating work together to provide dispersion with minimal higher order spectral phase distortions, while a telescope comprised of concave and convex mirrors force the spectral components to cancel any aberrations that may have been acquired from the optics or gratings. These aberrations would result in a lack of cancellation of the dispersion at the exit of the stretcher, and in non-optimal compression after the amplification.

| Laser Parameters | |
|---|---|
| Parameter | Value |
| Interaction Laser Pulse Energy | 500 mJ |
| Photocathode Drive Laser Energy | 3 mJ |
| Compressed Pulse Temporal FWHM | 120 fs |
| Central Wavelength | 780 nm |
| Bandwidth | 10 nm |

Table 5.1: Laser Parameters

#### 5.1.2.2 Amplifiers

After stretching occurs the laser pulse train then enters a regenerative amplifier that amplifies the energy of the pulses from the nJ scale to the mJ scale. A diagram of the regenerative amplifier can be seen in Figure 5.5. The regenerative amplifier uses Brewster Polarizers and two Pockels cells to close and open a resonant cavity so that the pulse to be amplified passes through the and close a cavity. Brewster

Polarizers work using Brewster's angle, defined as

$$\theta_b = \arctan\left(\frac{n_2}{n_1}\right) \tag{5.1}$$

here $n_2$ and $n_1$ are the indices of refraction for the selected material. At this angle of incidence to a material interface there will be no reflected light if the laser has p polarization. The laser pulse enters the regenerative amplifier cavity from the stretcher with s polarization, causing it to reflect off the first two polarizers and propagates through the lasing material and to the first Pockels cell. The Pockels Cell acts on the polarization of the laser pulse, by acting as a quarter waveplate twice as the laser pulse travels through it, refects off of the end of the cavity mirror and back through the Pockels cell, changing the polarization to from s to p. With p polarization the laser pulse travels through the gain media, back through the Brewster polarizers to the other Pockels cell which has no effect until about 10 round trips occur, when the amplification of the laser pulse reaches saturation. When saturation occurs, the second Pockels cell is switched on and the laser pulse switches back to s polarization, reflecting out of the regenerative cavity to further amplification.

Each time the laser pulse passes through the lasing medium it acquires phase delay dispersion(PDD). This changes the chirp set by the stretcher and the compressor parameters may need to be adjusted if the number of round trips through the regenerative amplifer is changed from the design value. A photodiode monitors the bleed through of the second end cavity mirror to assist in adjustment of the Pockels cell timing and alignment of the cavity to the proper build up time of the amplification process.

The laser pulse is further amplified by two four-pass amplifers. The first amplifier increases the laser pulse energy from 3 to 30 mJ. 3 mJ of the laser energy is split off and sent to drive the photoinjector, while the remaining 27 mJ is sent

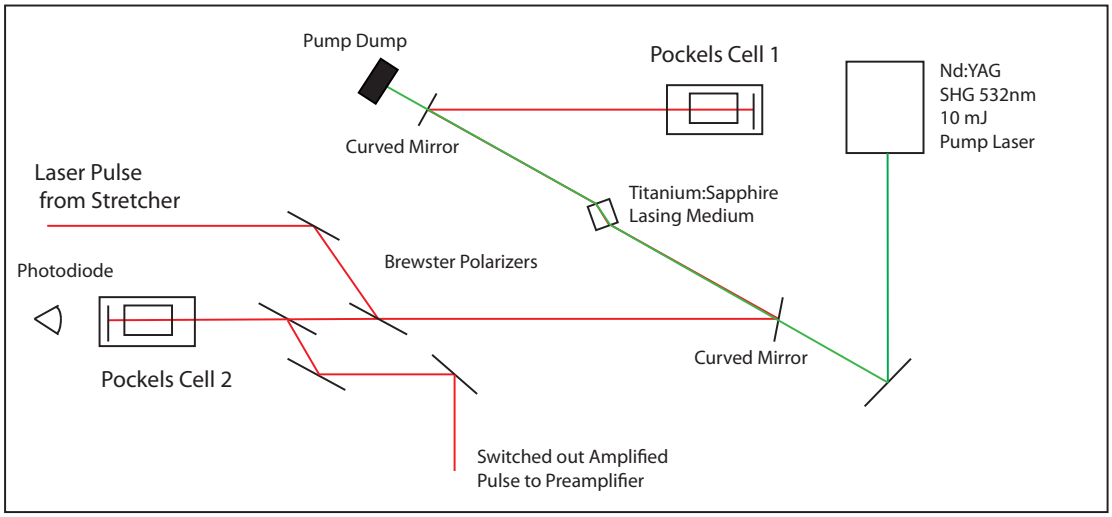


Figure 5.5: Diagram of Regenerative Amplifier. The Regenerative amplifier uses the first Pockels cell to close the cavity, resulting in 10 round trips of the laser pulse through the Ti:Sapphire lasing material. After saturation occurs a second Pockels cell switches out the amplified pulse to go to secondary amplifiers.

to a second Ti:Sapphire amplifier, increasing the energy from 27 to 700 mJ.

#### 5.1.2.3 Compressor

The compressor for the photocathode drive laser consists of a simple two grating configuration to undo the chirp placed on the laser from the stretcher and PDD acquired in the lasing gain media. The laser is then frequency multiplied from 780 nm to 260 nm for application to the photocathode to generate the electron beam.

The main interaction laser has a similar design as the photocathode drive laser arm but scaled up and placed in vacuum to avoid the nonlinear breakdown effects and self focusing in air when dealing with a TW scale peak power laser.

To verify that the interaction laser was compressed to its transform limit, we used of a Swamp Optics Grenouille system [73] which records the spectrogram

(time and frequency) of the laser pulse and has a computer algorithm that can reconstruct the phase and amplitude of the optical waveform using second harmonic generation frequency resolved optical gating (SHG FROG).

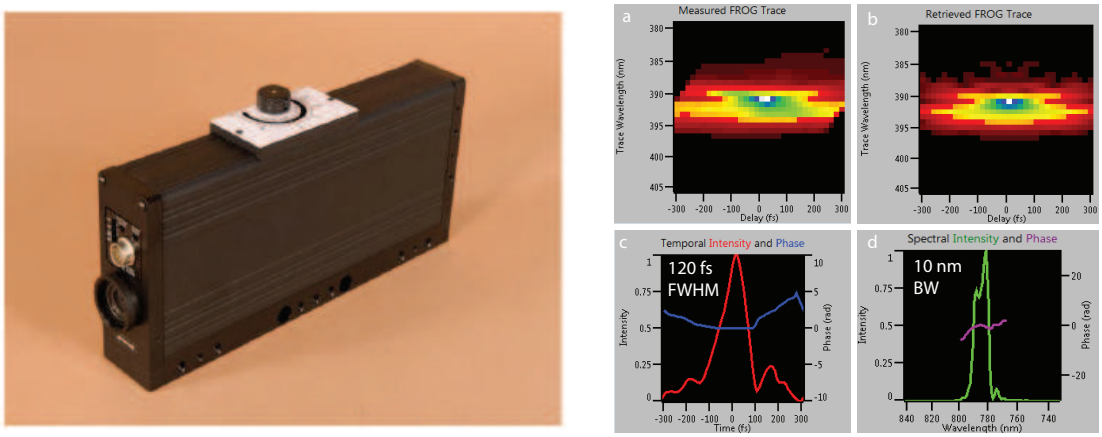


Figure 5.6: Swamp Optics Grenouille and Pulse Length Measurements.(Left) physical picture of the diagnostic.(Right) a. Measured spectrogram b. Reconstructed spectrogram. FROG reconstructed profiles of time (c) and frequency (d).

### 5.1.3 Interaction Area

A diagram of the interaction area is shown in Figure 5.7 We will break down the interaction area into its components: the compression of the electron beam, the undulator region, the timing diagnostics, and the beam spectrometer.

#### 5.1.3.1 Chicane

Since IFEL acceleration only occurs when the electron beam is temporally overlapped with the short pulse laser system, a magnetic chicane was designed to compress the electron beam so that the maximal amount of the beam can be captured and accelerated. The left side of Figure 5.7 shows the chicane. The magnetic chicane compressor functions by imparting a correlation between the longitudinal

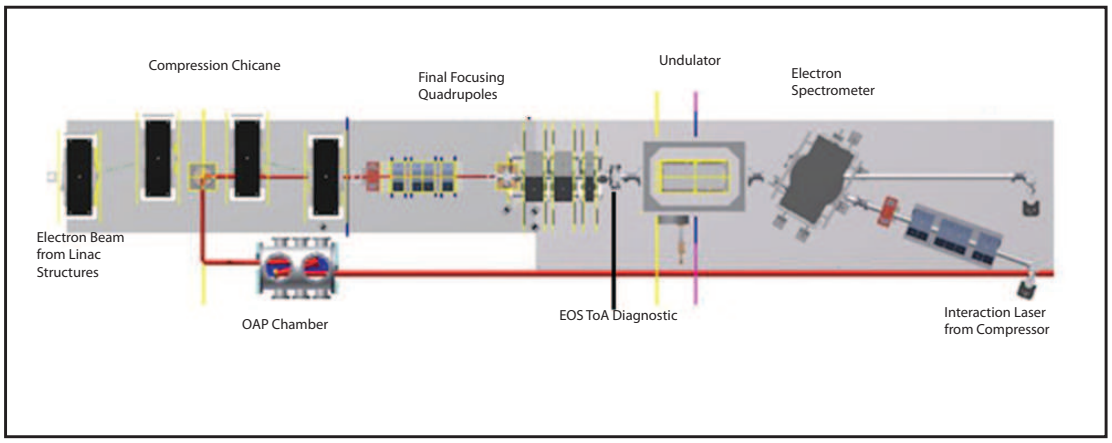


Figure 5.7: Interaction Area. The high power interaction laser approaches from the right side is focused in the OAP chamber, goes through a periscope that preserves its horizontal polarization, and is sent down the beamline on axis in the center of the chicane compressor. The electron beam approaches from the left, is compressed in the chicane, and is focused to a waist at the center of the undulator by two quadrupole triplets.

position of a given particle with it's energy or a nonzero $R_{56}$ element of the transfer matrix. Particles with higher energy will travel a shorter path length, resulting in an earlier time of arrival at the end of the chicane with respect to the design particle. For a chicane with four equal dipole magnets of length $L_{dipole}$ separated by drift length $L_{drift}$ and deflecting the beam be angle $\theta$ longitudinal position / energy correlation is given by

$$R_{56} = 2\theta^2(L_{drift} + \frac{2}{3}L_{mag}) \tag{5.2}$$

Given the constraint imposed on the maximum amount of chirp that can be imbued on the electron beam set by the maximum field in the chirping accelerating

section, the chicane compressor is designed to have an $R_{56}$ of 5.66 cm.

Propagation of the beam through the chicane was modeled using Elegant [74]. This simulation code offers a one dimensional model to compute the energy modulation on the beam due to coherent synchrotron radiation.

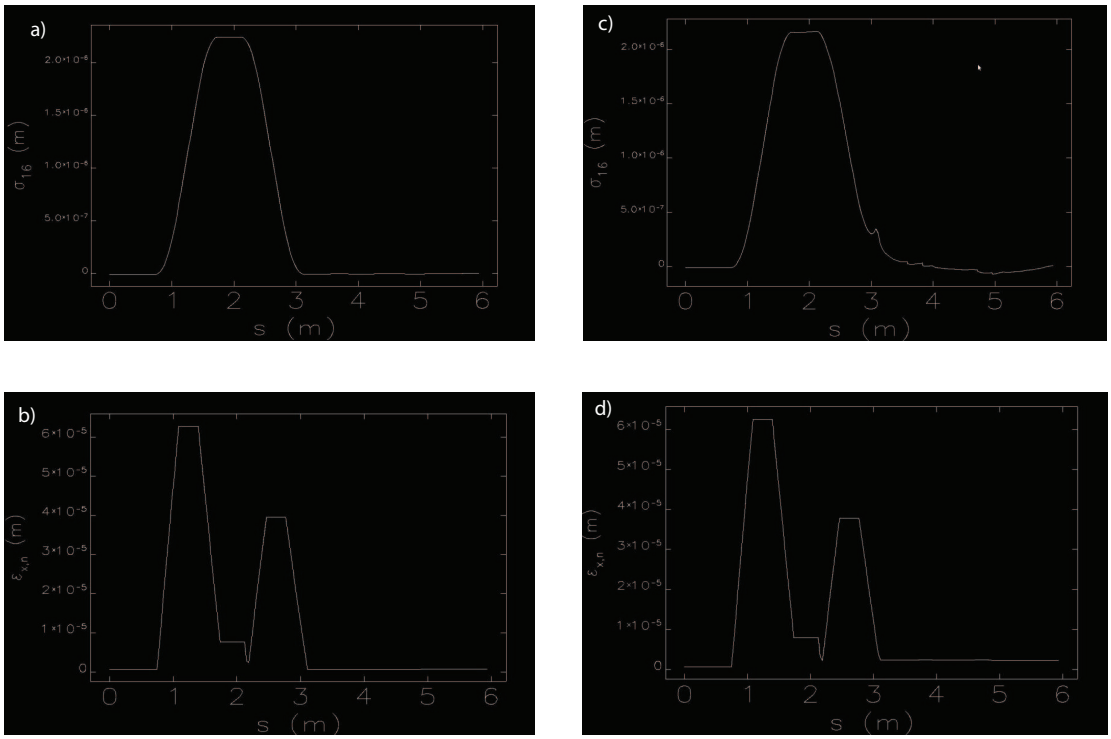


Figure 5.8: Dispersion and Normalized Horizontal Emittance Plots for Chicane in Elegant without and with Coherent Synchrotron Radiation (CSR). a),b) Dispersion and emittance respective plots without CSR. c),d) Dispersion and emittance respective plots with CSR.

The simulation results of the dispersion and horizontal normalized emittance plots can be seen in Figure 5.8. The left side of the figure shows the designed symmetric chicane where the dispersion cancels and there is no growth to the normalized horizontal emittance. The right side shows the effects of the CSR. The CSR creates nonlinearity in the longitudinal particle dynamics and poses a challenge to cancel the dispersion effectively, resulting in mixing between the x

and z trace planes and an increase in normalized emittance from the design 2 mm-mrad to 3 mm-mrad after the chicane with CSR effects included for a ∼ps electron beam compressed to ∼100 fs.

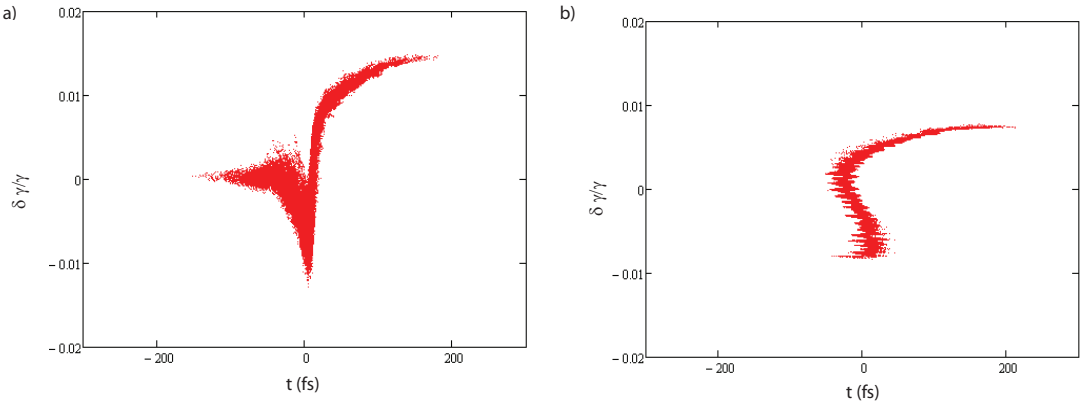


Figure 5.9: Longitudinal Phase Spaces after compression with (a) and without (b) CSR model.

#### 5.1.3.2 Final Focusing

The final focusing for the electron beam is accomplished by using two quadrupole triplets. The first triplet serves to expand the beam and to correct for any astigmatism. The second triplet focuses the beam to a minimum waist at the undulator center.

The final focusing for the laser occurs at a tank with an off axis parabola made from a dielectric substrate that is was coated for high reflectivity at 800 nm. The off axis parabola has a diameter of 40 mm and a focal length of 6.5 m. It is placed upstream of the center of the undulator by its focal length to ensure the minimum spot of the laser is at the center of the undulator as required by the IFEL dynamics design.

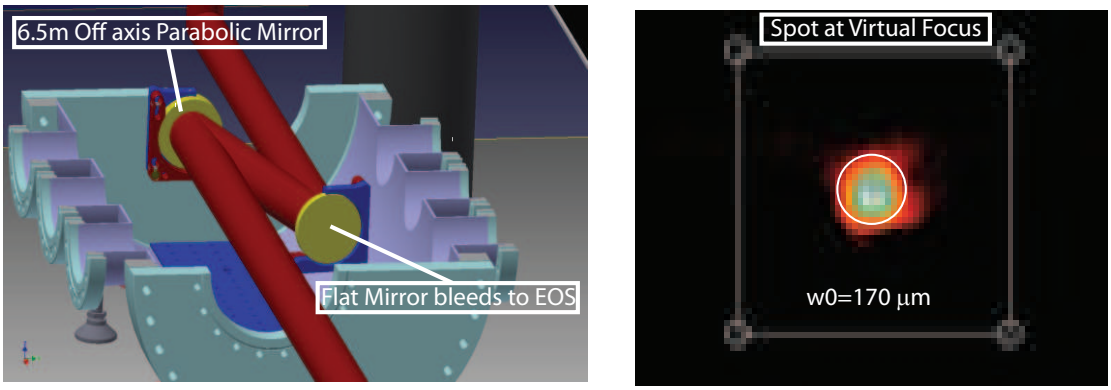


Figure 5.10: CAD Drawing of Focusing Chamber and Measured Spot at Virtual Focus.

#### 5.1.3.3 Undulator

The Kurchatov undulator was built for Neptune IFEL experiment. Being able to reuse an existing undulator greatly reduced the cost of the experiment. As can be seen in the left side of Figure 5.11, the magnetic field is tapered nonlinearly in both field intensity and period. This field map was used to model the undulator field in the "cbeam" and GPT simulations of the interaction.

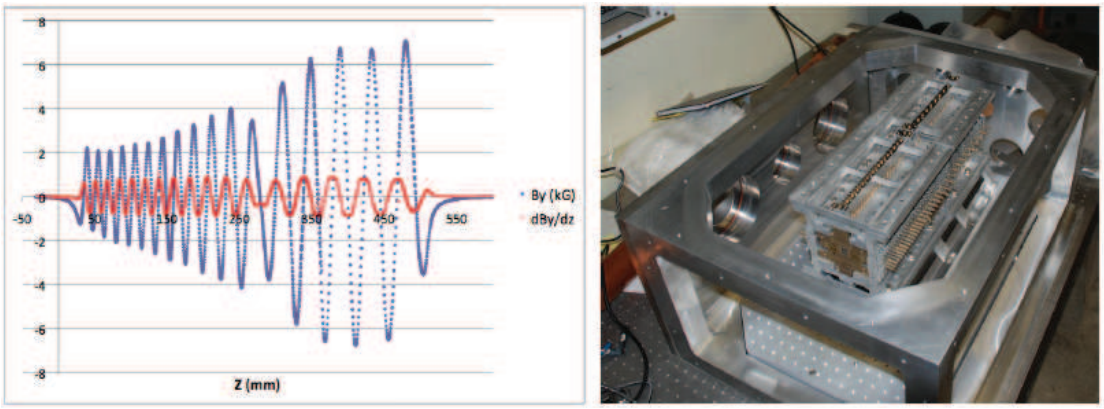


Figure 5.11: Undulator Field Map and Picture in Vacuum Chamber.

For the Neptune experiment, this undulator was designed to be tapered such that the IFEL resonance condition for the fundamental interaction was maintained from 14 MeV to 52 MeV for 10 $\mu$m wavelength $CO_2$ laser light. The undulator

period increases along the undulator for an initial value of 1.5 cm and a final period of 5.0 cm. The peak undulator strength parameter, $K$ is likewise tapered from 0.2 to 2.8. To achieve resonance with this undulator using 800 nm Ti:Sapphire light, the electron beam injection energy must be increased to 50 MeV resulting in an ending resonant energy of 200 MeV at the end of the undulator. As can be seen in the undulator field map, a trajectory phase shifter is located at the center of the undulator. This is designed to re-phase the periodic trajectory of the electron beam and compensate for the laser's Guoy phase shift that occurs at the waist of a Gaussian laser beam. The compensation is designed to correct for the shift associated with a diffraction limited Gaussian laser pulse with a 3.5 cm Rayleigh range.

### 5.1.4 Diagnostics

There is a suite of diagnostic required to determine spatial and temporal overlap of the electron beam and laser, as well as the longitudinal and transverse characteristics of the laser pulse and electron beam; these include the measurements of the electron beam bunch duration and transverse spot size, the characterization of the laser pulse and of th temporal and spatial overlap up to the measurement of the energy spectrum out of the IFEL accelerator.

#### 5.1.4.1 Electron beam Diagnostics

To measure the transverse profile of the electron beam as it propagates through the beamline, we used Yttrium-Aluminum Garnet (YAG) fluorescent screens. The images of the transverse profiles were acquired using CCD cameras looking at the screens.

DRZ fluorescent screens are used for the transverse profiles of the electron beam at the entrance, center, and exit of the undulator as well as the spectrometer

screen. The DRZ screens were used in these locations as they have a sensitivity that is about 50 % better when compared to standard Kodak Lanex and about five times greater sensitivity than that of the YAG crystals. The DRZ screens were purchased from MCI Optonix LLC [75].

The BLIS interferometer, discussed in Chapter 4, was used to spectrally analyze the coherent transition radiation generated at an aluminum foil located between the two sets of final focusing quadrupole magnets to make an electron bunch length diagnostic. The foil is placed at 45 degrees with respect to the beam propagation and the radiation passes through a THz transparent sapphire window. The radiation is then collimated by a metallic off-axis parabolic mirror located its focal length from the foil, and the CTR signal is propagated to the BLIS. The BLIS model we used did not have the option of a second detector to normalize the shot-to-shot fluctuations in CTR energy, so we used the same technique discussed in Chapter 4 in which we sampled several shots for a given delay and averaged. The model we used to fit the CTR signal was a beam with a longitudinal Gaussian profile with a low frequency spectral cut due to diffraction [76]. The RMS bunch length was measured to be $\sigma_t = 200$ fs after the chicane compression at when operating with a charge of (100 $\pm$ 10) pC.

#### 5.1.4.2 Laser Diagnostics

Because the laser's transverse mode quality can affect the field experienced by the electron beam during the IFEL interaction, diagnosis of the mode quality, spot size at the waist, and longitudinal position of the waist are all necessary to properly ensure a sufficient laser field interacts with the electron beam to accelerate the beam.

A Rayleigh range measurement was set up by pumping the main amplifier "off-time", i.e. by delaying the pump laser by 100 ns so that the seed laser propagates

without gain. This allows the laser pulses to propagate through the medium without amplification but including the correct thermal effects to the index of refraction in the lasing medium which act to focus effect on the laser pulse as if it were being amplified. The laser is then propagated through the compressor and beamline up to a meter before the undulator where it is brought out of the beamline and sent to a camera on a delay stage with ND filtering.

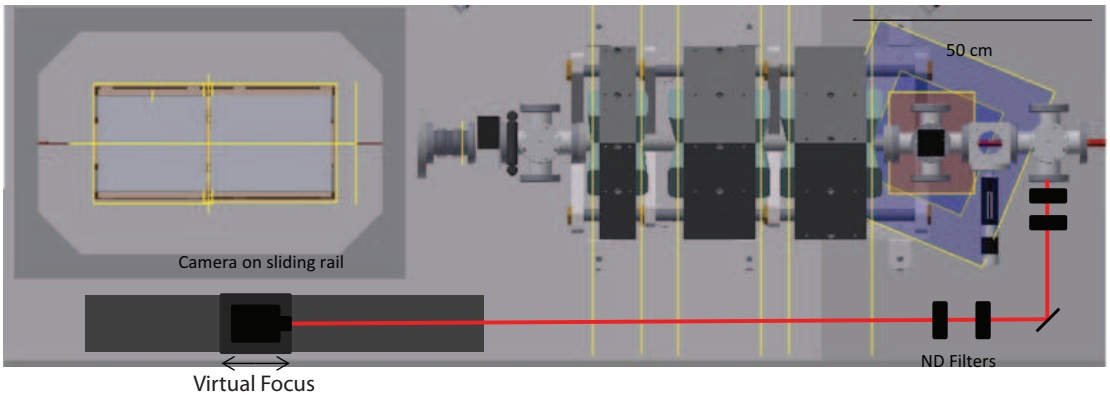


Figure 5.12: Setup for Rayleigh Range Measurement. A neutral density filtered camera on a sliding rail passes through the virtual focus of the laser and records images of the transverse profile.

This camera sits at a virtual focus, set at an equal distance as the center of the undulator from the off axis parabolic mirror. The camera is then scanned at several points moving away from this virtual focus, measuring the waist parameter, $w$ defined as the $1/e^2$ intensity radius of the transverse profile, at each point. Using these values we can fit to the model for a Gaussian beam traveling through a waist which gives,

$$w(z) = w_0\sqrt{1 + \left(\frac{z}{z_r}\right)^2} \tag{5.3}$$

where $w_0$ is the waist parameter at the focus, $z_r$ is Rayleigh length(range) defined by $z_r = \pi w_0^2/\lambda$. For a laser profile with a distribution other than diffraction limited Gaussian beam the divergence angle will go like $\theta = M^2\lambda/(\pi w_0)$ [77]. $M^2$

is a quality parameter that is equal to unity for a diffraction limited Gaussian and greater than one for other profiles.

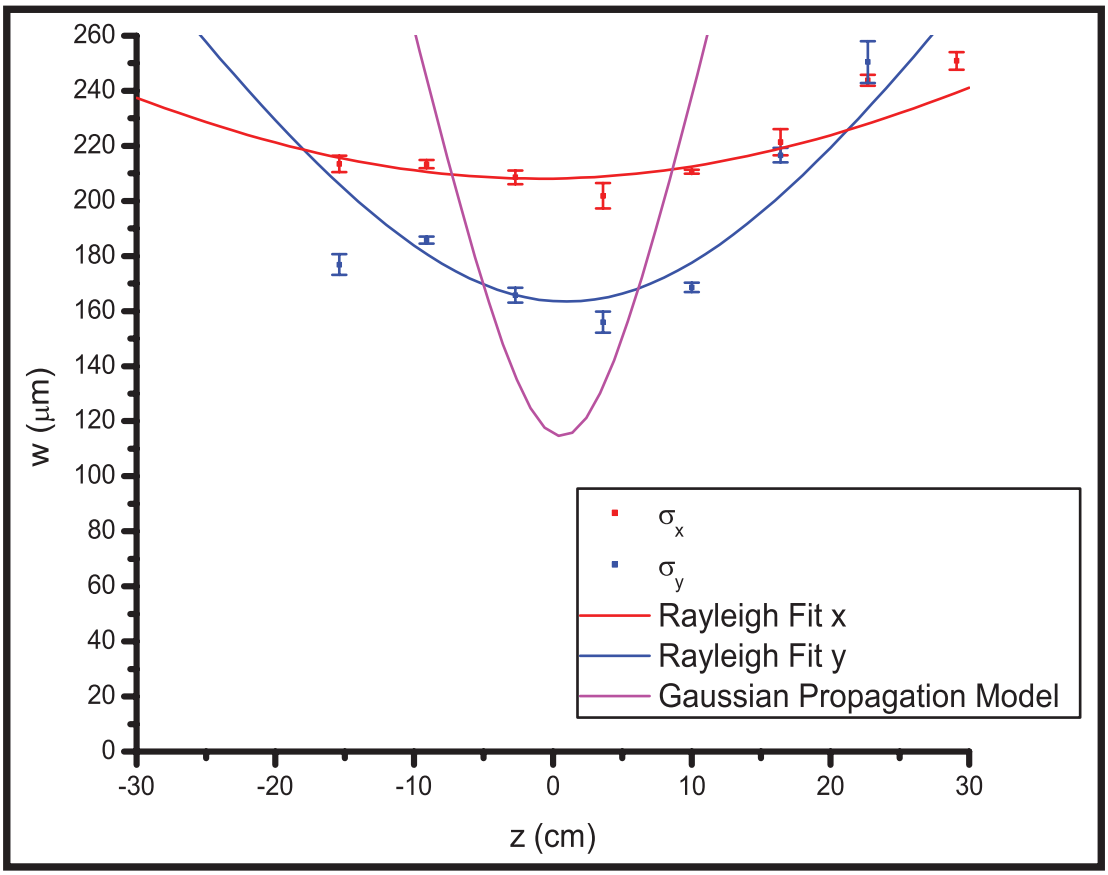


Figure 5.13: Rayleigh Range Measurements.

For an distribution with a $M^2 > 1$, the waist can be written as

$$w(z) = w_0\sqrt{1 + M^2\left(\frac{z}{z_r}\right)^2} \tag{5.4}$$

indicating that for a given $w_0$ the beam will diffract faster, resulting in an increased spot size for a given longitudinal distance away from the focus.

The results of the Rayleigh range measurement are seen in Figure 5.13. There is some asymmetry between x and y and the minimum spot size does not reach the predicted $w_0$ of 100 $\mu$m. The fitted values are shown in Table 5.2 and are compared to a design Gaussian model.

| Rayleigh Range Measurements | | | |
|---|---|---|---|
| Parameter | Measured X | Measured Y | Gaussian Model |
| $w_0$ | 200 $\mu$m | 160 $\mu$m | 100 $\mu$m |
| $z_{Rayleigh}$ | 7 cm | 12 cm | 3.5 cm |
| $M^2$ | 1.7 | 1.4 | 1 |

Table 5.2: Transverse Laser Properties

The laser profile is clearly non-Gaussian, and given the OAP with a 6.5 m focus, has a large spot size and longer Rayleigh range. This lowers the intensity by nearly a factor of two from the design value at the waist.

As a check to the off-time filtering method, we ran the amplifier at full power and used two wedges, one located at the output of the main amplifier and another at the last turn before the virtual focus, to verify the spot size and location of the waist on the virtual focus.

A Coherent EnergyMax pyroelectric Sensor and LabMax [78] energy meter was used to measure the laser pulse energy offline, with checks performed at the output of the amplifier and at the end of the electron beamline where the laser exits the system (when the electron beam is not in use). The laser energy before after the main amplifier before the compressor was measured to be 700 mJ with a 5% RMS fluctuation, while at the the exit of the beamline it was measured to be 500 mJ with a 5 % RMS fluctuation.

#### 5.1.4.3 Electron Beam Spectrometer

The results of the interaction are a modulation on the electron beam energy distribution that is measured by use of an electron spectrometer. A picture and path diagram of the electron spectrometer can be seen in Figure 5.14. For the purposes of our experiment we needed to be able to measure the electron beam's energy over a large dynamic range of 50 MeV to 200 MeV. An magnetic dipole

was utilized to serve this purpose. Additional side coils were added to allow the magnetic field inside the gap to reach 4 kGauss. To view the entire dynamic range in a single image we chose to place a long DRZ fluorescent screen on a pop-in directly inside a custom spectrometer vacuum tank that was designed at LLNL and built at the UCLA machine shop.

The spectrometer was designed assuming that a portion of the electron beam would be accelerated to 200 MeV. At full amplitude, the dipole would impart a 14 degree angle change, then the beam would further propagate to a set of quadrupole magnets and a beam dump. The pop-in screen and the computed paths for various energies can be seen on the right image of Figure 5.14.

A telescope consisting of an objective lens with a focal length of 5 cm and a compound lens system imaged the fluorescent screen on to a (CCD) camera so that the entire fluorescent screen, and hence the dynamic energy range of the spectrometer, could be captured in a single image.

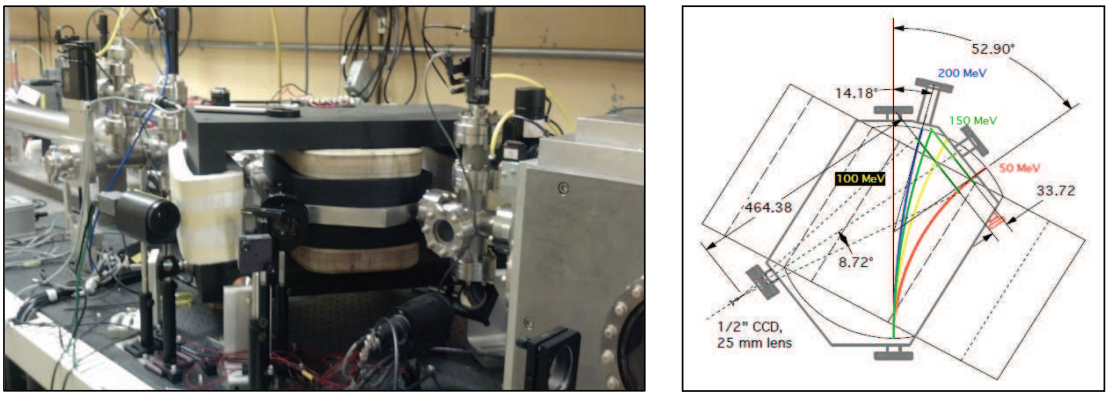


Figure 5.14: Spectrometer picture and Diagram

Typically with electron spectrometers a small angle approximation can be used so that the calibration is linear over the energy range of interest. In our case, however, the large energy range did not allow for a small angle approximation, and in the calibration we could not neglect the nonlinearity.

The calibration of energy to pixels of the spectrometer image can be seen in

Figure 5.15. This calibration was performed by first cross-correlating the magnetic field that the beam experiences at the center of the magnet with the fringe field that we can measure while the beam is present using two hall probes. The electron beam was then propagated for a fixed energy while varying the magnetic field. This relation is described by

$$p = eBR \tag{5.5}$$

where $p$ is the momentum of the electron beam, $e$ is the charge, $B$ is the magnetic field intensity and $R$ is the radius of curvature of the trajectory. By using a fixed energy electron beam and the magnetic field intensity changes the radius of curvature, which results in different intersection points on the fluorescent screen. We then fix the magnetic field intensity at a set value and calculate the momenta required to obtain the radii of curvature corresponding to the different positions on the spectrometer screen.

The result, seen in Figure 5.15 was compared to an analytical model which assumed an input particle momentum and magnetic field then computed the horizontal intercept of the particle trajectory with the fluorescent screen with one free parameter, the location of the left side of the camera's field of vision with respect to the edge of the fluorescent screen. This analytical model is the smooth curve seen in Figure 5.15. The two are in reasonably good agreement.

One minor complication with the calculation of the electron beam trajectory in the spectrometer is to properly account for the fringe magnetic field. To achieve consistency between the analytical model and the electron beam based empirical calibration, we used effective length obtained by measuring the fringe field at the 5 Gauss level with a Hall probe. The field was then numerically integrated and an effective length was determined for the magnetic field of the spectrometer. As a check the map was placed in a particle tracer and the trajectories were

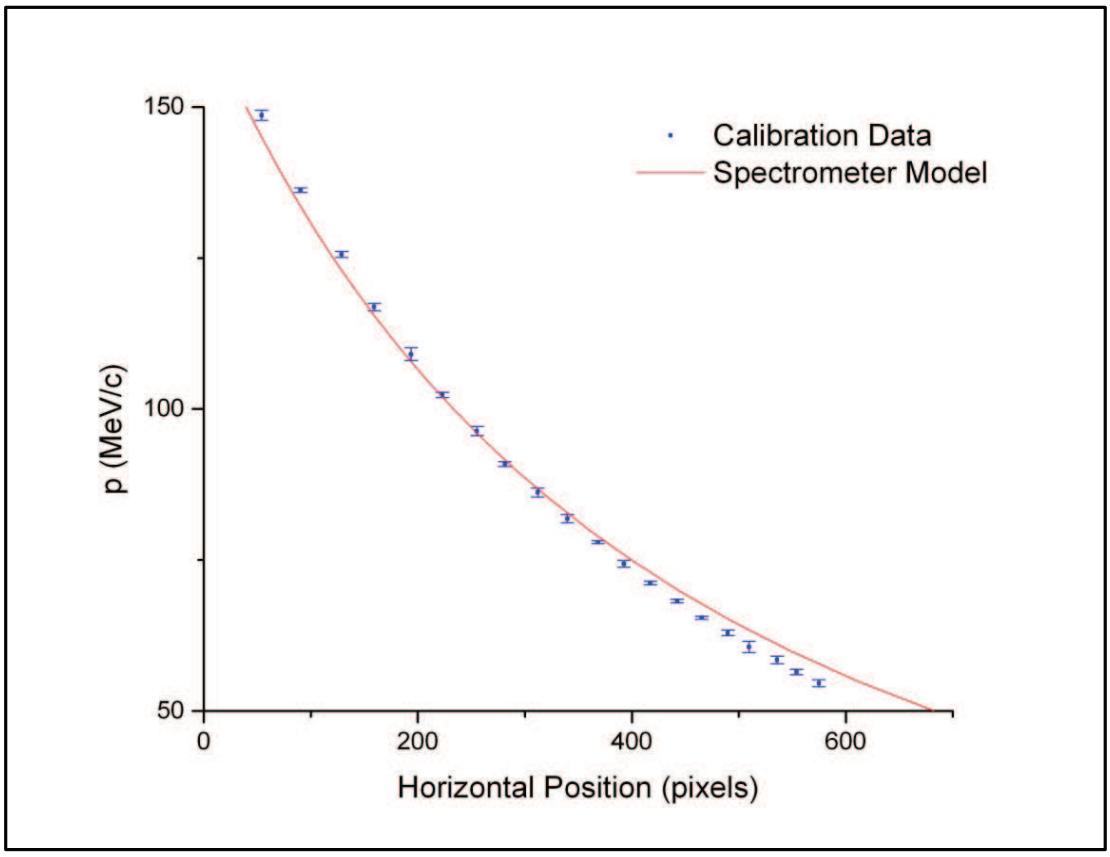


Figure 5.15: Spectrometer Calibration Curve. The data points are an empirically derived calibration while the solid curve is the results of an Analytical model.

determined precisely. The effective length dipole of constant magnetic field was consistent with the particle tracing model to within 1 % of the intercept position on the fluorescent screen.

#### 5.1.4.4 Temporal Overlap

The temporal overlap between the interaction laser and the electron beam is obtained by varying the relative time-of-arrival through use of an optical delay line. The length of the delay line is set to match the path length of the photocathode drive arm after the beamsplitter, plus the length of the electron beamline up to the center of the undulator minus the remaining distance of the interaction laser

arm after the delay line.

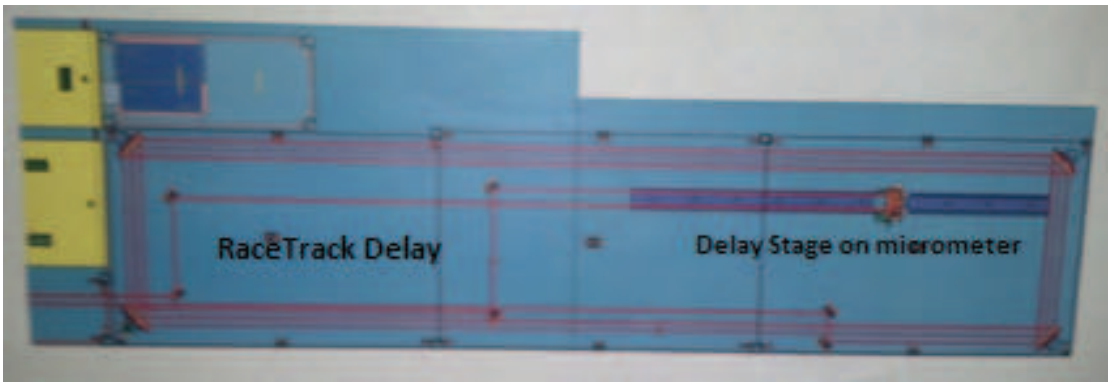


Figure 5.16: Diagram of Race Track Delay Line for the Interaction Laser.

The absolute temporal overlap was measured to the level of 2 ps using a streak camera. A foil between the two final focus triplets is inserted in order to obtain an optical signal corresponding to the electron beam from the transition radiation of the electrons. The foil has optical quality flatness and is also used to reflect the drive laser to the streak camera. The interaction laser is heavily filtered using OD 7 filters and pumping off time in the main amplifier. This reduces the pulse energy from 20 mJ to sub nJ levels so that it does not saturate the streak camera and is on the same scale as the collected optical transition radiation (OTR). Both the OTR and the filtered laser are then propagated out of the beamline and into the streak camera. The delay line is then adjusted until the OTR and laser pulse are overlapped on the streak camera.

## 5.2 Experimental Results and Analytical Discussion

The measurement of the modulated spectrum and the time of arrival correlated are discussed in the following sections.

### 5.2.1 Accelerated Electron Beam Spectrum

Initially, the ideal case was explored by injecting the electron beam at an energy 50 MeV with a design output energy of 200 MeV as can be seen in the red design acceleration curve seen in Figure 5.18. This, however, resulted in no observable energy modulation of the electron beam by the IFEL process due a lack of capture of the electron beam at the beginning of the undulator. This lack of capture is primarily due to the lower than design laser intensity caused by the higher order spatial mode in the transverse profile of the laser.

We then decided to increase the injection energy of the electron beam, effectively injecting the beam further into the undulator since the interaction is minimal until the resonance curve is at the injection energy of 57 MeV, and we were able to observe energy modulation. An example of this on the left side of Figure 5.17. The observed energy modulation accelerated a small fraction ($< 1\%$) of the beam from 57 MeV to 73 MeV.

The experiment ran at 10 Hz, which is the repetition rate of the laser. The data collection, however, based upon Gig-E cameras, limited the data collection to 2 Hz. The repeatability of the results was fairly low, where energy modulation is observed approximately 3 shots out of 10. This is due to both time of arrival and pointing jitter corresponding to rf phase fluctuations in the electron beam gun and accelerating sections, particularly in the section used to chirp the electron beam for compression in the chicane.

In an attempt to observe a larger accelerating gradient, we then injected at the largest energy that would be allowed by the magnetic fields of the dipoles in the chicane - 77 MeV. We observed acceleration from 77 MeV to 120 MeV.

The two cases were simulated using GPT using the achievable laser profile and comparing it to the the ideal case.

The simulated energy gain profiles of the highest observable electrons are

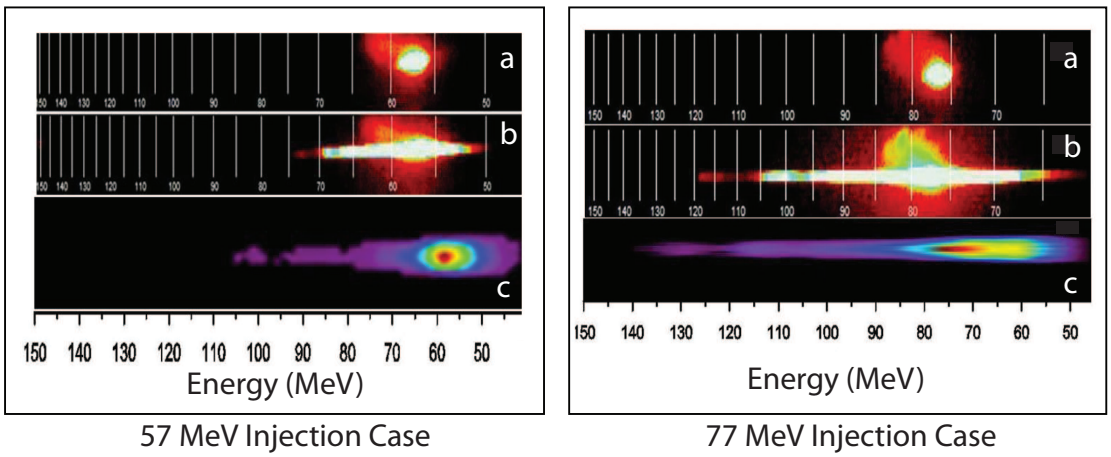


Figure 5.17: Electron Beam Spectrum Results. a) No laser b) Experimental Measured Spectrum c) GPT Simulated Spectrum

shown in Figure 5.18. The red curve describes the energy gain set by the tapering gradient of the undulator while the blue and green curves represent the simulated gradients corresponding to the measured best shots observed in the experiment for injection energies of 57 MeV and 77 MeV. Because we injected at energies higher than the resonant energy at the beginning of the undulator, the resonance does not begin until around the intersection of design acceleration curve.

For the 77 MeV case we saw acceleration to a final energy of 120 MeV, but according to the simulation most of the acceleration took place from 20 cm to 35 cm, resulting in a peak accelerating gradient of 200 MeV per meter. The average acceleration over the resonant region was approximately 130 MeV per meter.

Injection of the electrons into the accelerator at an energy above that of the resonant energy at the entrance of the undulator leads to phase area displacement as described by Kroll. [79]. In phase area displacement, electrons move along the outside of the bucket resulting in an energy modulation amplitude of the electron beam that is on the order of the bucket height. While this may account for some

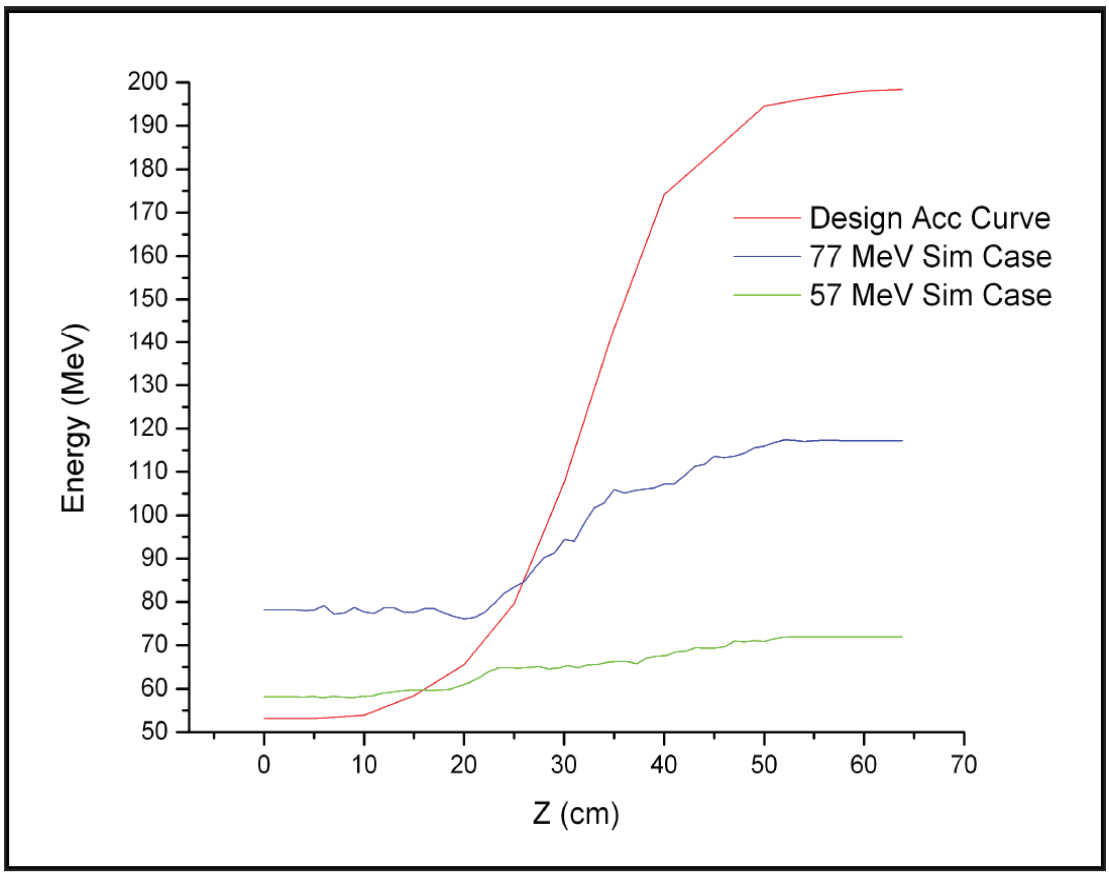


Figure 5.18: Energy gain profiles. The maximum energy gain along the undulator from simulated cases consistent with the measured cases.

of the energy modulation experienced by the electron beam, the 40 MeV gain observed at an injection energy of 77 MeV can not explained by this model, as the approximate bucket height is 7 MeV at injection. The phase space separatrix concept derives from a one dimensional Hamilitonian approximation of the beam dynamics. In reality there are many effects such as varying resonant phase and strong tapering that allow for particles 'crossing the separatrix' and getting trapped into the bucket, resulting in acceleration to the final 120 MeV energy.

### 5.2.2 Temporal Overlap Study

Because the laser pulse is on the same scale as the relative slippage between the electrons and the laser pulse in the undulator, the amplitude of the ponderomotive bucket responsible for the beam acceleration evolves due to the electron slipping with respect to the envelope of the pulse. With the electron beam's and laser pulse's lengths on the same scale as the slippage (i.e. 100 fs time scale), the time of arrival jitter between the electron and laser beams can have a significant effect on the performance of the accelerator. Due to aged RF sections with significant phase jitter and instability, the time of arrival jitter of the electron beam was estimated to be on the order of 1 ps. To successfully characterize the temporal overlap, the electron beam's time of arrival with respect to the laser must be determined for each shot. Electro-optic sampling provides for a diagnostic that can accomplish this measurement.

This diagnostic in fact can provide two useful pieces of information. If the delay line is fixed we can measure the time of arrival jitter of the electron beam with respect to the interaction laser. The second is the relative timestamping the IFEL energy modulated electron beam spectra by taking coincident measurements of the spectrometer and EOS diagnostic.

#### 5.2.2.1 Electro-optic Sampling Based Time of Arrival Measurement

In electro-optic sampling a crystal is used to sample the near field of the electron beam which induces a birefringence in the crystal via the Pockels effect. A linearly polarized optical laser is used to probe this index change, resulting in a polarization shift that can be then detected by an analyzing polarizer. In our case of interest the low frequency fields are the near fields of the relativistic electron beam passing by the crystal.

A 90 degree crossing geometery spatially encoding the time stamping based

on EOS effect was developed by C. Scoby [80] for timestamping of pump-probe ultrafast electron diffraction experiments.

The induced phase delay between the fast and slow axes in the crystal for a laser pulse propagating along the [1,0,0] plane of a "Zinc Blende" (i.e. ZnTe, GaP, etc.) is

$$\Gamma = \frac{\omega d}{2c} n_0^3 r_{41} E_{THz} \sqrt{1 + 3\cos^2 \alpha} \tag{5.6}$$

where $\omega$ is the angular frequency of the laser pulse, $d$ is the length of the crystal, $n_0$ is the zero order index of refraction for the laser pulse, $r_{41}$ is the Pockels coefficient for the crystal, $E_{THz}$ is the magnitude of the electric field of the THz scale field, or near field of the relativistic electron beam, and $\alpha$ is the angle of the electric field with respect to the [-1,1,0] axis of the crystal.

This phase retardation causes a rotation in the polarization of a linear polarized laser pulse with its electric field direction between the induced slow and fast axes. If a crossed polarizer configuration is used, where the analyzer is fixed at 90 degrees with respect to the initial polarization, the transmitted intensity to the CCD camera will be

$$I_{detector} = I_0 \sin^2(\frac{\Gamma}{2}) \tag{5.7}$$

In this configuration we see that for small $\Gamma$ we get an intensity that is proportional to $\Gamma^2$.

A figure of this setup applied to the LLNL beamline is shown in Figure 5.19. The main interaction laser is focused by the OAP in the focusing chamber then reflects off of a flat mirror located immediately after it. This mirror's coating allows approximately a tenth of a percent of the laser energy to be transmitted through the four inch optic. The core of this beam leakage is then reflected by a one inch mirror to the EOS optical transport beamline.

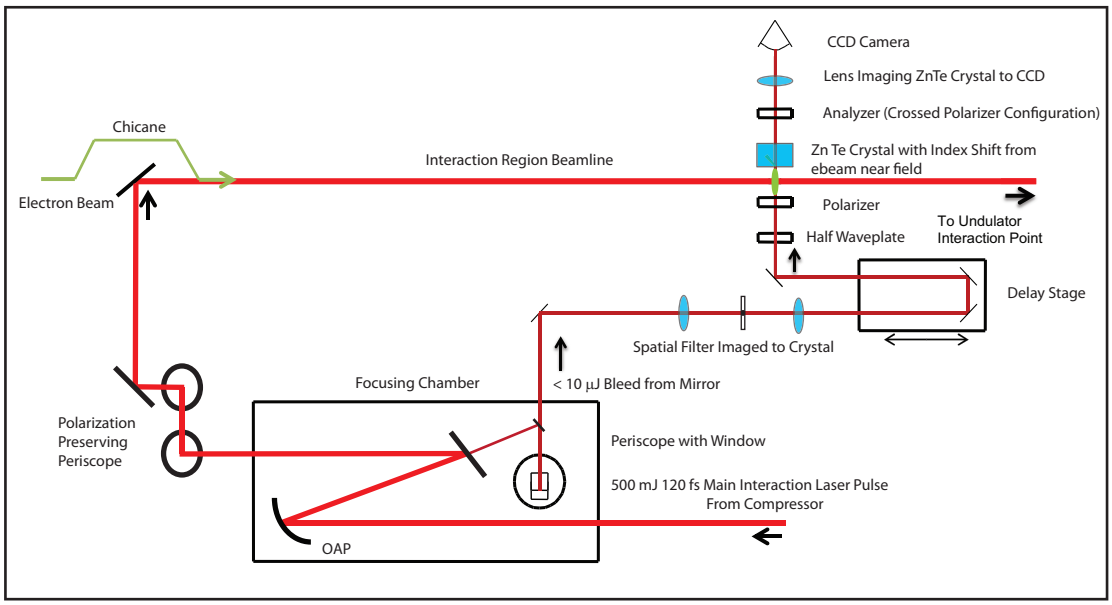


Figure 5.19: Diagram of Electro-Optic Sampling Timing Diagnostic

Because the mirror only intercepts a small portion of the larger laser beam bleeding through, the reflected laser pulse has a very poor spatial quality. A spatial filter was therefore designed using two positive lenses and a 300 $\mu$m pinhole. The telescope was chosen so that the overfilled spatial filter is imaged onto the ZnTe crystal. Once the polarization shift has occurred within the ZnTe, the plane of the crystal is imaged to the CCD. The spatial filtering results in a very uniform background, an important aspect of 90-degree spatially encoded EOS.

For coincident EOS and IFEL measurements to be captured, the electron beam must be as close to the crystal as possible. Indeed Scoby et al measured 100 kV/m with the electron 1 mm from the surface of the crystal. In the LLNL case, however, the separation between the crystal edge and the electron beam axis must be larger due to the main interaction laser co-propagating with the electron beam under the crystal. The scattering off of the crystal from the tail of the 500 mJ pulse is sufficient to saturate the camera and therefore the crystal must be kept sufficiently far away to prevent saturation of the image and damage of the crystal.

With the crystal placed 50 cm upstream from the waist of the laser, with the

assumption that the laser profile is approximately Gaussian with a spot size at the waist of $w_0 = 150$ $\mu$m and a Rayleigh range of 7 cm , the intensity of the laser at this point at 1 mm is 20 TW/cm$^2$, far beyond the damage threshold of the crystal. We must therefore move the crystal further away from the previously demonstrated 1 mm distance from the electron beam. A safe threshold for the intensity at the crystal's surface is less than 10 W/cm$^2$. According to the propagation model, a distance of 5 mm is required, resulting in an intensity of 5 W/cm$^2$.

For a relativistic Gaussian electron beam, the radial near electric field a distance r away from the beam is

$$E = \frac{q}{(2\pi)^{3/2}\epsilon_0 r c \sigma_t} \tag{5.8}$$

For a 100 pC 200 fs electron beam this gives us a radial field of 1 MV/m a distance of 5 mm from the center of the electron beam. For this field we expect a phase retardation on the scale of hundreds of degrees from Equation 5.6 if we use the full thickness of the crystal.

The measured phase retardation, however, was determined to be $\sim 7\%$. This phase retardation was determined by first finding the initial intensity value, $I_0$ in Equation 5.7 with the polarizers in an uncrossed state by measuring the values on a 12 bit CCD camera with calibratied neutral density filters applied. The polarizers are then configured in a crossed state and the intensity values are again measured during the experiment. Using the compared intensities in Equation 5.7, the phase retardation is determined.

The apparent discrepancy between the measured and expected phase retardation can be explained by the use of the effective length of the crystal that contributes in Equation 5.6. This length is not the full thickness of the crystal but a thinner effective length that the laser pulse probes. As the laser pulse moves

through the crystal, the birefringence is being induced on the same timescale as the traversal times of both the laser and the near field through the crystal. For a given transverse slice of the crystal with respect to the propagation of the laser pulse, then, only a small length estimated to be on the order of 100 $\mu$m of the polarized crystal is sampled by the probe laser pulse.

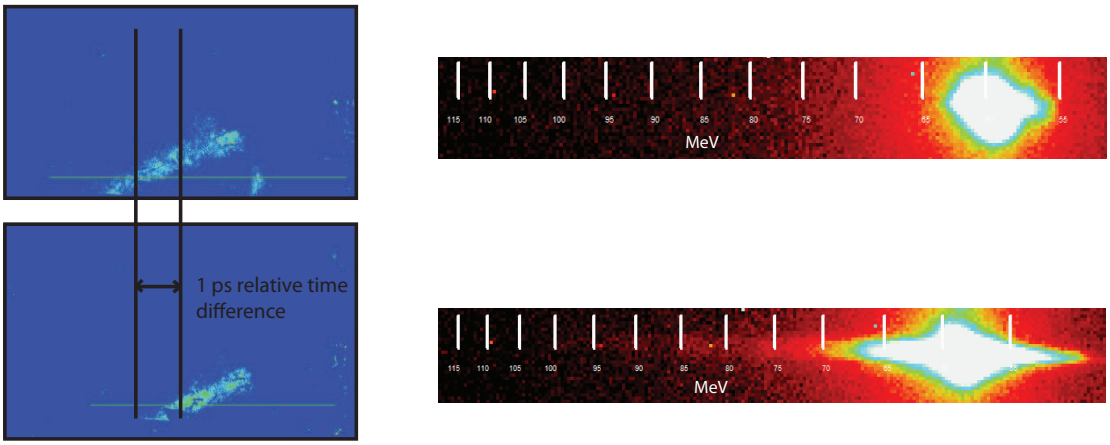


Figure 5.20: Sample Coincident EOS and measured IFEL Spectra

Sample shots of the EOS measurement can be seen in Figure 5.20. The coincident images show calibrated spectra from the IFEL interaction as well as the near field maps captured by the EOS measurement. To determine the relative time of arrival, a lineout near the edge of the crystal is used and the peak of the resulting distribution is determined. The meaningful quantity is the relative shift of the peak of the distribution in the lineout. For each shot this peak is determined and then recorded along with the maximum energy modulation measured by the spectrometer.

The image analysis is performed by first sampling the backgrounds. For the spectrometer this is a sample image without the laser to guarantee no IFEL interaction while with the EOS measurement the background is determined by sampling without the electron beam to induce the polarization shift. Several of these backgrounds images are sampled then the average and RMS values are taken by

pixel values. For every measurement shot, a filter is applied by zeroing any pixel with an intensity value less than two standard deviations above the mean of the background pixels. This results in high contrast signals in which the peak of the distribution and its relative position are well determined. The measurement gives a 60 fs per pixel resolution for the relative position of the peak of the EOS signal.

The energy modulation by the spectrometer is determined by applying the same filtering technique as the EOS image analysis but instead of searching for a peak signal from a lineout we are interested in the maximum energy modulation from the initial center of the electron beam on the spectrometer with no energy modulation. To accomplish this, after the background subtraction is applied, a loop is performed from the maximum energy values to minimum energy values searching for five contiguous non zero value, the first value is determined to be the maximum energy modulation associated with the distribution.

The results of the time of arrival study can be seen in Figure 5.21. Over two-hundred correlated images were examined and binned into 200 fs bins. The points and error bars were determined by averaging over values in each bin, taking the RMS and dividing by the square root of the number of values in each respective bin. Due to the pointing jitter of the electron beam, for each time of arrival there are several zero modulation values even around the peak of the correlated region, therefore binning was required and taking the average value was necessary.

A simple cross correlation model was applied for Gaussian models between the electron beam and the laser pulses with the values of 120 fs FWHM and 240 fs RMS, respectively. This model was found to be consistent with the envelope of the overlap data.

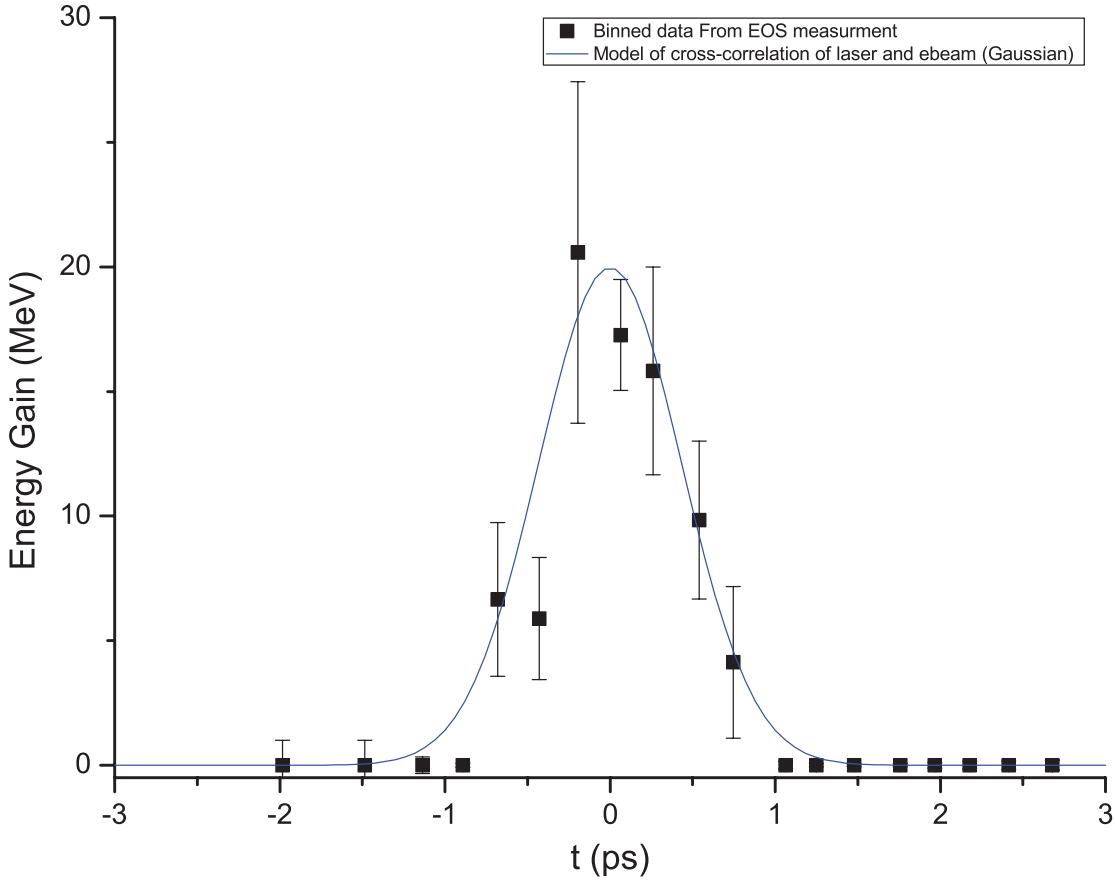


Figure 5.21: Results of Time of Arrival Study. Over 200 correlated relative time of arrival and energy modulation were sampled and binned to provide modulation time of arrival overlap profile.

## 5.3 Conclusions

The IFEL interaction with this undulator and laser resulted in 40 MeV energy gain over approximately 25 cm, resulting in an average accelerator gradient of ∼150 MeV/m and a peak gradient. of 200 MeV/m.

Acceleration with a short pulse using CPA Ti:Sapphire technology was investigated in which the laser pulse length was of the same scale as the electron beam slippage with respect to the laser. The overlap was found to agree with a Gaussian cross correlation model that with the measured pulse length values for the laser

and electron beams.

# References


[1] A. Fassò, K. Goebel, M. Höfert, G. Rau, H. Schönbacher, G. Stevenson, A. Sullivan, W. Swanson, and J. Tuyn, "Radiation problems in the design of the large electron-positron collider (lep)," tech. rep., European Organization for Nuclear Research, Geneva (Switzerland), 1984.

[2] K. Yokoya and S. Yamashita, "International linear collider," *Nippon Butsuri Gakkai-Shi*, vol. 61, no. 4, pp. 240–247, 2006.

[3] M. Battaglia, A. de Roeck, J. R. Ellis, and D. Schulte, *Physics at the CLIC Multi-TeV Linear Collider : report of the CLIC Physics Working Group.* Geneva: CERN, 2004.

[4] J. Arthur *et al.*, "{Linac Coherent Light Source (LCLS)} conceptual design report," *SLAC-R-593*, 2002.

[5] K. Tiedtke, A. Azima, N. Von Bargen, L. Bittner, S. Bonfigt, S. Düsterer, B. Faatz, U. Frühling, M. Gensch, C. Gerth, *et al.*, "The soft x-ray free-electron laser flash at desy: beamlines, diagnostics and end-stations," *New journal of physics*, vol. 11, no. 2, p. 023029, 2009.

[6] Y. Saitoh, H. Kimura, Y. Suzuki, T. Nakatani, T. Matsushita, T. Muro, T. Miyahara, M. Fujisawa, K. Soda, S. Ueda, *et al.*, "Performance of a very high resolution soft x-ray beamline bl25su with a twin-helical undulator at spring-8," *Review of Scientific Instruments*, vol. 71, no. 9, pp. 3254–3259, 2000.

[7] R. Ganter, "Swissfel-conceptual design report," tech. rep., Paul Scherrer Institute (PSI), Villigen (Switzerland). Funding organisation: Paul Scherrer Institute (PSI), Villigen (Switzerland), 2010.

[8] J. Jackson, *Classical Electrodynamics*. Wiley,New York, 3rd ed., 1999.

[9] C. Kunz, "Synchrotron radiation," 1974.

[10] R. Marsh, S. Anderson, T. Chu, C. Ebbers, D. Gibson, F. Hartemann, C. Barty, C. Adolphsen, E. Jongewaard, S. Tantawi, *et al.*, "Advanced x-band test accelerator for high brightness electron and gamma ray beams," *Proc. IPAC10, Kyoto, Japan*, 2010.

[11] F. Hartemann, F. Albert, G. Anderson, S. Anderson, A. Bayramian, S. Betts, T. Chu, R. Cross, C. Ebbers, S. Fisher, *et al.*, "Overview of mono-energetic gamma-ray sources & applications," in *Conf. Proc. C*, vol. 100523, 2010.

[12] "Facet-ii proposal."

[13] I. Blumenfeld, C. E. Clayton, F.-J. Decker, M. J. Hogan, C. Huang, R. Ischebeck, R. Iverson, C. Joshi, T. Katsouleas, N. Kirby, *et al.*, "Energy doubling of 42 gev electrons in a metre-scale plasma wakefield accelerator," *Nature*, vol. 445, no. 7129, pp. 741–744, 2007.

[14] W. Leemans, B. Nagler, A. Gonsalves, C. Toth, K. Nakamura, C. Geddes, E. Esarey, C. Schroeder, and S. Hooker, "Gev electron beams from a centimetre-scale accelerator," *Nature physics*, vol. 2, no. 10, pp. 696–699, 2006.

[15] E. Peralta, K. Soong, R. England, E. Colby, Z. Wu, B. Montazeri, C. McGuinness, J. McNeur, K. Leedle, D. Walz, *et al.*, "Demonstration of electron acceleration in a laser-driven dielectric microstructure," *Nature*, vol. 503, no. 7474, pp. 91–94, 2013.

[16] N. Thompson and B. McNeil, "Mode locking in a free-electron laser amplifier," *Physical review letters*, vol. 100, no. 20, p. 203901, 2008.

[17] R. Palmer *J. Applied Physics*, vol. 43:3014, 1972.

[18] E. D. Courant, C. Pellegrini, and W. Zakowicz, "High-energy inverse free-electron-laser accelerator," *Phys. Rev. A*, vol. 32, pp. 2813–2823, Nov 1985.

[19] I. Wernick and T. C. Marshall, "Experimental test of the inverse free-electron-laser accelerator principle," *Phys. Rev. A*, vol. 46, pp. 3566–3568, Sep 1992.

[20] A. Fisher, J. Gallardo, A. Van Steenbergen, S. Ulc, M. Woodle, J. Sandweiss, and J.-M. Fang, "An inverse free-electron-laser accelerator," in *Particle Accelerator Conference, 1993., Proceedings of the 1993*, pp. 2578–2580 vol.4, May 1993.

[21] A. van Steenbergen, J. Gallardo, J. Sandweiss, and J.-M. Fang, "Observation of energy gain at the bnl inverse free-electron-laser accelerator," *Phys. Rev. Lett.*, vol. 77, pp. 2690–2693, Sep 1996.

[22] Y. Liu, X. J. Wang, D. B. Cline, M. Babzien, J. M. Fang, J. Gallardo, K. Kusche, I. Pogorelsky, J. Skaritka, and A. van Steenbergen, "Experimental observation of femtosecond electron beam microbunching by inverse free-electron-laser acceleration," *Phys. Rev. Lett.*, vol. 80, pp. 4418–4421, May 1998.

[23] R. B. Yoder, T. C. Marshall, and J. L. Hirshfield, "Energy-gain measurements from a microwave inverse free-electron-laser accelerator," *Phys. Rev. Lett.*, vol. 86, pp. 1765–1768, Feb 2001.

[24] W. D. Kimura, A. van Steenbergen, M. Babzien, I. Ben-Zvi, L. P. Campbell, D. B. Cline, C. E. Dilley, J. C. Gallardo, S. C. Gottschalk, P. He, K. P.

Kusche, Y. Liu, R. H. Pantell, I. V. Pogorelsky, D. C. Quimby, J. Skaritka, L. C. Steinhauer, and V. Yakimenko, "First staging of two laser accelerators," *Phys. Rev. Lett.*, vol. 86, pp. 4041–4043, Apr 2001.

[25] W. Kimura, M. Babzien, I. Ben-Zvi, L. Campbell, D. Cline, C. Dilley, J. Gallardo, S. Gottschalk, K. Kusche, R. Pantell, *et al.*, "Demonstration of high-trapping efficiency and narrow energy spread in a laser-driven accelerator," *Physical review letters*, vol. 92, no. 5, p. 054801, 2004.

[26] P. Musumeci, S. Y. Tochitsky, S. Boucher, C. E. Clayton, A. Doyuran, R. J. England, C. Joshi, C. Pellegrini, J. E. Ralph, J. B. Rosenzweig, C. Sung, S. Tolmachev, G. Travish, A. A. Varfolomeev, A. A. Varfolomeev, T. Yarovoi, and R. B. Yoder, "High energy gain of trapped electrons in a tapered, diffraction-dominated inverse-free-electron laser," *Phys. Rev. Lett.*, vol. 94, p. 154801, Apr 2005.

[27] A. Varfolomeev, S. Tolmachev, T. Yarovoi, P. Musumeci, C. Pellegrini, and J. Rosenzweig, "An undulator with non-adiabatic tapering for the {IFEL} project," *Nuclear Instruments and Methods in Physics Research Section A: Accelerators, Spectrometers, Detectors and Associated Equipment*, vol. 483, no. 12, pp. 377 – 382, 2002. Proceedings of the 23rd International Free Electron Laser Confere nce and 8th {FEL} Users Workshop.

[28] J. D. et. al, "Private communication."

[29] S. Anderson, G. Anderson, S. Betts, S. Fisher, D. Gibson, A. Tremaine, S. Wu, J. Moody, and P. Musumeci, "The llnl/ucla high gradient inverse free electron laser accelerator," Proceedings of 2128 Particle Accelerator Conference, 2011.

[30] J. Moody, P. Musumeci, G. Anderson, S. Anderson, S. Betts, S. Fisher, D. Gibson, A. Tremaine, and S. Wu, "The llnl/ucla high gradient inverse free electron laser accelerator," *Energy*, vol. 70, p. 140, 2012.

[31] J. Moody, P. Musumeci, G. Anderson, S. Anderson, S. Betts, S. Fisher, D. Gibson, A. Tremaine, and S. Wu, "Results of the short pulse driven llnl/ucla ifel experiment,"

[32] D. R. Nicholson, *Introduction to plasma theory*. Cambridge Univ Press, 1983.

[33] I. Kapchinsky and V. Yladimirsky, "Limitations of proton beam current in a strong focusing linear accelerator associated with beam space charge," 1959.

[34] O. Luiten, S. Van der Geer, M. De Loos, F. Kiewiet, and M. Van Der Wiel, "How to realize uniform three-dimensional ellipsoidal electron bunches," *Physical review letters*, vol. 93, no. 9, p. 094802, 2004.

[35] L. Serafini, "Towards the x-ray free electron laser," AIP Conf. Proc. No. 413, 1997.

[36] P. Maine, D. Strickland, P. Bado, M. Pessot, and G. Mourou, "Generation of ultrahigh peak power pulses by chirped pulse amplification," *Quantum electronics, IEEE Journal of*, vol. 24, no. 2, pp. 398–403, 1988.

[37] P. Musumeci, J. Moody, and G. Gatti, "Ultrafast beam research at the pegasus laboratory," in *Particle Accelerator Conference, 2007. PAC. IEEE*, pp. 2751–2753, IEEE, 2007.

[38] C. Scoby, P. Musumeci, J. Moody, and M. Gutierrez, "Electro-optic sampling at 90 degree interaction geometry for time-of-arrival stamping of ultrafast relativistic electron diffraction," *Physical Review Special Topics-Accelerators and Beams*, vol. 13, no. 2, p. 022801, 2010.

[39] P. Musumeci, J. Moody, and C. Scoby, "Relativistic electron diffraction at the ucla pegasus photoinjector laboratory," *Ultramicroscopy*, vol. 108, no. 11, pp. 1450–1453, 2008.

[40] L. Serafini and J. B. Rosenzweig, "Envelope analysis of intense relativistic quasilaminar beams in rf photoinjectors: ma theory of emittance compensation," *Physical Review E*, vol. 55, no. 6, p. 7565, 1997.

[41] R. J. England, B. O'Shea, J. Rosenzweig, G. Travish, and D. Alesini, "X-band dipole mode deflecting cavity for the ucla neptune beamline," in *Particle Accelerator Conference, 2005. PAC 2005. Proceedings of the*, pp. 2627–2629, IEEE, 2005.

[42] K. Flottmann, S. Lidia, and P. Piot, "Recent improvements to the astra particle tracking code," *Lawrence Berkeley National Laboratory*, 2003.

[43] P. Musumeci, J. Moody, C. Scoby, M. Gutierrez, and T. Tran, "rf streak camera based ultrafast relativistic electron diffraction," *Review of Scientific Instruments*, vol. 80, no. 1, p. 013302, 2009.

[44] P. Woodward *J. Inst. Electr. Eng*, p. 1554, 1985.

[45] J. D. Lawson *IEEE Trans. Nucl. Sci.*, p. 4217, 1979.

[46] E. Esarey, P. Sprangle, and J. Krall, "Laser acceleration of electrons in vacuum," *Phys. Rev. E*, vol. 52, pp. 5443–5453, Nov 1995.

[47] E. Noether, "Invariant variation problems," *Transport Theory and Statistical Physics*, vol. 1, pp. 186–207, 1971.

[48] M. Santarsiero, D. Aiello, R. Borghi, and S. Vicalvi, "Focusing of axially symmetric flattened gaussian beams," *Journal of Modern Optics*, vol. 44, no. 3, pp. 633–650, 1997.

[49] P. Siegel, "Terahertz technology in biology and medicine," in *Microwave Symposium Digest, 2004 IEEE MTT-S International*, vol. 3, pp. 1575–1578 Vol.3, June 2004.

[50] J. F. Federici, B. Schulkin, F. Huang, D. Gary, R. Barat, F. Oliveira, and D. Zimdars, "Thz imaging and sensing for security applicationsexplosives, weapons and drugs," *Semiconductor Science and Technology*, vol. 20, no. 7, p. S266, 2005.

[51] J. Jackson, J. Bowen, G. Walker, J. Labaune, G. Mourou, M. Menu, and K. Fukunaga, "A survey of terahertz applications in cultural heritage conservation science," *Terahertz Science and Technology, IEEE Transactions on*, vol. 1, pp. 220–231, Sept 2011.

[52] J. Faist, F. Capasso, D. L. Sivco, C. Sirtori, A. L. Hutchinson, and A. Y. Cho, "Quantum cascade laser," *Science*, vol. 264, no. 5158, pp. 553–556, 1994.

[53] A. Yariv, *Quantum Electronics*. Wiley, third ed., 1989.

[54] J. Hebling, K.-L. Yeh, M. C. Hoffmann, B. Bartal, and K. A. Nelson, "Generation of high-power terahertz pulses by tilted-pulse-front excitation and their application possibilities," *JOSA B*, vol. 25, no. 7, pp. B6–B19, 2008.

[55] K.-L. Yeh, *The generation of high field terahertz radiation and its application in terahertz nonlinear spectroscopy*. PhD thesis, Massachusetts Institute of Technology, June 2009.

[56] L. Pálfalvi, J. Hebling, J. Kuhl, A. Péter, and K. Polgár, "Temperature dependence of the absorption and refraction of mg-doped congruent and stoichiometric linbo3 in the thz range," *Journal of Applied Physics*, vol. 97, no. 12, pp. –, 2005.

[57] J. A. Fülöp, L. Pálfalvi, G. Almási, and J. Hebling, "Design of high-energy terahertz sources based on optical rectification," *Opt. Express*, vol. 18, pp. 12311–12327, Jun 2010.

[58] P. Drude, "Zur elektronentheorie der metalle," *Annalen der Physik*, vol. 306, no. 3, pp. 566–613, 1900.

[59] Y.-S. Lee, T. Meade, V. Perlin, H. Winful, T. B. Norris, and A. Galvanauskas, "Generation of narrow-band terahertz radiation via optical rectification of femtosecond pulses in periodically poled lithium niobate," *Applied Physics Letters*, vol. 76, no. 18, 2000.

[60] J. Hebling, G. Almasi, I. Kozma, and J. Kuhl, "Velocity matching by pulse front tilting for large area thz-pulse generation," *Opt. Express*, vol. 10, pp. 1161–1166, Oct 2002.

[61] O. E. Martinez, "Grating and prism compressors in the case of finite beam size," *JOSA B*, vol. 3, no. 7, pp. 929–934, 1986.

[62] L. Cohen, "Generalization of the wiener-khinchin theorem," *Signal Processing Letters, IEEE*, vol. 5, no. 11, pp. 292–294, 1998.

[63] R. Molo, *Investigation of Short-Pulse Radiation Sources at DELTA Based on Coherent Harmonic Generation and Echo-Enabled Harmonic Generation.* PhD thesis, Technische Universität Dortmund Fakultät Physik, Oktober 2011.

[64] S. Reiche, "Genesis 1.3: a fully 3d time-dependent fel simulation code," *Nuclear Instruments and Methods in Physics Research Section A: Accelerators, Spectrometers, Detectors and Associated Equipment*, vol. 429, no. 1, pp. 243–248, 1999.

[65] W. J. G. C. Fultz, C. L. Whitten, "The lrl (livermore) 100 mev linear electron accelerator and facility," *IEEE Trans. on Nucl. Sci. NS-18*, vol. 533, 1971.

[66] F. Albert, S. G. Anderson, G. G. Anderson, A. J. Bayramian, S. M. Betts, T. S. Chu, D. J. Gibson, R. A. Marsh, M. J. Messerly, M. Y. Shverdin, *et al.*, "Advanced compton scattering light source r&d at llnl," in *International Conference on Ultrafast Phenomena*, p. ThE29, Optical Society of America, 2010.

[67] K. Halbach and R. Holsinger, "Superfish-a computer program for evaluation of rf cavities with cylindrical symmetry," 1976.

[68] L. Young and J. Billen, "The particle tracking code parmela," *PAC03 Proceedings, May*, 2003.

[69] M. De Loos and S. Van der Geer, "General particle tracer: A new 3d code for accelerator and beamline design," in *Proceedings of the fifth European Particle Accelerators Conference Sitges*, p. 1241, 1996.

[70] L. Serafini and J. B. Rosenzweig, "Envelope analysis of intense relativistic quasilaminar beams in rf photoinjectors: ma theory of emittance compensation," *Physical Review E*, vol. 55, no. 6, p. 7565, 1997.

[71] J. Arthur *et al.*, "{Linac Coherent Light Source (LCLS)} conceptual design report," *SLAC-R-593*, 2002.

[72] G. Cheriaux, B. Walker, L. F. Dimauro, P. Rousseau, F. Salin, and J. P. Chambaret, "Aberration-free stretcher design for ultrashort-pulse amplification," *Opt. Lett.*, vol. 21, pp. 414–416, Mar 1996.

[73] R. Trebino, "Grenouille model 8-20 users guide, swamp optics, llc. trebino, r," *Atlanta*, vol. 37, 2007.

[74] M. Borland, "Elegant: A flexible sdds-compliant code for accelerator simulation," tech. rep., Argonne National Lab., IL (United States). Funding organisation: US Department of Energy (United States), 2000.

[75] MCIOptonix, "http://www.mcio.com/products/drz-screens.aspx."

[76] A. Murokh, J. Rosenzweig, M. Hogan, H. Suk, G. Travish, and U. Happek, "Bunch length measurement of picosecond electron beams from a photoinjector using coherent transition radiation," *Nuclear Instruments and Methods in Physics Research Section A: Accelerators, Spectrometers, Detectors and Associated Equipment*, vol. 410, no. 3, pp. 452–460, 1998.

[77] A. E. Siegman, "Defining, measuring, and optimizing laser beam quality," in *OE/LASE'93: Optics, Electro-Optics, & Laser Applications in Science& Engineering*, pp. 2–12, International Society for Optics and Photonics, 1993.

[78] C. Labmax, "http://www.coherent.com/products/?1591/labmax-top."

[79] N. M. Kroll, P. L. Morton, and M. Rosenbluth, "Free-electron lasers with variable parameter wigglers," *Quantum Electronics, IEEE Journal of*, vol. 17, no. 8, pp. 1436–1468, 1981.

[80] C. Scoby, P. Musumeci, J. Moody, and M. Gutierrez, "Electro-optic sampling at 90 degree interaction geometry for time-of-arrival stamping of ultrafast relativistic electron diffraction," *Physical Review Special Topics-Accelerators and Beams*, vol. 13, no. 2, p. 022801, 2010.